

BIO-INSPIRED OPTIMIZATION OF A TURBINE STAGE

by

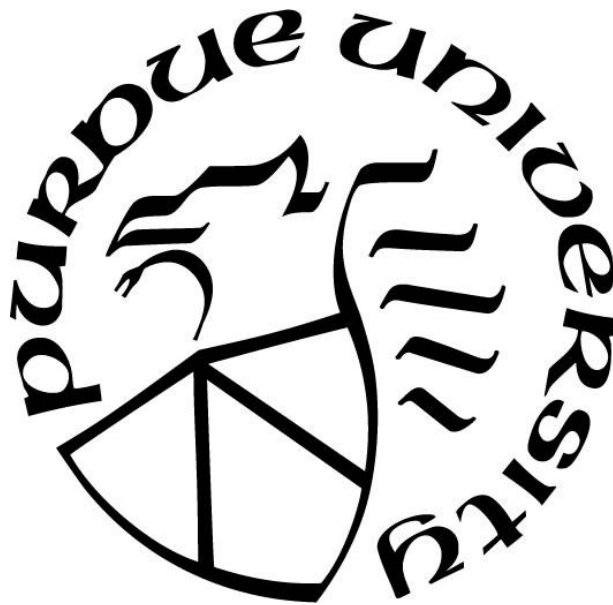
Paht Juangphanich

A Dissertation

Submitted to the Faculty of Purdue University

In Partial Fulfillment of the Requirements for the degree of

Doctor of Philosophy



School of Aeronautics & Astronautics

West Lafayette, Indiana

December 2019

**THE PURDUE UNIVERSITY GRADUATE SCHOOL
STATEMENT OF COMMITTEE APPROVAL**

Dr. Guillermo Paniagua, Chair

Department of Mechanical Engineering

Dr. Amy Marconnet

Department of Mechanical Engineering

Dr. Timothee Pourpoint

Department of Aeronautics and Astronautics

Dr. Vikram Shyam

NASA Glenn Research Center

Dr. John Clark

United States Air Force

Approved by:

Dr. Weinong Chen

To my parents for creating me and providing love and support and Danielle Daidone for being supportive and caring. To my brother's cat whom I will forcibly adopt after this is submitted. And to my brother for his cat.

ACKNOWLEDGMENTS

I would like to acknowledge Cis De Maesschalck, Jorge Saavedra, James Braun, Valeria Andreoli, Danielle Daidone, Udit Vyas, Nyansafo Aye-Addo, Lakshya Bhatnagar, Francisco Lozano, and Zhe Liu for their assistance and guidance throughout my PhD. I would also like to acknowledge my advisor Guillermo Paniagua and mentor Vikram Shyam for challenging me to think differently.

TABLE OF CONTENTS

LIST OF TABLES	8
LIST OF FIGURES	9
NOMENCLATURE	13
ABSTRACT.....	15
1. INTRODUCTION AND MOTIVATION	16
1.1 Turbine Secondary Flows	16
1.2 Turbine Loss	17
1.3 Turbine Loading.....	17
1.4 Turbine Design.....	18
1.5 Leakage Flows	19
1.6 Incidence Effects.....	21
1.7 Research Objectives.....	23
1.8 Research Methodology	23
1.9 Thesis Outline	24
2. NUMERICAL TOOLS.....	25
2.1 FineTurbo RANS Validation	25
2.2 Ansys Fluent URANS Validation.....	26
2.3 Optimizer: CADO Overview	28
2.4 CADO test case single objective Rosenbrock function	29
2.4.1 Rosenbrock results.....	30
2.5 CADO test case multi objective Kursawe function	30
2.5.1 Kursawe results.....	31
3. OPTIMIZATION OF THE TURBINE STAGE.....	32
3.1 Optimization Strategy Overview	32
3.2 1D Optimization Methodology.....	33
3.3 3D Optimization Strategy	34
3.4 Parameterization Strategy.....	35
3.4.1 2D Parameterization	35
3.4.2 3D Parameterization.....	36

3.4.3 Blade Count Selection	38
3.5 Computational Domain and Grid Sensitivity.....	38
3.6 Optimization Setup	41
3.7 1D Optimization Results.....	42
3.8 3D Optimization Results.....	43
3.8.1 Pareto Front	43
3.8.2 Trends in Stator Loss Generation	44
3.8.3 Trends in Rotor Loss Generation.....	45
3.8.4 Horlock Efficiency.....	47
3.8.5 Analysis of Optimal Profiles	49
4 BIO-INSPIRED TURBINE FOR OFF-DESIGN PERFORMANCE	53
4.1 Wavy Blade Design Methodology.....	53
4.2 Boundary Conditions	54
4.3 Computational domain and mesh sensitivity	56
4.4 Scaling Matrix Definition	58
4.5 Wavy parameterization	59
4.6 Optimization Setup	60
4.7 Results.....	61
4.7.1 Optimization Results	61
4.7.2 Pressure loss and separation bubble	62
4.7.3 Impact on Mach Number	65
4.7.4 Secondary Flow	71
4.7.5 Blade Loading.....	72
4.7.6 Stage Performance	73
5. OPTIMIZATION OF THE CAVITY	77
5.1 Design Optimization Approach	77
5.1.1 Optimization Strategy	77
5.1.2 Meander-line parameterization.....	78
5.1.3 Creation of the stator and rotor rim cavity shape	79
5.1.4 Computational domain.....	80
5.1.4 Grid sensitivity and convergence analysis.....	81

5.2	Results of 2D Optimization	82
5.2.1	Geometries that reduce rear platform temperature	82
5.2.2	Blockage and Exit Flow Angle	84
5.2.3	Smoothness comparison	85
5.2.4	2D/3D Stationary and Rotation comparison	86
5.2.5	Gap Sensitivity	88
5.2.6	Pressure Sensitivity	90
5.3	Assessment in a Turbine Stage	91
5.3.1	Computational Domain	91
5.3.2	Boundary Conditions and solver setup	92
5.3.3	Comparison between 2D and 3D Stationary and Rotation	93
5.3.4	Cavity impact on rotor performance	94
5.3.5	Effect of the gap spacing and leakage inlet pressure	96
5.4	Development of an Experimental Methodology	97
5.5	Experimental Design of the Test Article Methodology	97
5.5.1	Boundary Conditions	98
5.5.2	Matching Cavity Isentropic Mach and Nusselt	100
5.6	Experimental Requirements	102
5.7	Design of the Settling Chamber	103
5.7.1	1 to 2 Inlets with inner casing	103
5.7.2	1,2, 4, and 8 Inlets without inner casing	105
5.7.3	Linear Test Section Hardware	108
	CONCLUSION	110
	FUTURE WORK	113
	REFERENCES	115
	LETTERS	124
	PUBLICATIONS	126

LIST OF TABLES

Table 1. Optimizer constants for both 1D and 3D optimizations	28
Table 2. Single Objective Differential evolution setup for Rosenbrock function	29
Table 3. Rosenbrock evaluation results	30
Table 4. Multi-objective Differential evolution setup for Kursawe Function	31
Table 5: Stator and rotor grid sensitivity configuration.....	39
Table 6. Optimizer constants for both 1D and 3D optimizations	42
Table 7. Characteristics of 1D Final Design.....	43
Table 8. Inlet boundary conditions and outlet quantities.....	55
Table 9. Mesh size and corresponding pressure loss	57
Table 10. Endwall secondary flow loss contribution.....	72
Table 11. Stage baseline and wavy simulations at design conditions.....	76
Table 12. Stage baseline and wavy simulations at +15 incidence	76
Table 13. Boundary Conditions	77
Table 14. 2D/3D cavity simulation boundary conditions	87
Table 15. 2D/3D cavity inlet total conditions.....	87
Table 16. Highly Loaded Turbine without Purge	92
Table 17. Inlet and outlet boundary conditions for simulations with turbine.....	93
Table 18. Cavity boundary conditions when simulating with turbine	93
Table 19. Scaled Boundary Conditions	99
Table 20. Cavity Inlet Boundary Conditions	100
Table 21. Experimental Requirements.....	102
Table 22. Boundary conditions for single inlet design without contraction	105
Table 23. Settling chamber boundary conditions with 20 mm contraction	106
Table 24. Settling chamber flow exit properties 20mm contraction.....	107

LIST OF FIGURES

Figure 1. Classical secondary flow model of Hawthorne [1,2]	16
Figure 2. Left: Evaluation of the horseshoe vortex by Sieverding and Van den Bosche [7]. Right: Secondary flow structure by Sharma and Butler [5]	17
Figure 3. Left: Solid airfoil is aft-loaded, dashed is front-loaded. Right: A-Aft loaded design. B- Front loaded design [16]	18
Figure 4. Incidence. Left: Positive incidence flow angle. Right: Separation bubble on the suction side.....	21
Figure 5. Left: Experimental Test Case. Right: Computational Domain	25
Figure 6. Left: Stator midspan isentropic mach number. Right: Computational Domain	26
Figure 7. Validation Backward Facing Step	27
Figure 8. Rosenbrock function with 2 inputs.....	29
Figure 9. Rosenbrock function optimization results	30
Figure 10. Kursawe Results	31
Figure 11: Overview of the turbine stage optimization strategy.....	32
Figure 12: Overview of the 3D optimization structure	34
Figure 13: 2D Parameterization strategy for the blade profiles in the 2D cascade planes ...	36
Figure 14: Three-dimensional stacking of the blade profiles through a lean distribution	37
Figure 15: Channel Parameterization.....	37
Figure 16: Computational Domain	39
Figure 17. Stator and rotor pressure losses for 4 mesh of the grid sensitivity analysis	40
Figure 18. Effect of mesh size to the entropy creation across each row: (a) Stator; (b) Rotor.	41
Figure 19. Turbine stage Efficiency calculation locations.....	41
Figure 20. Left: 1D optimization results. Right: chosen design.	43
Figure 21: Pareto Front (left) and colored by the degree of reaction and turning angle (right)	44
Figure 22. Left: Relation of the stator losses with the aerodynamic quantities. Right: Geometrical characteristics.....	45
Figure 23. Left: Effect of the rotor turning. Right: The influence of the blade lean.	46

Figure 24. Rotor entropy loss coefficient vs. stagger angle. Left: Hub stagger angle. Mid: Mid profile stagger angle. Right: tip stagger angle.....	47
Figure 25. The stage efficiency in function of the aerodynamic losses (left) and the compensation strategy for the Horlock efficiency equation (right).	49
Figure 26. Stator optimal profiles and channel geometry.....	50
Figure 27. Rotor optimal profiles.....	51
Figure 28. Rotor Isentropic Mach number. Left: Mid span. Right: Tip.	52
Figure 29. Wavy blade design methodology	53
Figure 30. Baseline rotor. Left: suction side. Right: pressure side	54
Figure 31. Boundary Conditions vs. Radius. a) Total relative pressure. b) Rotor inlet flow angle. c) Total relative temperature	55
Figure 32. Wavy computational domain.....	56
Figure 33. Mesh Sensitivity +20 deg incidence, a) Pressure loss b) Efficiency	57
Figure 34. Left: Wave Rotation. Right: LE, TE, SS, Waves	58
Figure 35. Wave amplitude along the blade surface Left: Suction side. Right: Pressure Side	59
Figure 36. Location of the center point.....	59
Figure 37. Wave amplitude definition. Amplitude as a function of % span.....	60
Figure 38. Optimized wavy design	61
Figure 39. Optimized design wave definition as a function of span. a) Leading edge wave. b) Suction side wave. c) Trailing edge wave. d) Location of cut planes near the tip	62
Figure 40. Ratio of total pressure at exit to inlet.....	62
Figure 41. Large recirculation region around the suction side. Top: baseline blade: Bottom: Optimized Wavy design	63
Figure 42. Streamlines comparison. Top: baseline. Bottom: Optimized.....	64
Figure 43. Q-criterion. Left: Baseline blade. Right: Wavy Blade	65
Figure 44. Mach Number contours near the shroud	66
Figure 45. Iso-surface of constant Mach number. Left: Baseline. Right: Optimized.....	67
Figure 46. Density Gradient. Top: 70% span. Mid: 80% span, Bottom: 90% span.	67
Figure 47. Mach contour and density gradients at 50%. Left column: Baseline. Right column: Optimized. Top row: Mach contours. Bottom Row: Density gradients magnitude.	68

Figure 48. Vorticity at 50% span. Top Row: X-Vorticity. Bottom Row: Y Vorticity. Left Column: Baseline. Right Column: Optimized.	69
Figure 49. Vortex Structures. Left column: Baseline. Right column: Optimized.	69
Figure 50. Trailing edge wake profile.....	70
Figure 51. Secondary Flow. Left: Baseline blade. Right: Optimized.	71
Figure 52. Top row: isentropic mach number for 3 different spanwise locations. Bottom row: Cp distribution for 3 different spanwise locations. Dotted blue line indicates the sonic line	73
Figure 53. Top: Total-Total efficiency. Bottom: Pressure loss	74
Figure 54 Stage computational domain	75
Figure 55. Boundary conditions of stage and rotor only simulations	75
Figure 56. Hub disk design overall strategy	78
Figure 57. Left: Meander line. Middle: Stator and rotor rim thicknesses. Right: Stator rim and rotor rim shape.	79
Figure 58. a) Purge smoothing using Bezier curves. b) Removal of sharp corners.....	80
Figure 59. Computational domain mesh generated using HEXPRESS.....	80
Figure 60. Cavity Mesh Sensitivity	81
Figure 61. Rear Temperature plotted against massflow ratio	83
Figure 62. Top: Contours of temperature and lines of constant Q Criterion. Bottom: Contours turbulence kinetic energy with lines of constant Q Criterion	84
Figure 63. Blockage vs. Massflow contoured with purge exit flow angle	85
Figure 65. Left: Heat flux within the cavity comparison with smooth geometry. Right Top: Design B jagged. Right Bottom: Design B Smooth.....	86
Figure 66. Computational Domain	87
Figure 67. Top: Heat Flux [W/m ²] inside the cavity. Bottom: Heat flux along the rotor platform vs axial direction.....	88
Figure 68. Heat flux vs. massflow by changing gap size.....	89
Figure 69. Heat flux along the platform for different gap sizes.....	90
Figure 70. Heat flux along platform vs. massflow by changing pressure.....	91
Figure 71. Optimized Geometry “B.” Rotation was applied to the stator walls.....	92
Figure 72. Nusselt number within cavity X.....	93
Figure 73. a,b) Secondary flows plotted with iso surface of rothalpy, massflow ratio 10% both cases. c,d) Platform heat flux.....	94

Figure 74. a) Stage Efficiency. b) Massflow Ratio. c) Increase in secondary flow. d) Sealing Effectiveness	95
Figure 75. Top: Corrected efficiency vs. gap and pressure. Bottom: Discharge coefficient vs. gap	96
Figure 76. Channel geometry without stator, rotor, or purge	98
Figure 77. Test Article 5x scaled	98
Figure 78. Isentropic mach number along the channel and linear test section test article....	99
Figure 79. Mach number contour. Left: Linear. Right: Engine boundary conditions and geometry. Dotted line: start of the cavity.....	99
Figure 80. Cavity Total Pressure selection strategy.....	100
Figure 81. Straight Purge Isentropic mach number, purge comparison with linear	101
Figure 82. Straight purge Mach Number. Left: Linear test section. Right: Engine.....	101
Figure 83. Design X Mach Number. Left: Linear test section. Right: Engine	102
Figure 84. Left: Settling chamber used in the VKI C4 tunnel. Right: Settling chamber used in the VKI C3 tunnel.....	104
Figure 85. Settling chamber with single inlet	104
Figure 86. Double inlet settling chamber.....	105
Figure 87. Settling chambers with contraction. a.) single inlet b.) double inlet c.) 4 inlets d.) 8 inlets	106
Figure 88. Left: Contraction Geometry and dimensions. Middle: Settling chamber and dimensions. Right: Settling chamber cross section	107
Figure 89. Settling Chamber contraction exit mach number and massflow vs. inlet total pressure simulated with 10mm contraction width.....	108
Figure 90. Mounting Hardware Linear Test Section	109
Figure 91. Left: Linear test section with purge hardware. Right: Settling chamber with the purge hardware.....	109

NOMENCLATURE

c	=	Chord [mm]
C_p	=	Specific heat [J/(kgK)]
C_p	=	Coefficient of Pressure
δ	=	Boundary layer thickness
Gz	=	Graetz number
h	=	Convective heat transfer coefficient [W/(m ² K)]
H	=	Blade height [mm]
k	=	Thermal conductivity of air [W/(mK)]
\dot{m}	=	Massflow rate [kg/s]
M	=	Mach number
Nu	=	Nusselt number
P	=	Pressure [bar]
P_{0loss}	=	Total Pressure Loss
Pr	=	Prandlt number
Q	=	Integrated heat flux [W]
r	=	Radial coordinate
r_p	=	Degree of reaction
RPM	=	Rotational speed
s	=	Specific Entropy [J/(kgK)]
T	=	Temperature [K]
V	=	Velocity [m/s]
XR	=	Reattachment length from step
z	=	Axial coordinate

Subscripts

0	=	Total flow quantity
$0c$	=	Total flow quantity at cavity inlet
1	=	Inlet
2	=	Rotor-stator interface
$02R,2R$	=	Rotor Inlet relative frame
3	=	Outlet
ax	=	Axial component
bl	=	Boundary layer
is	=	Isentropic
θ	=	Tangential component
r	=	Radial component
$s3$	=	Static exit
TT	=	total-total

Greek symbols

∞	=	Freestream
α	=	Absolute flow angle, purge exit angle
β	=	Relative flow angle
γ	=	Ratio of specific heats
η	=	Efficiency
ρ	=	Density
τ	=	Shear stress
θ	=	Tangential component
ψ	=	Stage loading
ω	=	Angular velocity

ABSTRACT

To reduce fuel burn, aircraft manufacturers and NASA are exploring concepts to maximize the thermal and propulsive efficiency, one concept is the hybrid turbo-electric powertrain. In these novel architectures, coupling an electrical generator one may encounter turbine incidence problems. There is also a demand for the gas generator to be compact to achieve weight savings which means the turbine will need to be both highly loaded and efficient. In nature, millions of years of evolution has produced designs that reduce drag over a wide range incidence angles. This dissertation presents a strategy that incorporates nature and bio-inspired shapes to redesign turbine airfoils and stator-rotor rim seal cavity.

A differential evolution optimizer was used to fulfill the objectives of the thesis. The first objective consists of the development of tools to optimize the turbine velocity triangles and then the 3D shape using 75 parameters. Design trends that minimize loss in the stator and rotor were discussed. The second objective expands on the first by incorporating wavy structures at the leading and trailing edges as well as the suction side mimicking design features of seal whiskers and tubercles of a whale. The airfoils were optimized to maximize the efficiency of a highly loaded high-pressure turbine at positive incidence.

The last objective addressed the design of the cavity to reduce cooling massflow and protect the turbine platform. A novel strategy was proposed to assess and optimize the shape of the cavity. In an attempt to simplify the problem and identify the main physical phenomena, a slice of the flow was examined by considering a purely a 2D case in the relative frame of reference. This simplification enabled the cavity to be optimized in 2D using a geometry inspired by the meandering of rivers. The optimization produced designs that reduce the heat flux in the rear rotor platform and are less sensitive towards variations in gap and cavity total pressure. The methodology was demonstrated in 3D rotating cavity and later in a full turbine stage configuration. The strategy and design tools developed in this dissertation seek to provide understanding of the effects of bio-inspired shapes on turbine blades and lay the foundation for future experimental research into cavity flows.

1. INTRODUCTION AND MOTIVATION

1.1 Turbine Secondary Flows

The design and optimization of a turbine requires the understanding of secondary flows. Secondary flow structure in a turbine consists of 4 main vortices: the two legs of horseshoe vortex, corner or counter vortex, and most importantly the passage vortex. The passage vortex is created by turning of the incoming boundary layer shown in Figure 1.

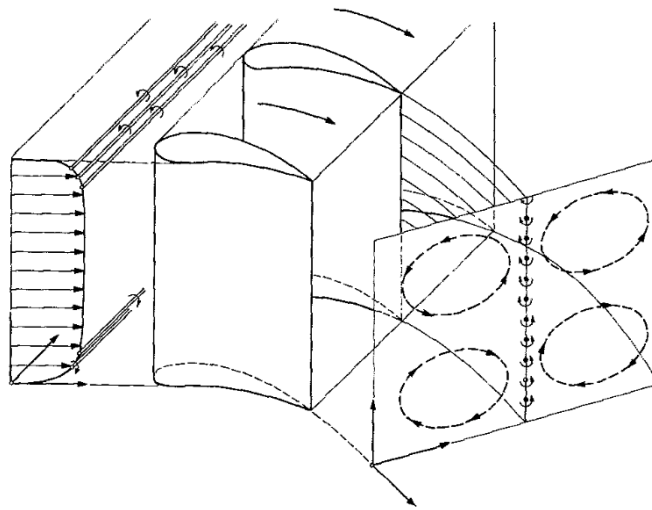


Figure 1. Classical secondary flow model of Hawthorne [1,2]

The horseshoe vortex is formed by the inlet boundary layer rolling up as it meets the blade's leading edge. The vortex splits into two legs (Figure 2-Left), the pressure side horseshoe vortex and the suction side horseshoe vortex. The pressure side leg of the horseshoe vortex (H_p) merges with the passage vortex [3] as shown in Figure 2-Right. The horseshoe vortex on the suction side (H_s) called the counter vortex because it rotates in opposite direction to the passage vortex [4], this vortex wraps around the passage vortex [5,6].

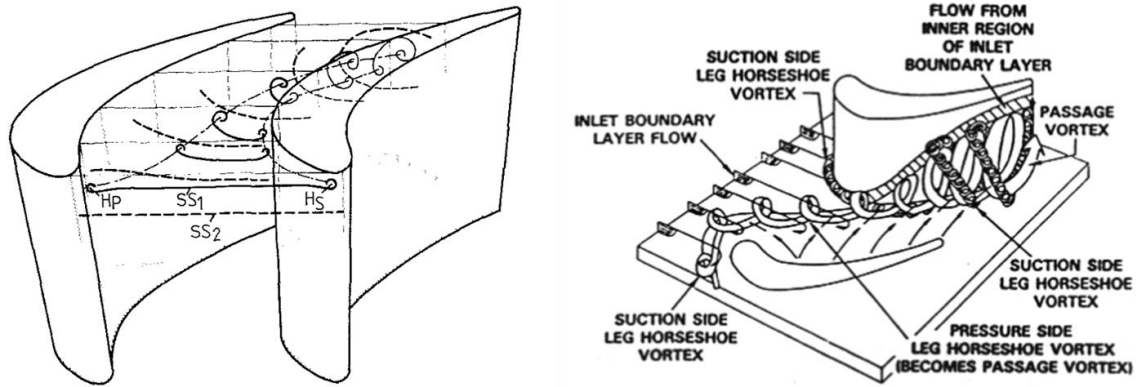


Figure 2. Left: Evaluation of the horseshoe vortex by Sieverding and Van den Bosche [7]. Right: Secondary flow structure by Sharma and Butler [5]

1.2 Turbine Loss

Turbine loss can be broken down into three components profile loss, endwall loss, and leakage loss [8]. Profile loss includes the viscous losses in the boundary layer of the blade including the trailing edge. Endwall loss is associated with secondary flows. This loss is due to the roll up of boundary layers developed along the endwalls as they impact the airfoil's leading edge. Sharma and Butler [5] developed an empirical model for estimating endwall secondary flow losses based on results from an experimental cascade. They estimated that secondary flows can account for 30-50% of the total pressure loss in a turbine blade. Leakage loss includes leakage of the flow over the tip, the hub disk between the stator and turbine, and any release of cooling flow into the mainstream.

1.3 Turbine Loading

Efforts to minimize loss have revolved around changing the airfoil's loading. The desire is to control the rate of acceleration and diffusion along the turbine passage. Front loading increases the lift which results in an adverse pressure gradient on the suction surface. Additionally, strong diffusion generates stronger secondary flows.

Zoric et al. [9] investigated three highly loaded low-pressure turbine airfoils. They concluded that at design conditions the front-loaded blade has higher profile loss than the two aft-loaded designs, also with stronger secondary flows. This occurs because diffusion starts earlier on the suction side (Figure 3-Right). Aft-loaded blades delay the diffusion towards the

trailing edge (Figure 3-Left) and as a result they have less secondary flow and profile losses. Weiss and Fottner [10], Dossena et al [11], Hodson and Dominy [12], Corriveau and Sjolander [13], Perdichizzi and Dossena [14], and Benner et al. [15] reached the same conclusions.

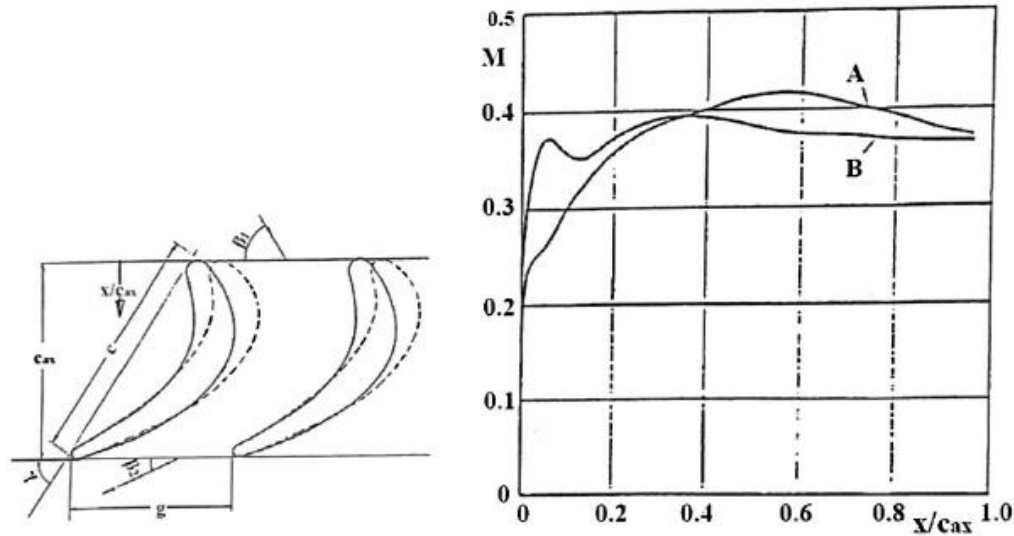


Figure 3. Left: Solid airfoil is aft-loaded, dashed is front-loaded. Right: A-Aft loaded design. B-Front loaded design [16]

Corriveau and Sjolander looked at loading distribution on high pressure turbine blades at off-design [17]. At off-design conditions, the inlet angle varied -10 to 10 degrees relative to design. They showed that the aft-loaded design had more losses at off-design mach numbers and flow angles compared to the front loaded design. Notably, Lydall et al. [18] showed that by changing the stagger angle at the endwalls of a front loaded airfoil, the secondary flows loss caused by endwalls can be reduced by 20% at design conditions. Praisner et al. [19] compared different airfoil loading designs: front, center, and aft loaded. Their results showed that with endwall contouring, front loaded designs can have similar losses as an aft-loaded blade.

1.4 Turbine Design

The initial conceptual design of turbomachinery components often relies on expertise and design guidelines from previous engine programs. Once the overall architecture is decided, simplified 1D models are used to set the velocity triangles throughout the different stages.

Subsequently, 2D throughflow solvers are adopted to determine the radial distribution of the flow quantities, relying on correlations and empirical models from experimental campaigns and historical engine data.

Traditional design tools such as Turbine Design and Analysis System (TDAAS) [20] use splines that define the pressure and suction sides. The design is then verified by performing a 2D CFD optimization on a single profile. Once optimized, a series of 2D blade profiles are radially stacked to generate full 3D turbine design, lean and sweep distributions are added afterwards [21].

The optimization of a full stage is computationally intensive, researchers often optimize a single airfoil at a time: Shelton et al. [22] optimized a turbine blade under transonic conditions incorporating a stacking and sweep law. Sousa and Paniagua [23] adopted Bezier curves to optimize the design of supersonic turbine blades, illustrating the flexibility of these curves to generate geometries going from slender compressor blades [24] to thick turbine blades [25] with high turning. Thorn and Hartfield [26] used a combination of Bezier curves to define 2D airfoil shapes and NURBS to design the 3D blade with a total of 136 design parameters to represent the turbine blade.

A comprehensive 3D optimization approach is essential to obtain blade shapes, and the methodology needs to allow an exploration of a wide design space to reveal novel optimal trends that relate loading with efficiency. To ensure optimal compatibility, both the turbine, stator, and channel should be optimized simultaneously.

1.5 Leakage Flows

Minimize leakage flows between the stator and rotor is a major concern for turbine's performance. Leakage flows affect the incidence of the blade, it causes a blockage of the main flowpath [27], and changes the degree of reaction of the stage. There is also the physical mechanism of ingestion of main flow into the stator-rotor gap. Ingestion is caused by two mechanisms the first is referred to as externally induced ingress [28], which is caused by pitchwise asymmetric pressure variations from the stator which is affected by the potential field from the passing of the rotor, and turbulent transport within the fluid [29]. The second type of ingestion is rotationally-induced [30], which occurs without the presence of axisymmetric pressure distributions of the stator or rotor blades. This type of ingestion is caused centrifugal

forces of the disk rotating which pumps the fluid outwards, the static pressure inside the disk can be lower which causes the mainflow to enter. Ingestion in the turbine can be dominated by either of the two types depending on the geometry [31].

This dissertation addresses the interaction of the cavity flow with the main flow. Studies have shown that the purge flow enhances the rotor hub vortex [27,32–34]. This phenomenon prevents coolant from reaching rear rotor platform near the pressure side; as a result, end wall cooling is often required to protect both the vane and rotor platforms, and in some instances, may be used to cool the blade region close to the platform near the trailing edge. A 167K change in temperature can result in a 3 to 4 times increase in turbine life [35,36].

To capture some of the physics, researchers model the cavity using 3D Unsteady Reynolds Averaged Navier Stokes or they perform expensive experiments. LES has also been used to identify pressure instabilities and vortical structures within the cavity. Most of the designs aim preventing ingestion and controlling the interaction with the main flow. There has been a large number of publications on both the sealing effectiveness of different seal designs and on the interaction of purge flow with the main flow. Double seal designs have been investigated by Zhou et al. [37]. Zhou and co-workers showed that double overlap seals with low aspect ratios (where seal gap is reduced) had the best sealing effectiveness. Additionally, there have been studies on how to parameterize and optimize purge designs. Moon et al. [38] parameterized a rectangular cavity on the stator side of a double overlap seal configuration and studied the sealing effectiveness and the influence the seals had on minimizing passage vortex. Popović and Hodson [39] investigated the effect of changing the overlap of the rim seal geometry on sealing effectiveness and the effect on the passage vortex using a linear experimental rig. In 2012, Popović and Hodson [40] discovered that an inclined ejection does not result in a strong leakage vortex. Injecting coolant flow at a shallower angle provides better coolant to the endwall. None of the researchers were able to perform a full optimization of the cavity, they parameterized in order to study the effects of changing the geometry on a few cases.

The study of rim seal design configurations has primarily been focused on preventing ingestion. However, the effect of purge flow on the rotor platform should also be considered. McLean et al. [41] studied the effect of purge flow on the performance of the turbine. They showed that a 1% change in cooling can significantly affect the total-total efficiency of the turbine. Pau et al. [27] measured the effect of purge flow on the Nusselt number on the rotor

platform. They determined that rotor platform cooling has minimal effects on the suction side and trailing edge of the rotor. Barigozzi et al. [42] also suggested that this is due to the coolant flow from the hub disk being captured by the rotor hub passage vortex which moves the coolant away from the rotor endwalls. Suryanarayana et al. [43,44] showed using pressure- sensitive paint that coolant supplied by purge flow did not provide sufficient coolant to the pressure side of the rotor. There is a need to repurpose leakage flows, instead of simply preventing ingestion, the cavity shape can be optimized to redirect coolant to protect the rotor platform while also minimizing the required massflow rate to do so.

1.6 Incidence Effects

Incidence effects appear when the angle of the incoming flow entering is different than the metal angle of the airfoil. When the flow angle is greater than the metal angle, this is called positive incidence, flow stagnates on the pressure side (Figure 4-Left). Positive incidence increases the loading along the front suction side, causing a separation bubble to appear on the suction side (Figure 4-Right). The local diffusion farther enhances the intensity of the passage vortex. [12].

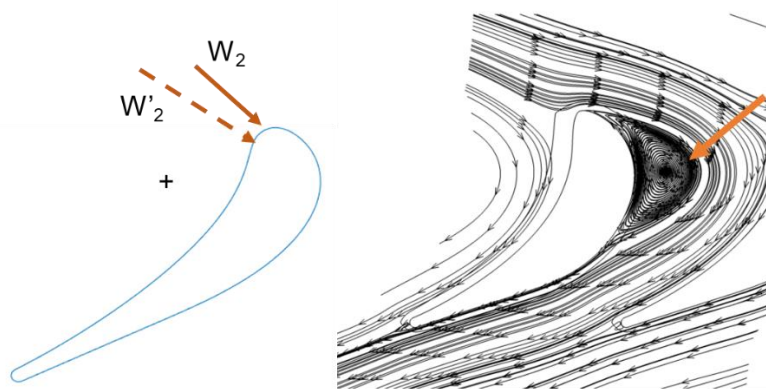


Figure 4. Incidence. Left: Positive incidence flow angle. Right: Separation bubble on the suction side

Minimizing the effects of incidence is a challenge for turbine designers. Turbines are designed to be efficient at a given operating condition for example at cruise. Incidence can occur when the RPM is reduced, this problem occurs in highly loaded low pressure turbines during a climb, while performing maneuvers or at high altitudes. Negative incidence decreases the

loading and results in more efficiency, however separation could occur on the pressure side for high turning low pressure turbine designs [45].

Many researchers have studied the application of wavy shapes from nature as a form passive flow control. These shapes commonly found in marine mammals and fish, for example, leading edge bumps on the hammerhead shark's head help it maneuver and take down prey [46]. The humpback whale's flipper features tubercles that help it perform tight turns [47–49]. The whiskers on the harbor seal allows it to hunt in deep dark waters by detecting and following vortices shed by fish (hydrodynamic trail following). Leading edge protuberances have been shown to reduce the recirculation zone and breakdown large vortical structures [50].

Shyam et al. [51] compared a harbor seal whisker inspired design of a power turbine blade to a conventional design at various flow angles up to +10 degrees of incidence and Reynolds number of 100,000. They were able to delay separation and reduce pressure loss for all angles in the seal whisker blade. Luo et al [52] showed that a wavy trailing edge based on Hanke et al. [50] was able to reduce mixing loss at the trailing edge. Pym et al. [53] studied the effect of leading edge waves on low pressure turbine airfoils. They applied tubercles commonly studied by other researchers, they concluded the leading edge waves increased the loss for all incidence angles; as the angle of attack was increased, the blade became more front loaded.

A number of researchers have also found negative results when applying waviness to wings and airfoils. Miklosovic et al. [54] tested a finite span and a full span wings. They showed that a wavy leading edge on a NACA0012 airfoil was able to delay stall in a finite span, however substantial loss in lift and increased drag was found for the full span. Hansen et al [55] tested leading edge waves on NACA 65-021 and NACA 0021. He concluded that tubercles worked best on NACA 0021 and through optimizing the amplitude and wavelength they were able to obtain similar performances as the original airfoil. Shyam et al [56] show that there is a difference in performance between harbor seal whiskers and elephant seal whiskers that both display span-wise waviness. Thus, all waviness is not necessarily beneficial.

There are a lot of literature on the application of wavy shapes to wings and low pressure turbine airfoils at low Reynolds and Mach number. Some researchers experience positive results while others find no benefit in applying the waves. Chapter 4 explores the optimization of waviness for an already optimized high pressure turbine operating at off-design conditions at high inlet flow angles, Mach and Reynold's numbers.

1.7 Research Objectives

The objective of this thesis is to explore applying designs found in nature to a turbine stage. The objective is accomplished in 3 phases:

- **The development of a highly loaded efficient turbine** is essential towards the development of future research turbines. Having a comprehensive 3D design optimization strategy that allows an exploration of the design space and can reveal optimal trends in stator and rotor losses is vital towards achieving this objective.
- **Improving the performance of a turbine at off-design** is a challenge for turbine designers. Biomimicry can serve as an inspiration for unique designs that can lead to more incident tolerant blades.
- **Development of a simplified design and optimization strategy for the cavity** is crucial towards future stage designs. The rear rotor platform is difficult area to cool due to secondary flows that migrate cooling flow from pressure side to suction side. Currently about 20% of the compressor massflow is used for cooling. Future engines with lean low NOx combustors will require even more cooling. It important to investigate cavity designs that minimize cooling massflow while also maximizing the delivery of coolant further along the rotor platform.

1.8 Research Methodology

To achieve the objectives, the following research strategy is proposed.

1. Development and assessment of the Numerical Tools

Fluid dynamic solvers such as FineTurbo (Numeca Inc.) and Fluent (Ansys Inc.) which are used for the objectives will be validated against experimental test cases. Furthermore, the optimizer and the optimization settings will also be validated.

2. Optimization of the Turbine Stage

A fast 1D meanline design tool will be paired with an optimizer. Secondly, a 3D turbine design tool will be developed. Results of the 1D optimization will be used as a seed point for the full 3D stage optimization.

3. Design of a bio-inspired incident tolerant blade

A wavy design strategy will be added to the 3D turbine design tool. A highly loaded turbine stage from the previous method will be optimized with waves at positive incidence.

4. Optimization of the Cavity

A simplified 2D methodology for optimization of the cavity will be assessed. An optimized cavity geometry will then be applied to a turbine and the impact will be compared with a conventional design. An experimental methodology will be proposed for testing the cavity in a linear wind tunnel.

1.9 Thesis Outline

- Chapter 2 describes the validation of FineTurbo and Fluent solvers against TATEF blade and the backward facing step, respectively.
- Chapter 3 presents the development of the design codes of the turbine stage and the methodology of the stator-rotor optimization. The mesh sensitivity is also presented and the lastly the results of the optimization are shown.
- Chapter 4 is focused on the bio-inspired design of the turbine stage.
- Chapter 5 contains the methodology of simplification of the hub disk cavity followed by a grid sensitivity study. The chapter goes into the optimization set of the hub disk and how the cooling of the rotor platform was evaluated. Finally, the experimental methodology of testing leakage flows in the linear test section.

2. NUMERICAL TOOLS

2.1 FineTurbo RANS Validation

Both Numeca tools, AUTOGRID and FINETRUBO were validated against an experimental test case. AUTOGRID is an automated structural meshing tool used to construct computational domains of internal passages in turbomachinery applications. FINETRUBO is a solver design for turbomachinery applications. Both tools are used in the manuscript to evaluate the design of turbines. To validate these cases an experimental test case of a transonic turbine [57] was chosen. Figure 5-Left shows the experimental test case, on the right is CFD domain with boundary conditions. The boundary conditions consist of imposing a total pressure and temperature upstream and static pressure downstream. The computational domain was solved using a steady state simulation and the SST turbulence model. Y^+ along the blade surface was less 0.4. The simulation was run until the massflow, the predicted torque, and efficiency all remained constant.

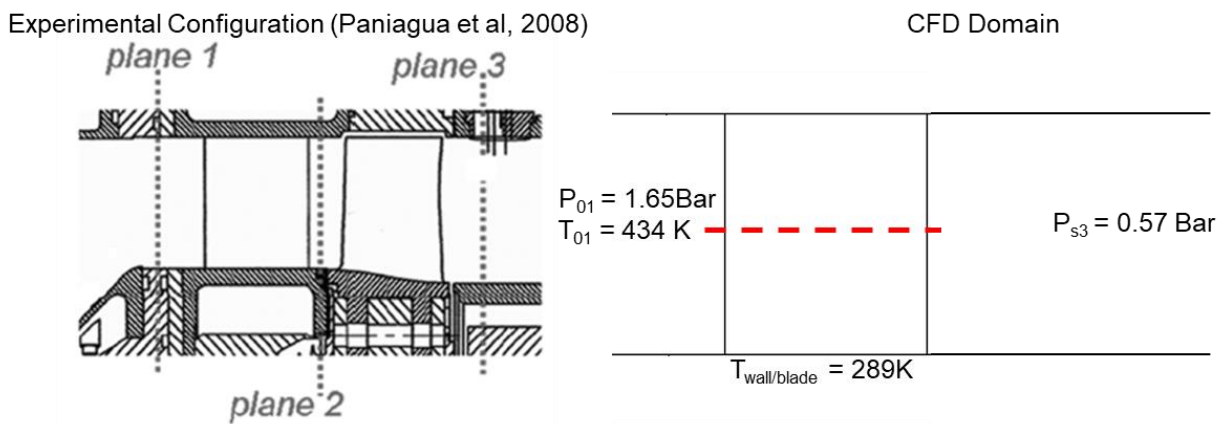


Figure 5. Left: Experimental Test Case. Right: Computational Domain

The isentropic mach number (Equation 1) along the mid-span of the stator was compared with experimental values from Paniagua et al. [57]. To match the experimental data, the stator was modeled without the rotor. The boundary conditions were adjusted to match a stator exit mach number. Figure 6: Left shows the isentropic mach number along the midspan of the stator modeled without the rotor. The computational simulation was able to capture the trend of the experiments.

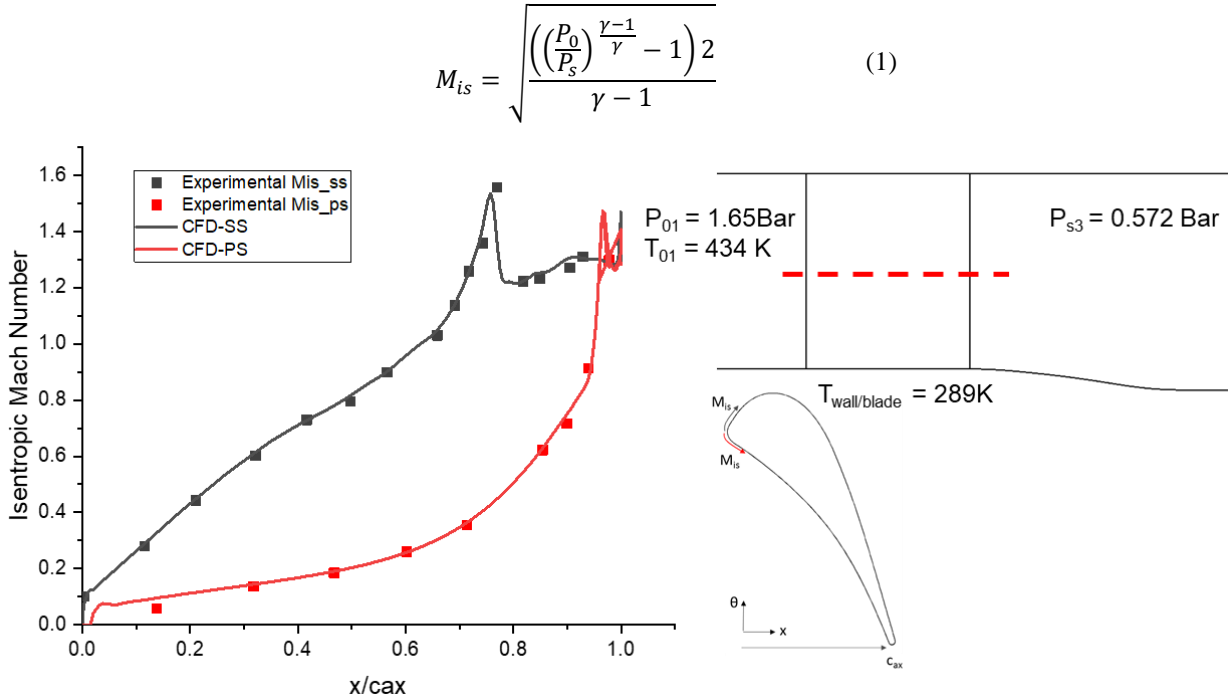


Figure 6. Left: Stator midspan isentropic mach number. Right: Computational Domain

2.2 Ansys Fluent URANS Validation

ANSYS FLUENT and HEXPRESS (Numeca, Inc.) were used to redesign the cavity. Both the solver FLUENT and the meshing tool HEXPRESS were validated against an experimental test case for the backward facing step [58]. Figure 7-Top shows the geometry of the backward facing step. The inlet of the domain is 2.2 m away from the step. The height of the inlet of the channel was set to 150mm. The step height is 3.8mm, same as Vogel and Eaton [58]. The bottom step length is set to be 55 times the step height to ensure proper convergence of the recirculation region.

The boundary conditions imposed at the inlet consisted of an inlet velocity of 11.3m/s and total temperature of 305K. At the outlet a static pressure boundary condition of 107kPa was used. A wall temperature of 290K was assumed at the step and bottom wall. The boundary layer height relative to the step height was measured at $-3.8H$ way from the step (x_{bl}) was found to be around 0.7 matching the data in Vogel and Eaton. Reattachment point (X_R) and was calculated by finding where skin friction (C_f) equals to zero. The computational domain was simulated using Unsteady Reynolds Average Navier Stokes simulation until heat flux along the bottom

wall after the step was converged. The SST Turbulence model [59] was used to provide closure to the Navier Stokes equations.

Figure 7-Bottom shows a comparison with the Stanton number (Equation 2) nondimensionalized by the max plotted against x nondimensionalized by the reattachment point. The results from the experiment (blue triangles) shows a good agreement in the location of the reattachment point compared to CFD. There is a discrepancy in the diffusion near the end of the comparison which could be related to 3D diffusion of turbulence quantities.

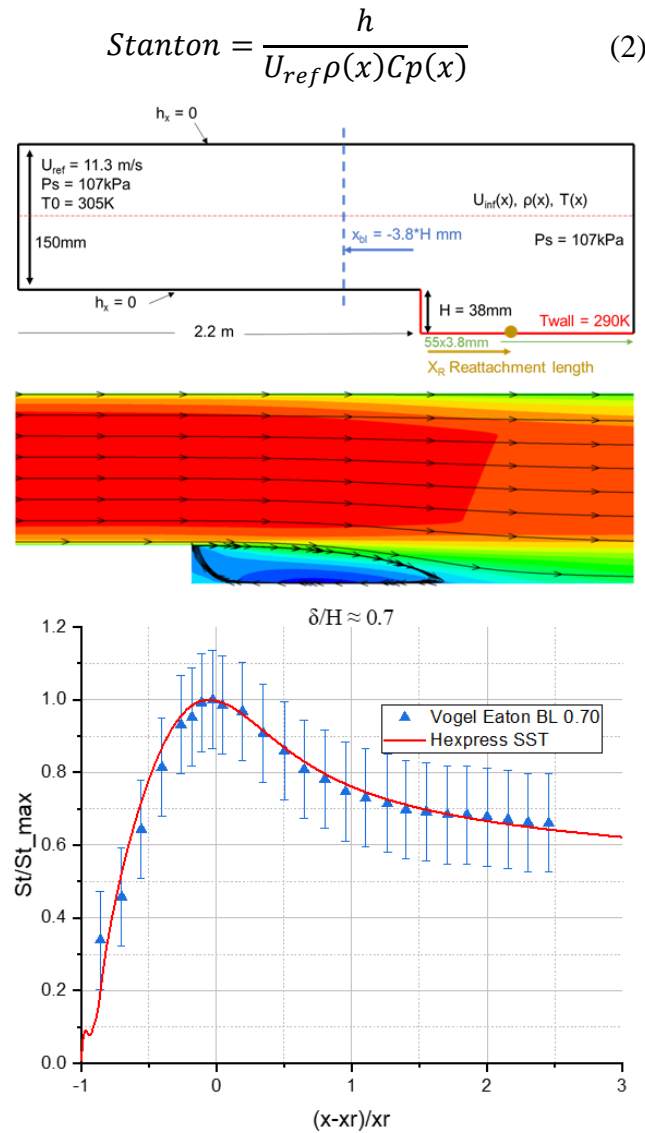


Figure 7. Validation Backward Facing Step

2.3 Optimizer: CADO Overview

The optimizer used for this project is CADO (‘Computer Aided Design and Optimization Tool’) [60]. CADO is a powerful optimization package developed at the von Karman Institute for Fluid Dynamics and has been previously applied for the improvement of a wide variety of turbomachinery components [25,60–62]. CADO uses either a single or multi-objective differential evolution strategy based on the Darwinian evolution [63], where every iteration a new set of individuals is generated via the process of crossover and mutation. Equation 3 and 4 describe mutation and crossover respectively. Vectors \vec{a} , \vec{b} , and \vec{c} denote unique individuals, r_i represents a random number generated between 0 and 1, ‘C’ is a constant value specified in Table 1. The resulting child individual ‘z’ are evaluated then combined with the previous population. Multi-objective is handled using the NSGA-II ranking mechanism, which locates optimal parents for the next generation [64]. Individuals evolve throughout each successive population, favoring the individuals with the lowest of each objective to eventually converge to the Pareto front, i.e. the subset of optimal profiles.

Table 1 summarizes the main optimization constants, namely the mutation scale factor and the mutation rate. Common values of the mutation rate vary from 0.5 to 1 [63,65]. Price et al. [66] recommends a crossover rate of 0.9 for functions with dependent parameters, and 0.5 for independent parameters. Gämperle et al. [67] showed that a large crossover rate speeds up the convergence, however convergence rate may decrease, or populations may approach a local minima and that a good choice is between 0.3 and 0.9.

Table 1. Optimizer constants for both 1D and 3D optimizations

	Symbol	Value
Mutation scale factor	F	0.6
Mutation rate	C	0.8

$$\text{Mutation} \quad y_i = a_i + F(b_i - c_i) \quad (3)$$

$$\text{Crossover} \quad z_i = \begin{cases} y_i & \text{if } r_i \leq C \\ x_i & \text{if } r_i > C \end{cases} \quad (4)$$

2.4 CADO test case single objective Rosenbrock function

The Rosenbrock function (Equation 5) [68] is a challenging single objective optimization problem that has been used as a test case in numerous optimization codes [69–75]. The function represents a parabolic valley, the gradients are near zero around the minimum located at $x_i = 1$. The valley is easy to find conceptually, but convergence to the minimum value is particularly difficult for an optimizer. For this test case, α was set to 100 and 2 dimensions was used, x_{1-2} ranged from -5 to 5.

$$f(x) = \sum_{i=1}^{d-1} [\alpha(x_{i+1} - x_i^2)^2 + (x_i - 1)^2] \quad (5)$$

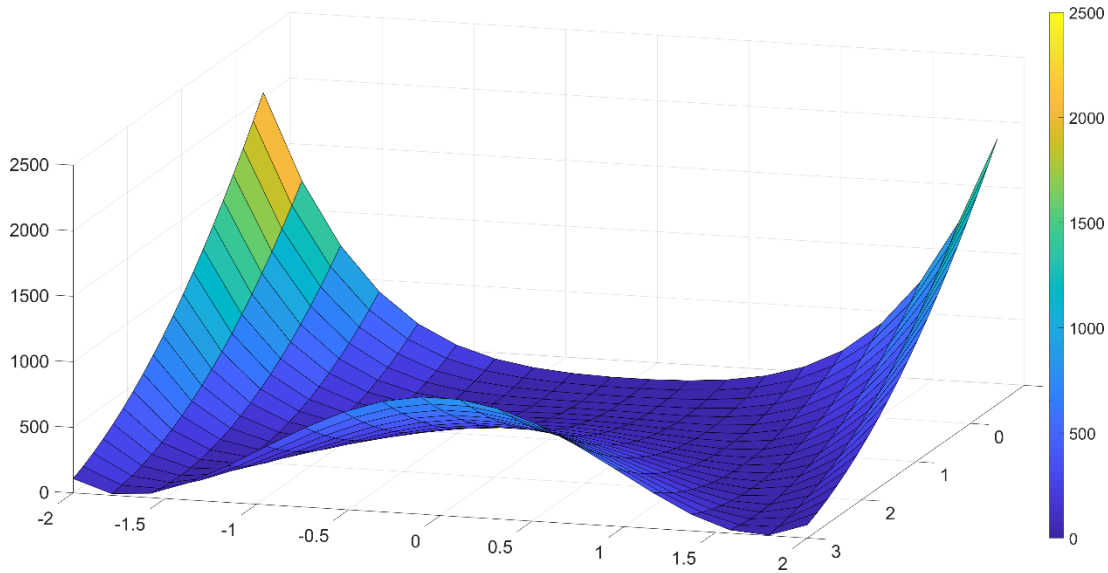


Figure 8. Rosenbrock function with 2 inputs

Table 2. Single Objective Differential evolution setup for Rosenbrock function

Number of Generations	40
Population Size	40
Design of Experiments Size	40
Rosenbrock Dimensions	2

2.4.1 Rosenbrock results

The minimum value found after 40 iterations is shown in Table 3. Figure 9 shows the results of the optimization plotted onto the Rosenbrock function. Successive populations gather near the minimum value. After 40 generations the minimum was found to be 1.1. to reach the center of the valley is very difficult because the gradients are very small, and it would require a larger population size and more optimization time.

Table 3. Rosenbrock evaluation results

x_1	0.44
x_2	0.19
Rosenbrock (x_1, x_2)	1.1

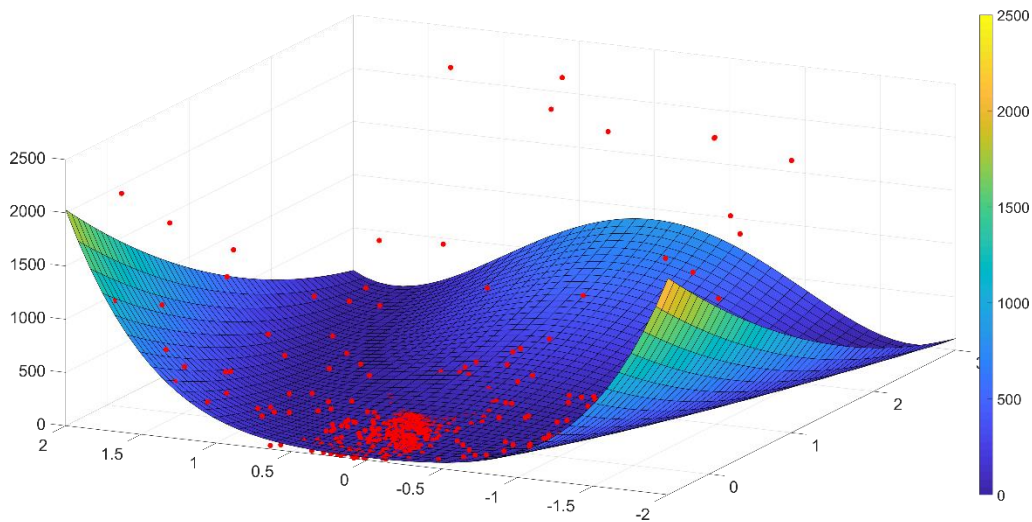


Figure 9. Rosenbrock function optimization results

2.5 CADO test case multi objective Kursawe function

Multi-objective was tested using the Kursawe function [76] (Equation 6). The Kursawe function is a multi-objective problem that creates the pareto front is a disconnected and asymmetric. It has been used as a test function by many researchers [71,74,77–79]. Table 4 contains the settings used to start the optimization. The design of experiments was changed to 128 and the number of parameters “ x_i ” was set to 3 with a range of -5,5.

$$\text{Minimize} \begin{cases} f_1(x) = \sum_{i=1}^{n-1} -10 \exp\left(-0.2 \sqrt{x_i^2 + x_{i+1}^2}\right) \\ f_2 = \sum_{i=1}^n (|x_i|^{0.8} + 5 \sin(x_i^3)) \end{cases} \quad (6)$$

Table 4. Multi-objective Differential evolution setup for Kursawe Function

Number of Generations	27
Population Size	40
Design of Experiments Size	64
Parameters (x_i)	3

2.5.1 Kursawe results

The objective of evaluating the Kursawe function is to reach a pareto front. A pareto front represents a trade-off between two objectives where the minimization of one objective adversely effects the other. Figure 10 shows the evaluation of Kursawe function. The two objectives are displayed in the x and y axes. The circles represent individual evaluations. Grey circles show individuals belonging to populations 0 to 9, blue 10 to 24, and red dots represents the final 3 generations/populations that make up the pareto front.

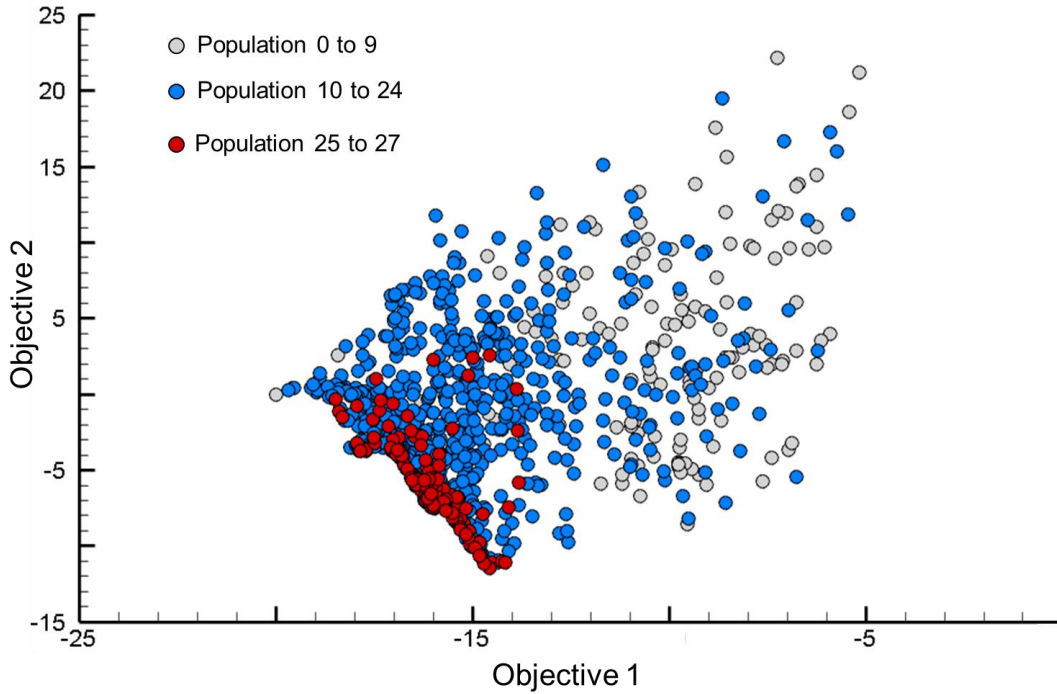


Figure 10. Kursawe Results

3. OPTIMIZATION OF THE TURBINE STAGE

3.1 Optimization Strategy Overview

The overall design methodology consisted of two consecutive steps as presented in Figure 11. First, a 1D optimization strategy was adopted to define the ideal operating conditions of the high-pressure turbine stage and to provide an estimation of the main aerodynamic quantities throughout the machine. In the second step, the turbine channel was parametrized, and the stator and rotor airfoils were defined in 2D cascade planes at several radii, combined to generate the full 3D blade profiles using stacking laws. The third step applies a lean distribution to the 3D blades creating the final stator and rotor designs. The blades are then fitted into a channel that is parameterized. The final 3D geometry is then solved in a 3D optimization routine that iterates through the parameters in order to determine the optimal designs for achieving maximum efficiency and stage loading.

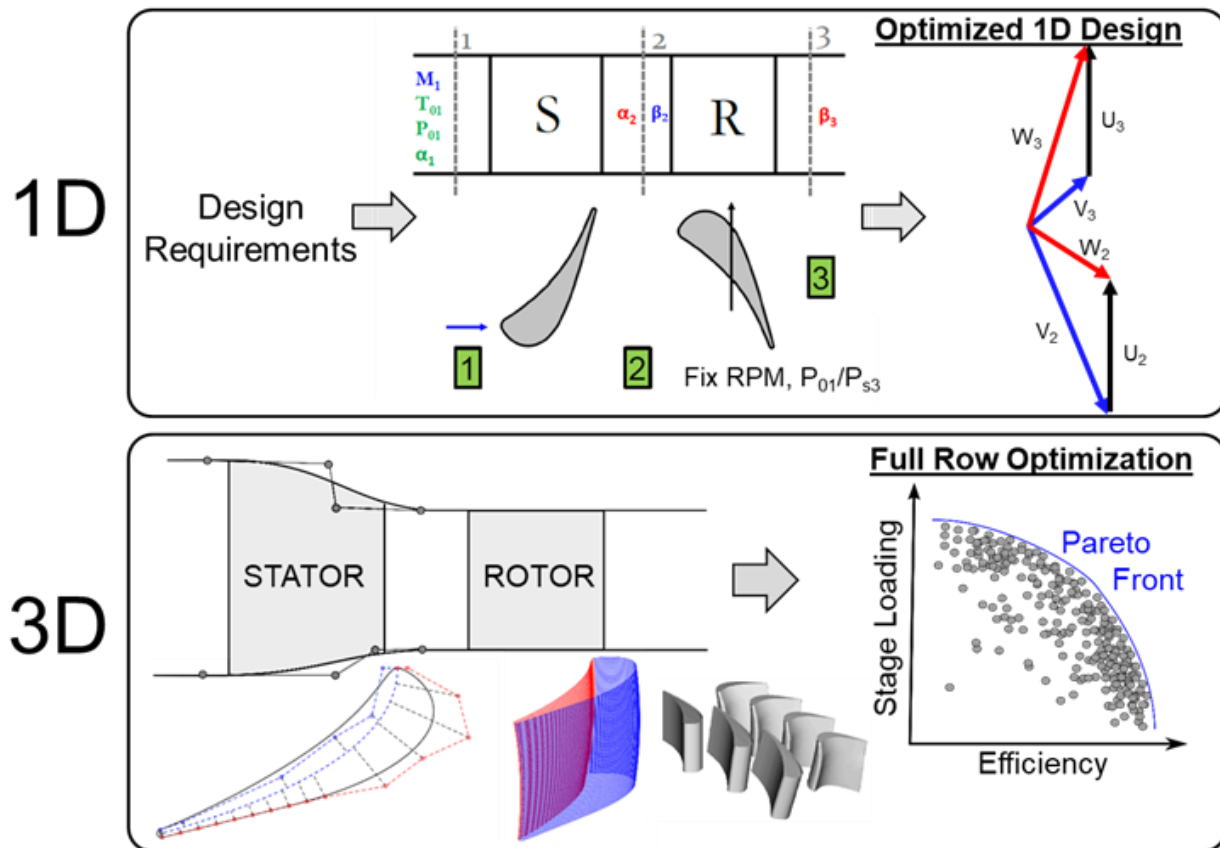


Figure 11: Overview of the turbine stage optimization strategy

3.2 1D Optimization Methodology

The 1D stage optimization consisted of an in-house developed 1D MATLAB mean-line solver. The solver accepts inputs of a total pressure (P_{01}) and total temperature (T_{01}) at the inlet, rotational speed (RPM), total-to-static pressure ratio (P_{01}/P_{s3}), inlet Mach number (M_1), and degree of reaction (r_p). Geometrical constraints include inlet height (H_1), and ratio of channel heights (i.e. H_2/H_1 and H_3/H_2). The inlet and outlet blade metal angles (α_2 and β_3) were iterated upon to balance the mass-flow through the stage. An axial inflow angle ($\alpha_1 = 0$), moderate stator and rotor efficiencies (respectively 92.5% and 87%), and constant gas properties were used. Constraints included an upstream total pressure of 5 bar and the rotational speed was fixed to 7500 RPM to maintain the structural integrity of the future rotating assembly.

The optimization routine was paired with a multi-objective differential evolution optimizer to explore a large, 7-dimensional design space; which allowed the pressure ratio to vary from 3 to 5, the inlet Mach number from 0.1 to 0.3, the degree of reaction from 0.25 to 0.75, and the total inlet temperature from 500K to 700K based on the capacity of the upstream air heater. The remaining 3 degrees of freedom are the turbine inlet height which varied from 40mm to 63mm and the channel height ratios, H_2/H_1 and H_3/H_2 , varied from 1 to 2 and 0.5 to 1.5, respectively. The mean radius was constrained by the dimensions of the tunnel and was held at a constant of 389mm.

To exclude aerodynamically unfeasible designs, constraints were set for the flow angles and velocities based on prior turbine design knowledge. The passage height was restricted to 420mm. The airfoil's exit metal angles, α_2 and β_3 , were limited to 80 deg., the relative rotor inlet angle β_2 to 40 deg., and a maximum allowed turning of 120 deg. in the rotor passage was imposed. To avoid high supersonic designs, the outlet Mach numbers, M_2 and M_{3r} , were constrained to 1.3 and 1.05, respectively, while M_{2r} was kept below 0.42. Furthermore, mass-flow was limited to a maximum of 30 kg/s based on the capacity of the upstream high-pressure vessels and downstream dump tank. The target was to simultaneously maximize the stage loading (Equation 7) and stage efficiency (Equation 8).

$$\psi = \frac{h_{01} - h_{03}}{U^2} \quad (7)$$

$$\eta_{adiabatic} = \frac{\dot{W}_{shaft}}{h_{01} - h_{03ss}} = \frac{Torque * \omega}{Torque * \omega + T_3(s_3 - s_1)} \quad (8)$$

This work uses the adiabatic efficiency as a figure of merit, specifically the ratio of extracted work to what would be isentropically possible with adiabatic boundary conditions. Therefore, the associated entropy production caused by heat transfer to the airfoils and end-walls can be neglected. In case isothermal simulations would be performed, the heat dissipated across the airfoils, hub and casing end-walls ought to be considered, by subtracting the energy lost through heat transfer from the actual drop in total enthalpy across the stage using equation 9.

$$\eta_{isothermal} = \eta_{adiabatic} + \frac{\dot{Q}_{stage}}{h_{01} - h_{03ss}} - \frac{T_{03}}{h_{01} - h_{03ss}} \left[\frac{\dot{Q}_{stator}}{T_{01}} + \frac{\dot{Q}_{rotor}}{\frac{1}{2}(T_{02} + T_{03})} \right] \quad (9)$$

De Maesschalck et al. [80], based on the work of Yasa et al. [81], and Atkins and Ainsworth [82] demonstrated the use of this correction to compare adiabatic with isothermal simulations, considering the temperature at which the heat transfer takes place for the entropy creation.

3.3 3D Optimization Strategy

The full 3D row optimization was implemented through an automatic evaluation routine written in BASH. The routine launched a MATLAB tool that created the 3D geometry using 75 parameters that defined the stator and rotor blades and hub and shroud curves. The 3D geometry is exported to a GeomTurbo file where it is read by the mesh generator, Numeca Autogrid. The mesh is solved using FINE/Turbo and post processed in CFView (Figure 12). The two optimization objectives: the entropy definition of efficiency (Equation 8) and stage loading (Equation 7) were extracted using Numeca CFVIEW and fed back into the optimizer. The entropy definition was used to reveal the effect of entropy on the overall turbine performance.

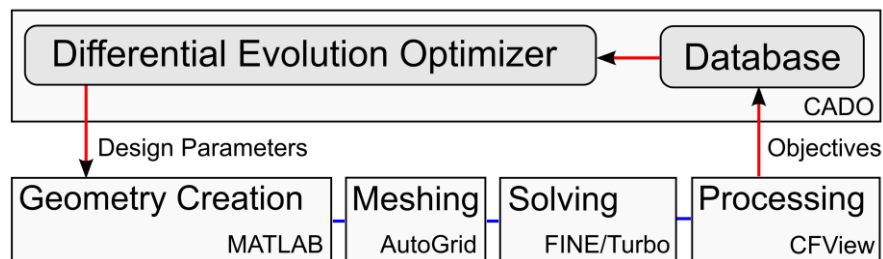


Figure 12: Overview of the 3D optimization structure

3.4 Parameterization Strategy

3.4.1 2D Parameterization

The 2D blade was constructed in the radius, tangential, axial (RTZ) coordinate system. The 2D profile was defined using a camber-line and an independent parameterization of the suction and pressure sides. Compressor airfoils are usually defined with only a camber-line and one thickness distribution, with high flexibility and a lower number of variables. However, in transonic airfoils the local curvature of the rear suction side is particularly important, which requires an unconstrained shape for pressure side and suction side, which results in a few more parameters. Both the pressure and suction sides were defined using Bezier curves by assigning control points at distances perpendicular to the camber line (Figure 3-right). In the stator suction side, points 1-6 were spaced using an expansion ratio of 1.2, the points covered 60% of the camber-line. The remaining 40% of the camber-line was straightened out using 10 automatically spaced control points to maintain gradual diffusion. In the current transonic turbine design, the rear suction side was kept flat based on our design experience [83]. The camber-line was constructed by 3 points that define the inlet (α_1, β_2) and outlet (α_2, β_3) metal angles. The stagger angle (γ) and axial chord (C_{ax}) determines the position of point 1. Throughout the optimization, the stator inlet flow angle, α_1 , was fixed to zero while the other blade metal angles, as well as the chord and stagger angle, were allowed to vary.

The pressure side was constructed from 5 control points (excluding the points at the leading edge and trailing edge) spaced using the same expansion ratio. The thickness of the point 1 on the pressure side was adjusted perpendicular to the metal angle to match the second derivative of the suction side at the beginning of the leading edge. The last point, 5, was fixed at 90% of the camber line. The thickness near the trailing edge along the pressure side was determined by the pressure side wedge angle. Finally, the trailing edge connected the two blade sides through a circle segment with a diameter of 1 mm.

Similar types of parametrization strategies have been successfully used in several prior studies and allows for the generation of a wide variety of turbine profiles [60,84]. This 2D parametrization gave rise to a total amount of 12 and 14 design variables for the stator and rotor, respectively. In the case of the stator, the blade profiles were parameterized at the hub and tip sections while the rotor included an additional profile at mid-span.

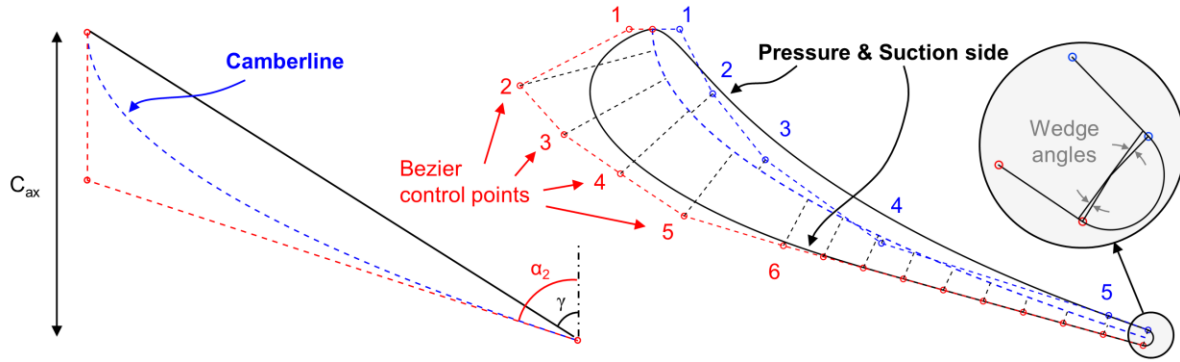


Figure 13: 2D Parameterization strategy for the blade profiles in the 2D cascade planes

3.4.2 3D Parameterization

The 3D geometry was designed by stacking 2D profiles at fixed percent spans. Two profiles were used to stack the stator and 3 profiles were used for the rotor. An illustration of the procedure is presented in Figure 14 for the rotor blade. First, 100 intermediate profiles along the spanwise direction were defined. This was accomplished by fitting splines through each point along the suction and pressure sides of the profiles. Intermediate profiles were obtained by discretizing the splines. Blade lean was applied by constructing a Bezier curve from hub to tip through either the centroid or leading edge (Figure 14-b). This determined the tangential shift of the 2D blade profiles and the intermediate profiles (Figure 14-a). The Bezier curve was defined by 3 control points at the hub, midspan, and tip; the upper two points could move along the peripheral direction to induce lean by as much as 15% of the blade span. Positive lean is lean towards the suction side and negative lean is towards the pressure side. After the lean had been applied, the 3D blade was placed inside the turbine channel with an inter-row spacing of one third of the axial stator hub chord. Each intermediate profile was eventually rescaled radially to fit the local shroud and hub curvature.

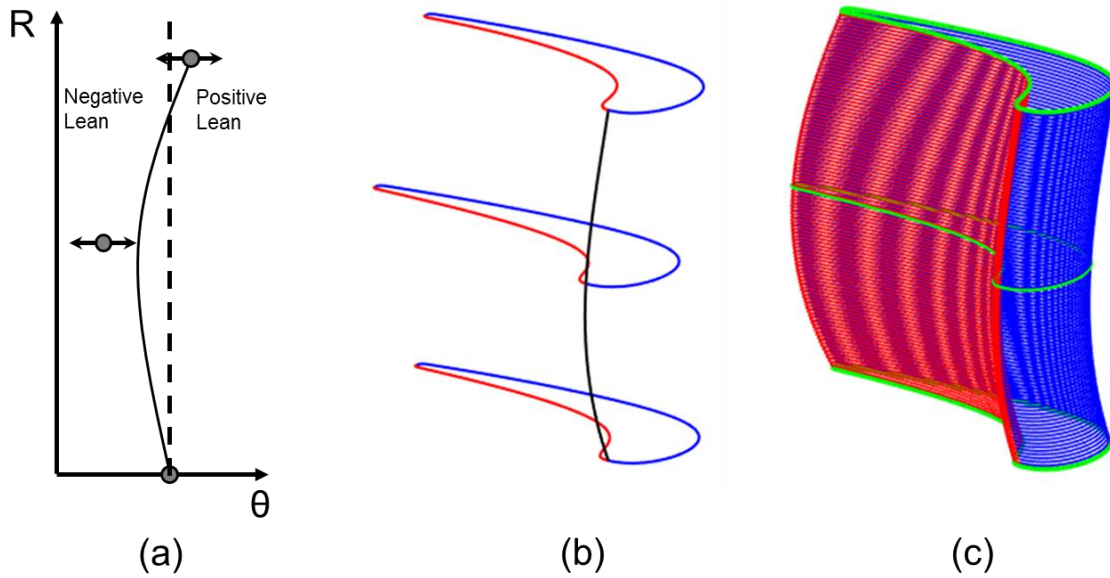


Figure 14: Three-dimensional stacking of the blade profiles through a lean distribution

The strategy for the channel parameterization is presented in Figure 15. The hub and shroud contours were constructed using 3 cubic Bezier curves and a straight line over the rotor shroud. Intermediate points 1, 2, and 3 were fixed axially at the stator and rotor mid-chords and were determined radially by the channel spans H_1 , H_2 and H_3 . To control the local curvature, points 4, 5 and 6 could move axially from the profiles mid-chord all the way up to the vicinity of the stator-rotor interface.

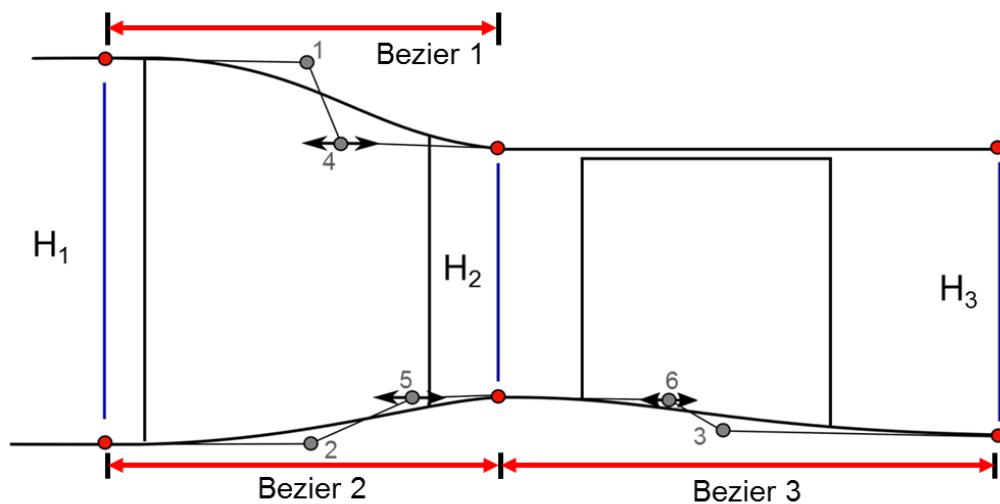


Figure 15: Channel Parameterization

3.4.3 Blade Count Selection

In this chapter, the number of blades was not part of the optimization. Instead, several factors influenced the selection of the number of blades: The axial chord requirement for both stator and rotor blades could not exceed 45mm; the aspect ratio was limited by the inlet height from the 1D design. The strategy was to choose the number of blades while being able to explore a wide range of pitch-to-chord and aspect ratios. For this analysis, 41 stator and 61 rotor blades were chosen. This allowed the stator's pitch-to-chord ratio to vary from 0.7 to 0.94, and aspect ratios (H/C) of 0.47 to 0.68. The rotor's pitch-to-chord ratios ranged from 0.65 to 0.85 and aspect ratios of 0.7 to 1.2, simply by varying the axial chord and stagger angle of each blade.

3.5 Computational Domain and Grid Sensitivity

The computational domain (Figure 16) was created in Numeca Autogrid, containing a periodic section of the stator and rotor passages connected through a mixing plane. The blade height was divided radially into 117 and 141 sections for the stator and rotor, respectively. To account for tip clearance, 37 spanwise cells were defined within a rotor tip gap of 0.4mm. An O4H structured topology is used to mesh the blades in the cascade plane. The stator contains 193 cells along the suction side and 97 cells on the pressure side. The rotor was discretized using 257 and 97 cells, respectively. The y^+ was kept below unity using an initial cell size of 1 micrometer combined with an expansion ratio of 1.3 resulting in a total mesh count of 7.8 million cells.

The steady Reynolds-Averaged Navier-Stokes simulations were performed using Numeca FINE/Turbo with Menter's Shear-Stress Transport model for the turbulence closure [59]. The working fluid was dry air modeled as a real gas, incorporating temperature dependent properties. Total temperature and pressure were imposed at the domain inlet while a fixed static pressure was set at the outlet, satisfying the radial equilibrium. A turbulence intensity of 2.5% and length scale of 5% of the blade span were used for the inflow conditions and all walls were considered adiabatic. At the stator-rotor interface, a conservative coupling strategy of the pitch-wise averaged quantities was employed.

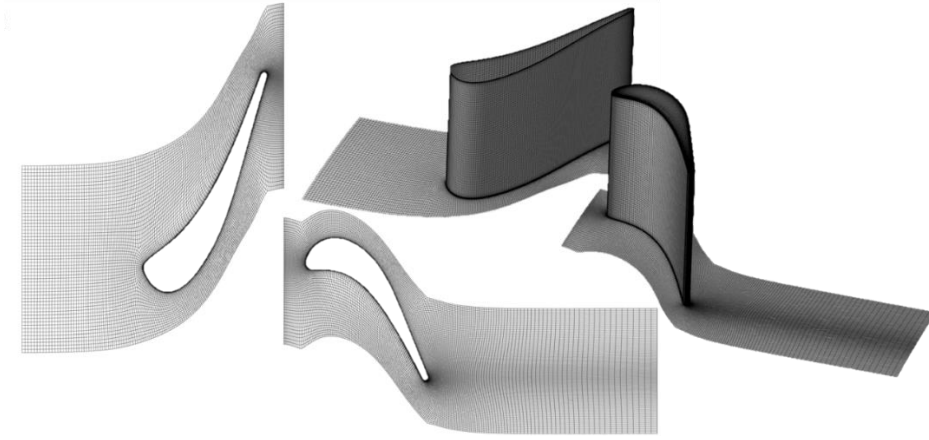


Figure 16: Computational Domain

To verify the final grid size for the optimization, a thorough mesh sensitivity study was performed for both the stator and rotor separately using an average baseline geometry. The rotor sensitivity study was performed by simulating with a fixed stator mesh while the stator grid was refined without the effects of the rotor, applying the appropriate vane back pressure from the stage calculations. Table 5 presents the details of the four different grids applying consecutive refinements in every direction. The results of the mesh sensitivity analysis are shown in Figure 17, where the stator (a) and rotor (b) relative pressure losses are presented along the radial direction. Based on the observed similarity between the ‘Fine’ and ‘Finer’ mesh results, the characteristics of the ‘Fine’ mesh are deemed sufficient to be used throughout the optimization.

Table 5: Stator and rotor grid sensitivity configuration

Stator/Rotor	Mesh size	Spanwise divisions	Suction side	Pressure side
Coarser	1.5 / 1.5M	81 / 81	133 / 177	65 / 65
Coarse	2.4 / 2.2M	97 / 97	161 / 213	81 / 81
Fine	3.4 / 4.4M	117 / 141	193 / 257	97 / 97
Finer	5.6 / 7.0M	141 / 169	233 / 309	113 / 117

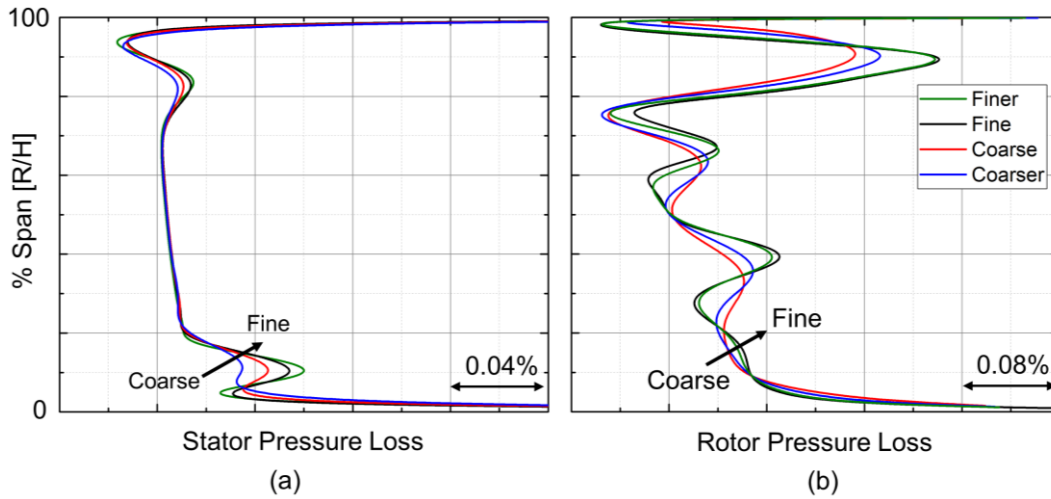


Figure 17. Stator and rotor pressure losses for 4 mesh of the grid sensitivity analysis

The calculation of efficiency requires calculating the entropy change across each blade row (Figure 19). The entropy change across the stator was evaluated as the difference between the values obtained at planes 1 and plane 2, the stator outlet plane (2a) is located upstream of the mixing plane. At each plane, the values are the result of the integral along all the area, weighted by the local mass-flow in each cell, according to the method of Denton and Pullam [85]. Entropy change across the rotor was evaluated as the difference between the values obtained at planes 2b and the rotor exit plane 3., The rotor inlet plane (2b) is located downstream of the mixing plane. Figure 18-a shows the change of entropy across the stator. Figure 18-b displays the change of entropy across the rotor, as a function of the grid size. The relative error in entropy for the fine mesh for the stator is 0.7% from the finest mesh. For the rotor, the relative error fine from finest mesh is less than 0.14%.

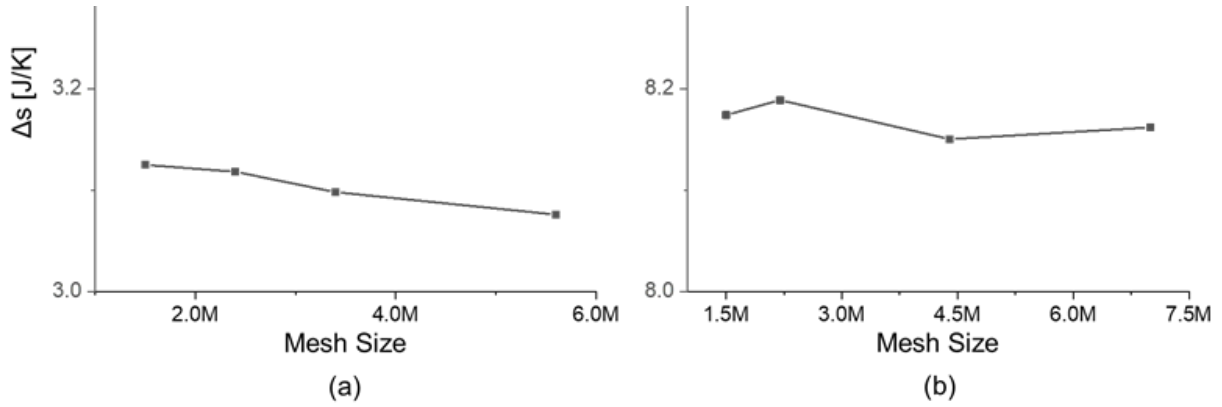


Figure 18. Effect of mesh size to the entropy creation across each row: (a) Stator; (b) Rotor.

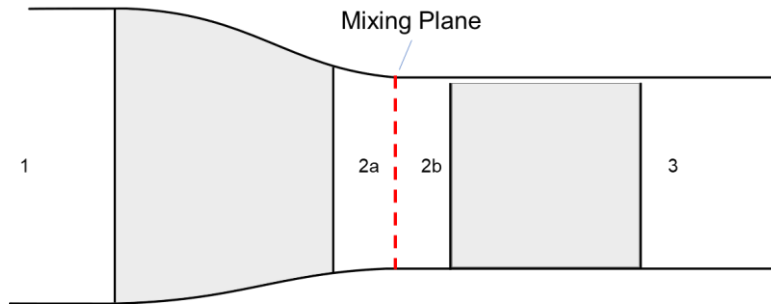


Figure 19. Turbine stage Efficiency calculation locations

3.6 Optimization Setup

Table 3 shows the evaluation space for both the 1D and 3D optimizations. The 1D optimization was seeded by evaluating 80 randomly selected individuals. Mutation and crossover were used on the parameters defining those 80 individuals to generate the next population with a size of 40 individuals. The recommended population size is 2 to 10 times the number of parameters [86]. The number of populations was determined by stopping the simulation once a pareto front was identified. The 3D optimization, on the other hand, had a large design space, and a fractional factorial [87] approach was used to initialize a database containing 256 individuals selected to cover 10% and 90% of the design space. From this set of individuals, the multi-objective optimization was started with a population size of 30 individuals. This population size facilitated a balance between a fast iteration turnover time and the ability to capture a sufficient amount of geometrical variability within each population.

Table 6. Optimizer constants for both 1D and 3D optimizations

	1D	3D
# Parameters	7	75
Design of Experiments	80	256
Population size	40	30
Populations Evaluated	35	15

3.7 1D Optimization Results

Figure 20-left presents the results of the 1D optimization, yielding 760 feasible designs obtained from 35 optimization populations. The axes depict the two objectives: the simultaneous maximization of the aerodynamic efficiency and blade loading. The configurations from the first 20 populations (grey markers) largely scatter around the design space, the turbine stages from the final 5 iterations (red markers) are confined along a Pareto front (red curve) scoping about 3% in efficiency and span stage loadings from 1.2 up to more than 1.7.

The velocity triangles of the eventually chosen target configuration (indicated with a yellow diamond) is presented in Figure 20-right. This design features the highest stage loading (1.74) satisfying all constraints while delivering a total power of 3.64 MW. The degree of reaction of the selected case is 0.39 with a pressure ratio of 4 and an inlet temperature of 676K. The turbine has a turning angle of 107 deg. while the stator outlet angle is 73 deg. Both the vane and blade exit Mach numbers, 0.89 (M_2) and 1.05 (M_{3r}), are in the high subsonic-transonic regime while both the stator and rotor passage heights are increasing with 16% and 32% respectively. The latter optimized design parameters were used as a starting point to set the geometrical ranges for the 3D optimization and are summarized in Table 7.

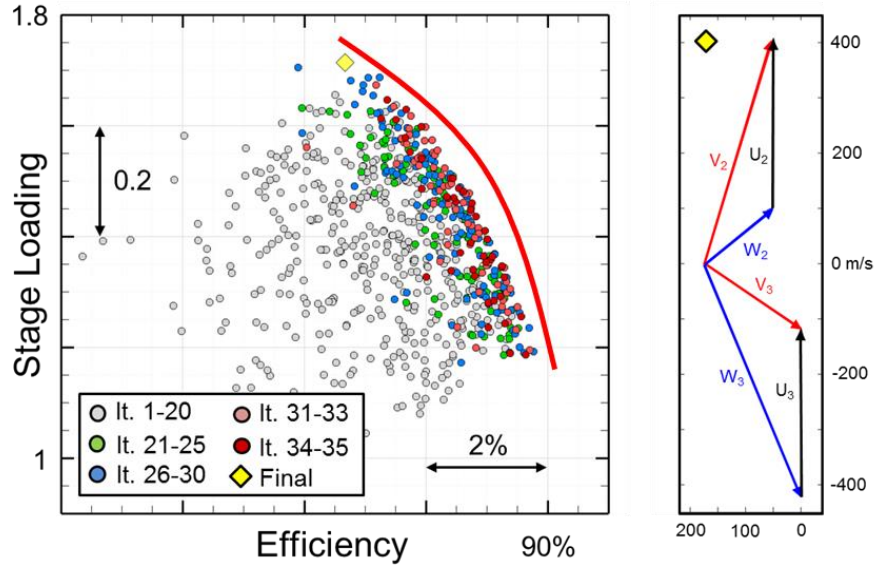


Figure 20. Left: 1D optimization results. Right: chosen design.

Table 7. Characteristics of 1D Final Design

Flow Angles		Performance			Mach Number	
α_2	73	Power	MW	3.64	M_2	0.89
α_3	-33	Massflow	kg/s	22.8	M_{2r}	0.34
β_2	39.3	Degree of Reaction	-	0.39	M_3	0.48
β_3	-67.7	Stage Loading	-	1.74	M_{3r}	1.04
		T_{01}	K	676		

3.8 3D Optimization Results

3.8.1 Pareto Front

The 3D optimization ran for 15 generations (Figure 21-left). Each circle on the plot represents a unique combination of stator, rotor, and channel. Throughout the optimization, the individuals move to regions of high efficiency and stage loading. The Pareto front represents the limit where if a geometry wanted to improve stage loading, a sacrifice in efficiency would have to be made. Optimal designs along the Pareto front are indicated with letter A through E. The baseline profile is marked diamond. The individuals are colored by the degree of reaction (r_p).

On the right of Figure 21, the same design space is colored with the rotor turning angle ($\Delta\beta$). Individuals with higher efficiency contain higher degrees of reaction and have lower turning. However, designs with higher stage loading, feature lower degrees of reaction and more turning. Degrees of reaction in the 0.3-0.35 range with turning up to 120 degrees represent the top right of the pareto front.

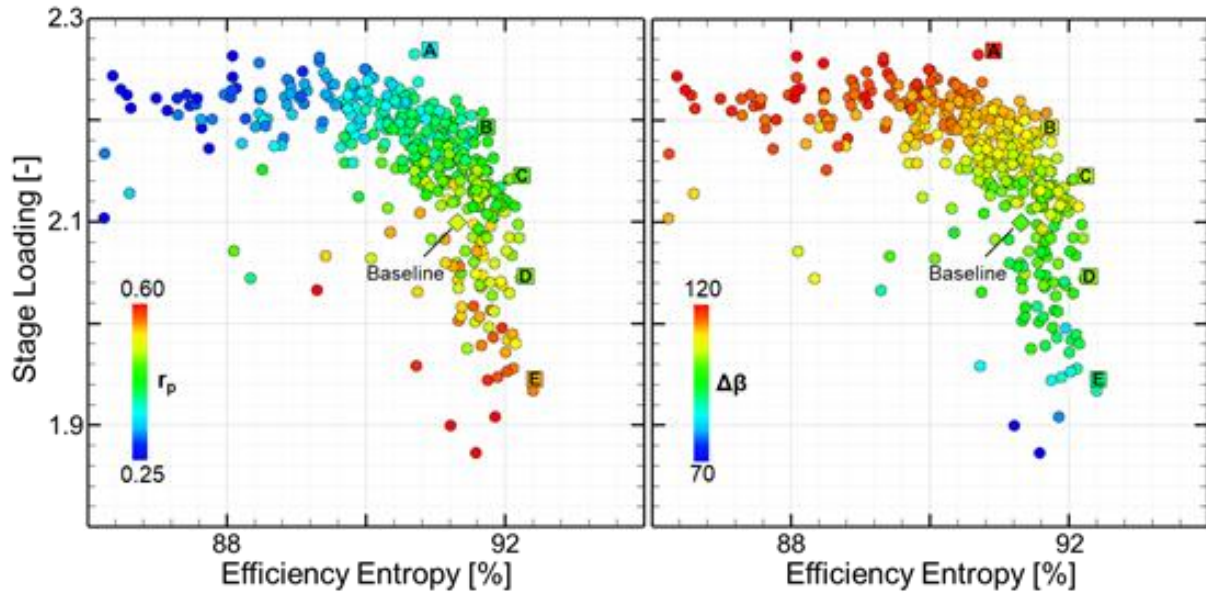


Figure 21: Pareto Front (left) and colored by the degree of reaction and turning angle (right)

3.8.2 Trends in Stator Loss Generation

Figure 22 compares stator entropy loss coefficient [8] (Equation 10) with stator turning (left) and pitch-to-chord ratio (right).

$$\zeta_s = \frac{T_2 \Delta s}{h_{02} - h_2} \quad (10)$$

The lower region of the Figure 10-left features designs of high degree of reaction, which results in less turning and lower exit Mach numbers (M_2). The upper regions are characterized by low degree of reactions which results in more turning of the stator and have higher exit Mach numbers. Losses can be kept as low as 0.6% if one limits the stator turning to 76 deg. and a degree of reaction above 0.4.

Figure 22-right compares the entropy loss with geometry properties, pitch-to-chord ratio and stagger angle. Stators with lower loss have lower stagger angles closer to the minimum value and higher pitch-to-chord ratios. However, stators with higher turning have pitch to chord ratios

below 0.85 to provide guidance, but they generate more loss. No clear optimal trends were observed in terms of lean distribution or suction side wedge angle for the simulated configurations.

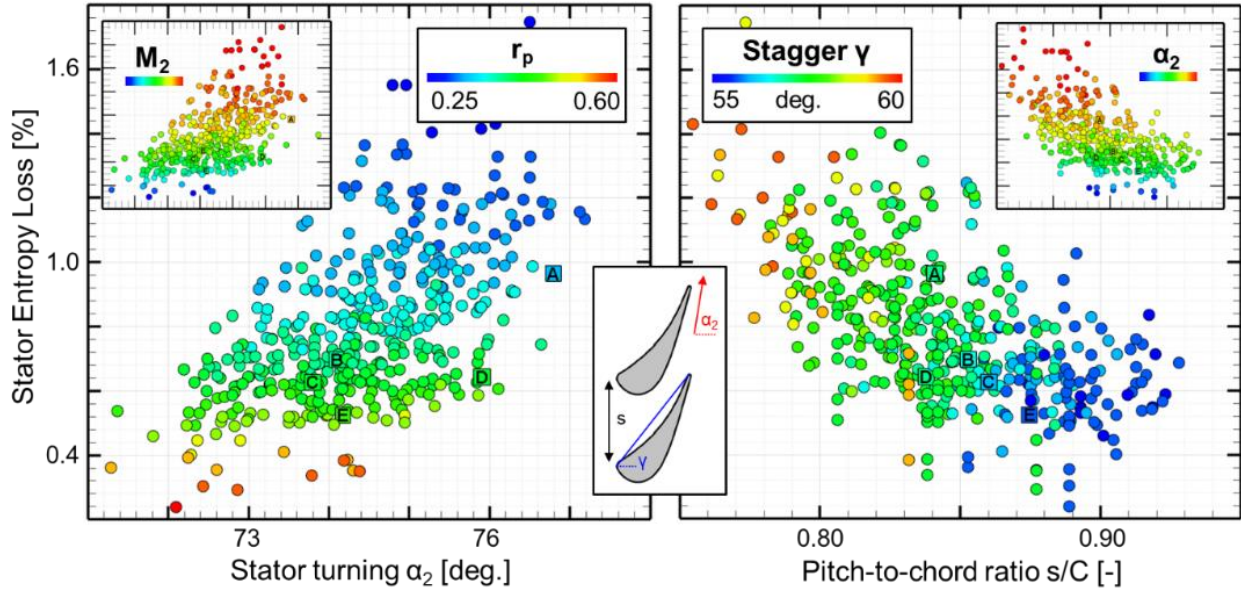


Figure 22. Left: Relation of the stator losses with the aerodynamic quantities. Right: Geometrical characteristics.

3.8.3 Trends in Rotor Loss Generation

Figure 23 presents the effect of several aerodynamic and geometrical features on the rotor entropy loss coefficient (Equation 4). The left graph illustrates the effect of the rotor turning on the losses. The left portion of the graph shows low turning angles which results in high exit relative Mach numbers and as a consequence, a larger degree of reaction. This results in a lower incoming absolute flow velocity from the stator. Through a proper optimization of the rotor geometry, the losses can be limited to about 10% up to a turning angle of 110 deg. From this point on, as the turning increases, the losses start to increase significantly up to 15% for a turning angle of 125 deg.

The right graph of Figure 23 illustrates the lean distribution for the optimal profiles along the Pareto front, colored in yellow. The vertical axis identifies the lean at 100% span and in abscissa the lean at 50% span. The baseline design used in the grid sensitivity is marked with a green diamond showing no lean. The majority of the optimal profiles that display the best efficiency

show positive lean at 100% span in order to off-load the tip section and negative lean in the mid-chord.

Similar to the stator, investigations on rotor loss with pitch-to-chord ratio contoured with the stagger angle γ was investigated. However, no apparent trend can be observed. It should be noted that the selected profiles along the Pareto front (A to E) are contained within a narrow band of the pitch-to-chord ratio of 0.7 to 0.75, the majority of the profiles feature stagger angles between 40 and 45 degrees.

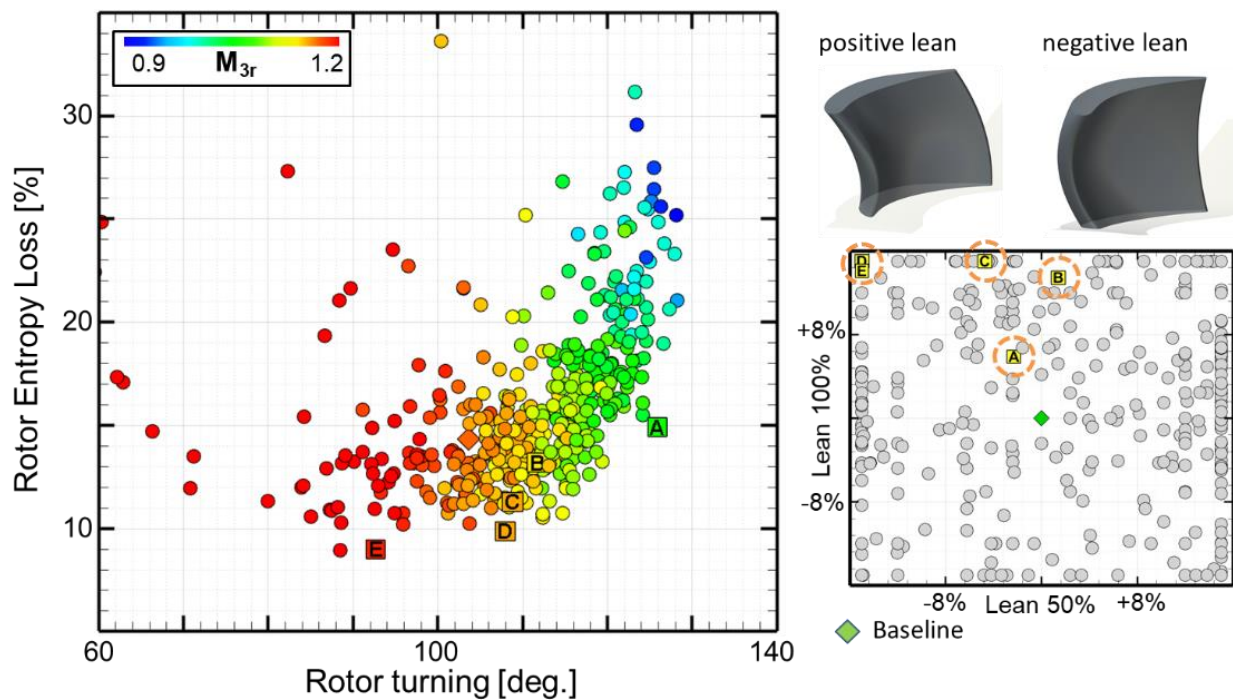


Figure 23. Left: Effect of the rotor turning. Right: The influence of the blade lean.

Highly loaded turbines are more desired because they extract more work per blade and thus reducing the number of airfoils in an engine. Their usage has been a challenge. Researchers have shown that highly loaded (front loaded) turbine airfoils produce the more profile and secondary flow loss than aft-loaded designs [9,13,14]. However, Lydall et al. [18] postulated that secondary flow loss can be reduced by lowering the stagger angle at the walls. The same principals can also be applied to high pressure turbines. In the dataset, design “A” has the highest loading, “E” is the most efficient design with the lowest loading. Figure 24 compares the rotor entropy loss coefficient with the stagger angle of the 3 rotor profiles defined at the hub, midspan, and tip.

Design “A” has the lowest stagger angle at the hub and tip which supports the work of Lydall et al. [18]. The highest efficiency design “E” shows the opposite trend, the stagger angle is highest near the walls, and lowest at the midspan.

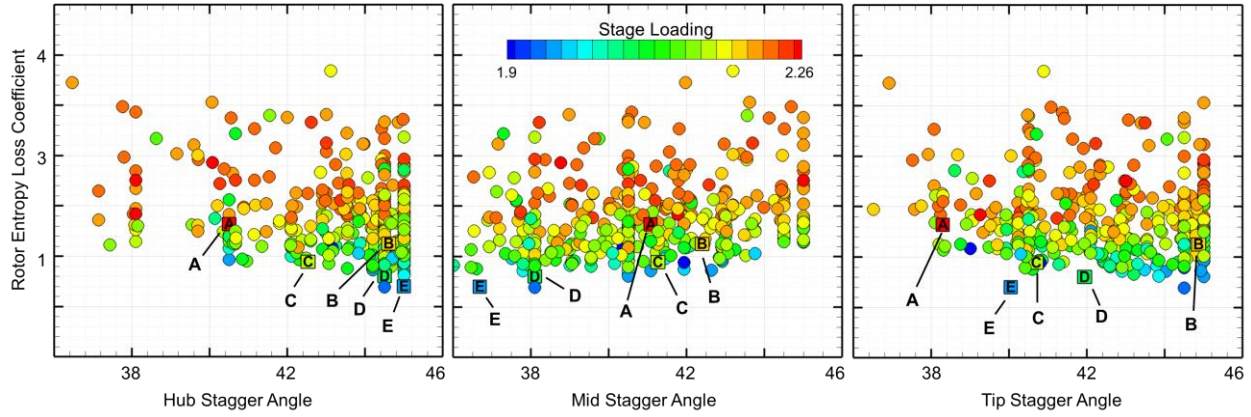


Figure 24. Rotor entropy loss coefficient vs. stagger angle. Left: Hub stagger angle. Mid: Mid profile stagger angle. Right: tip stagger angle

3.8.4 Horlock Efficiency

Horlock efficiency, commonly used in turbomachinery to evaluate the efficiency of a stage from the losses of the stator and rotor, relies on a couple of simplifications. Equation 11 begins the derivation of the horlock efficiency from the adiabatic efficiency. The loss expressed as the difference between total enthalpy at exit from the isentropic definition. The first assumption is that v_3 and v_{3ss} are equal, which however may result in errors for high speed turbines.

$$\eta_{adiabatic} = \frac{Power}{Power + \left(h_3 + \frac{v_3^2}{2} - h_{3ss} - \frac{v_{3ss}^2}{2} \right)} \cong \frac{Power}{Power + (h_3 - h_{3ss})} \quad (11)$$

The enthalpy loss can be related to the difference in entropy using the second law of thermodynamics. Then $h_{3s} - h_{3ss}$ is related to $h_2 - h_{2s}$ by the temperature ratio.

$$\begin{aligned} h_3 - h_{3ss} &= (h_3 - h_{3s}) + (h_{3s} - h_{3ss}) \\ h_{3s} - h_{3ss} &\cong T_3(s_{3s} - s_{3ss}) \\ h_2 - h_{2s} &\cong T_2(s_2 - s_{2s}) \end{aligned} \quad (12)$$

$$h_{3s} - h_{3ss} \cong \frac{T_3}{T_2}(h_2 - h_{2s}) \quad (13)$$

Substituting equation 13 into 11 results in the definition of Horlock efficiency

$$\eta_{adiabatic,Horlock} = \frac{Power}{Power + (h_3 - h_{3s}) + \frac{T_3}{T_2}(h_2 - h_{2s})} \quad (14)$$

$$h_2 - h_{2s} = \frac{V_2^2}{2} \xi_{stator}$$

$$h_3 - h_{3s} = \frac{W_3^2}{2} \xi_{rotor}$$

Figure 25-left shows the pressure loss of the rotor as a function of the entropy definition of efficiency as obtained using Equation 3, and the individuals are contoured with the percentage of rotor loss from the total loss of both blades. As the efficiency of the designs increase, pressure loss decreases, and the percentage of rotor loss from the total pressure loss reduces to 60%. The slope is approximately 3% of rotor loss for about 1% of stage efficiency gain.

The middle plot in Figure 25 presents the comparison of the entropy efficiency (Equation 11(11)) with the efficiency approximated using the Horlock equation (Equation 14). The Horlock equation is used in experiments and simulations to provide an estimate for the total efficiency of the stage, based on the measured kinetic loss of the flow. The kinetic loss for the stator was computed from the mass-flow average relative velocity, V_2 , extracted at the exit of the stator (Equation 15). Similarly, for the blade losses, the mass-flow average relative velocity, W_3 , was taken at one half the axial chord downstream of the rotor.

$$\xi_{stator} = \frac{V_{2s}^2 - V_2^2}{V_2^2} \quad (15)$$

$$\xi_{rotor} = \frac{W_{3s}^2 - W_3^2}{W_3^2} \quad (16)$$

Figure 25-right illustrates the comparison of both efficiency definitions. The corrected Horlock efficiency definition (Equation 17) was evaluated on a dataset of 416 different designs, and the resulting error has a mean value of 0.01%, $\pm 0.007\%$ with a confidence level of 95% from the entropy definition of stage efficiency.

$$\eta_{adiabatic,Horlock\ corr} = \eta_{adiabatic,Horlock} - 0.0562(M_{3r} - 1.057) \quad (17)$$

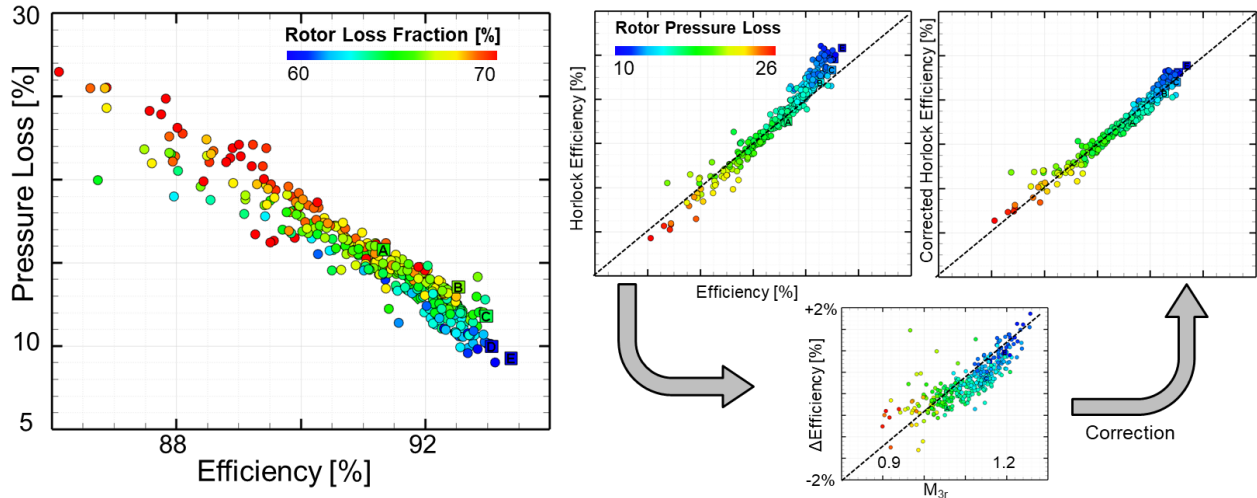


Figure 25. The stage efficiency in function of the aerodynamic losses (left) and the compensation strategy for the Horlock efficiency equation (right).

3.8.5 Analysis of Optimal Profiles

Profiles of the stators along the pareto front are compared in Figure 26 Profile A has the highest stage loading of 2.26 with an efficiency of 91.3%, the degree of reaction is 0.33. Profile E shown at the bottom of Figure 13 is the highest efficiency design and has a maximum efficiency of 93.3%, stage loading of 1.94, and a degree of reaction of 0.54. Highly loaded stators feature high turning from hub to tip. More efficient designs have less turning at the tip and their tip profiles are smaller. Additionally, as designs go towards higher efficiency, the stagger angle is reduced from 58 to 55 degrees and turning angle is also reduced. The suction side wedge angle decreases from 5 to 2 degrees. The channel shown on the right of Figure 26 flow moves from left to right. The red represents the stator and blue, the rotor. The channel has a high expansion ratio for highly loaded designs, i.e. Design A has an initial expansion ratio of 1.2 from stator inlet to stator exit and from stator exit to rotor exit the ratio is 1.28. The expansion ratio decreases as one moves towards designs of higher efficiency.

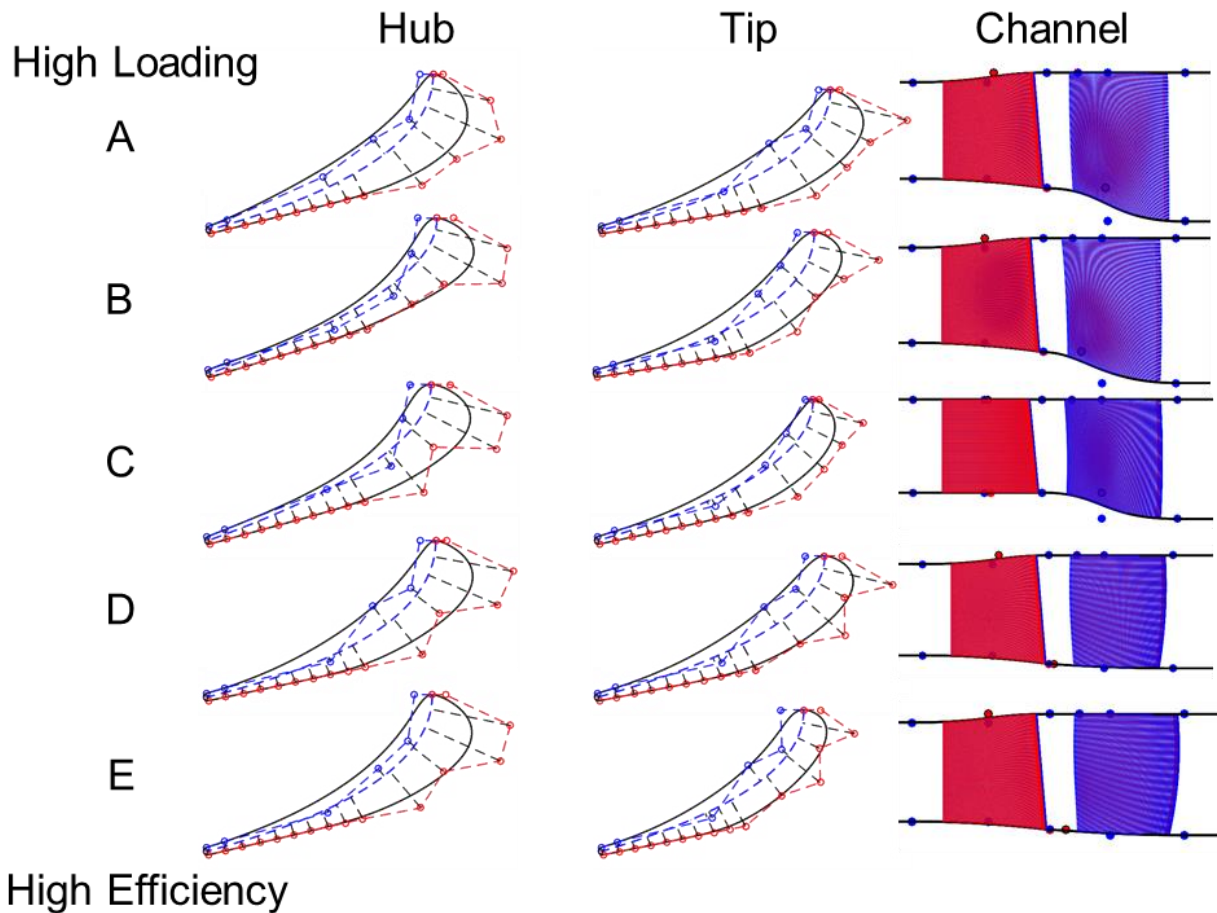


Figure 26. Stator optimal profiles and channel geometry

The highest loading design, profile A, is displayed in Figure 27-top and shows a larger change in thickness as opposed to profile E. The thickness of both the stator and rotor blades increases from hub to tip and so does the turning. Figure 27 compares rotor designs along the pareto front. Design A has the most loading, and it turns 19.5 kg/s of air 125 degrees through the turbine extracting 3.6MW. The maximum efficiency geometry, design E, turns 22.5 kg/s of flow 92 degrees and extracts 3.52MW. Design A's profile is thicker near the tip, and β_3 also increases from 66 to 74 deg at tip. However, β_2 decreases from 40 deg at hub to 38 at the tip. Higher loading designs typically feature fatter profiles at the tip with more turning. More efficient designs on the other hand, have higher turning at the hub and less at the tip. In design E, the inlet metal angle β_2 varies along the span from 38 to 43 to 38 degrees at the tip. β_3 shows a different trend. It decreases from the hub to midspan, 73 to 65 degrees and slightly increases at the tip to

66 deg. In contrast, the suction side wedge angle fluctuates from 3 to 5 deg, then back to 3 deg. at the tip.

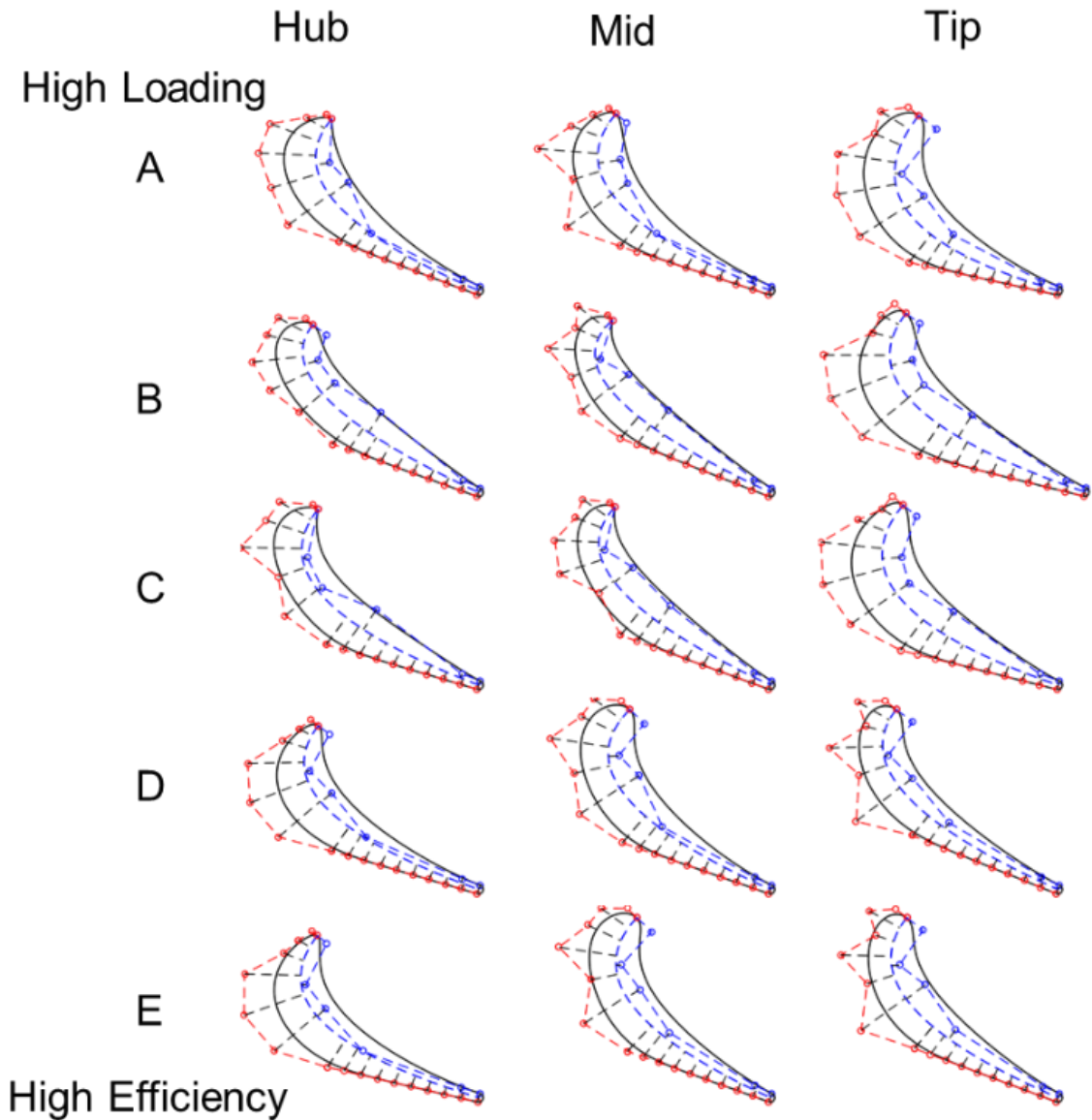


Figure 27. Rotor optimal profiles

Isentropic Mach plots provides a precise non-dimensional estimation of the airfoil loading. Figure 28 compares the isentropic Mach number at the rotor midspan with the tip for 3 designs along the pareto front. Highly loaded designs have increased loading near the front of the blade followed by diffusion and re-acceleration of the flow until it leaves the trailing edge. This is true

for both hub and tip. Designs with lower stage loading are less front loaded and more aft-loaded and have higher exit Mach numbers and large diffusion near the trailing edge.

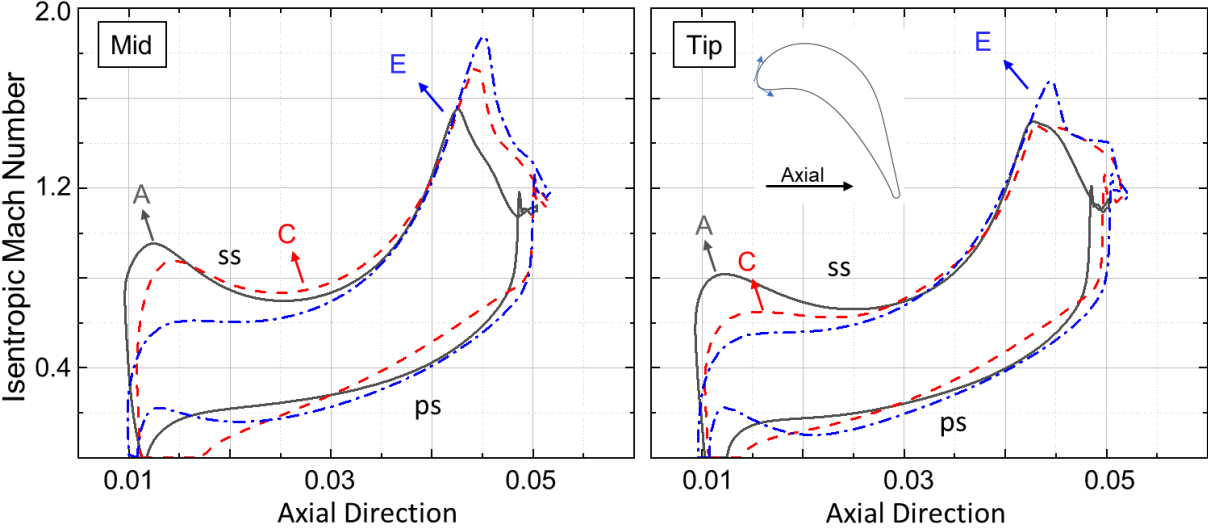


Figure 28. Rotor Isentropic Mach number. Left: Mid span. Right: Tip.

4 BIO-INSPIRED TURBINE FOR OFF-DESIGN PERFORMANCE

4.1 Wavy Blade Design Methodology

The methodology described in Figure 29 aims to answer the question, “what happens when we take an already optimized airfoil that is front loaded and evaluate its performance at positive incidence, it is possible to improve the efficiency by applying nature inspired waves?” To answer this, a highly loaded turbine derived from the previous chapter was used as a baseline geometry (Figure 30). The optimizer uses an evaluation routine that takes the baseline geometry and applies waves using a modified version of the in-house turbine design program from the previous chapter. The airfoil is then meshed using a structured O4H grid and solved at positive incidence. Pressure loss and flow exit and inlet quantities such as the flow angle (β_2), incoming and exit mach number, massflow, and exit flow angles were extracted. Careful consideration was made to ensure the massflow, stage loading, and turning angle remained constant. The target of the optimization is to find the ideal wave combination that reduces pressure loss (Equation 21). The effects of tip clearance were not considered for this study and are suggested for future work.

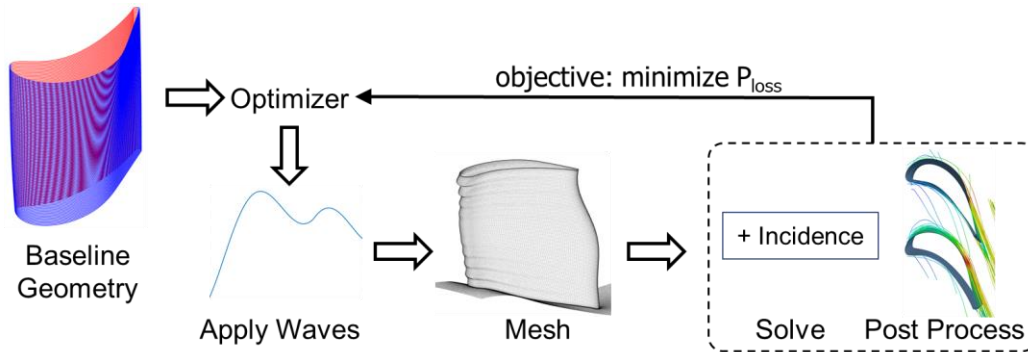


Figure 29. Wavy blade design methodology



Figure 30. Baseline rotor. Left: suction side. Right: pressure side

4.2 Boundary Conditions

To simulate incidence, static pressure, temperature, and specific heat were exported from the stator outlet and used to re-compute rotor inlet total relative pressure (P_{02R}), total relative temperature (T_{02R}), and yaw angle (β) (Equations 18-20) at positive 15 degrees incidence. The pitch angle was not modified. Figure 3 shows the pitch-wise average variations of P_{0R} , T_{0R} , and flow angles at the inlet of the rotor.

$$W_2 = \frac{W_{ax}}{\cos(\beta_2)} \quad (18)$$

$$T_{02R} = T_2 + \frac{W_2^2}{2cp} \quad (19)$$

$$P_{02R} = P_2 \left(\frac{T_{02R}}{T_2} \right)^{\frac{\gamma}{\gamma-1}} \quad (20)$$

$$P_{loss} = \frac{P_{02R} - P_{03R}}{P_{02R} - P_3} \quad (21)$$

Scaled conditions result in Mach numbers up to 0.75 entering the rotor. Table 8 list massflow-weighted flow angles and inlet Mach numbers for the baseline blade at design (7500RPM) and off-design (4000RPM). By operating at a reduced RPM, the total relative pressure increases which causes the Mach number entering the rotor to be transonic. The stage

loading increases from 2.26 to 5.91. Reynolds number was calculated using the axial chord of the rotor and remains the same for both incidence angles. Figure 31 compares the inlet boundary conditions of the design point with positive incidence.

Table 8. Inlet boundary conditions and outlet quantities

Incidence	RPM	β_2	M_{2R}	β_3	M_{3R}	Re_{exit}
0	7500	-55	0.41	70.8	1.06	8.3E5
+15	4000	-70	0.75	70.0	1.14	8.3E5

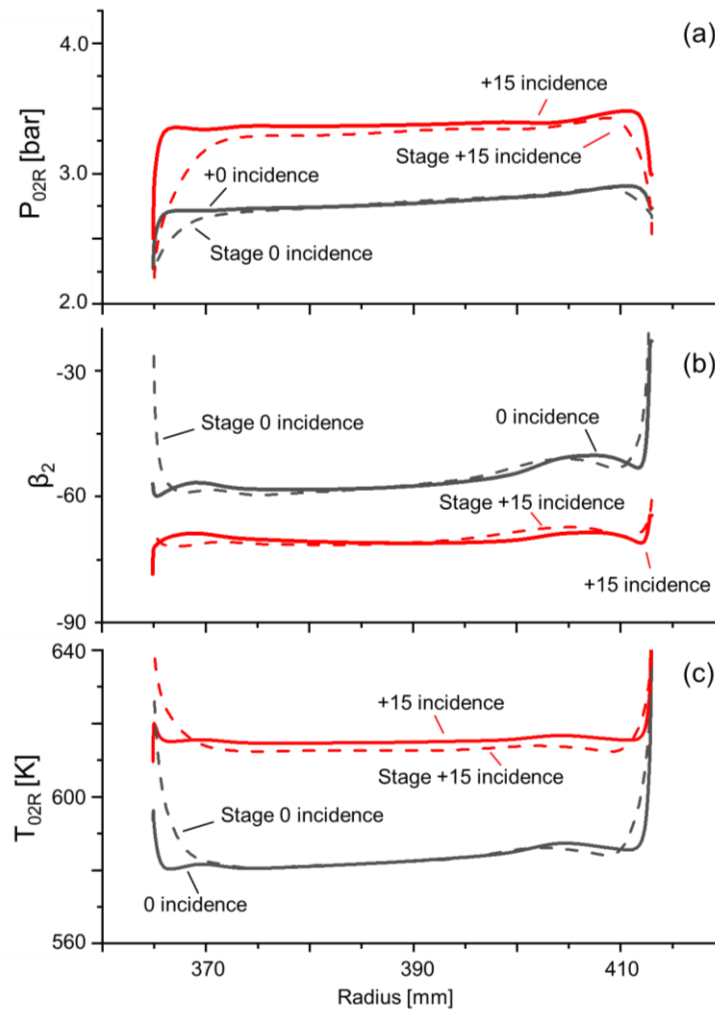


Figure 31. Boundary Conditions vs. Radius. a) Total relative pressure. b) Rotor inlet flow angle. c) Total relative temperature

4.3 Computational domain and mesh sensitivity

The computational domain displayed in Figure 32 was created using Autogrid Numeca Inc. The blade was meshed with an O4H topology. Periodicity was applied to the lateral walls. The inlet boundary was placed upstream at $0.5c_{ax}$, the outlet was spaced $2.5c_{ax}$ downstream of the blade. Periodicity was applied to the side walls. The first cell height was set to $1E-7$ leading to $y^+ < 0.5$. The domain's walls, and blade were all considered adiabatic to neglect the effects of entropy production by heat transfer between the wall and fluid.

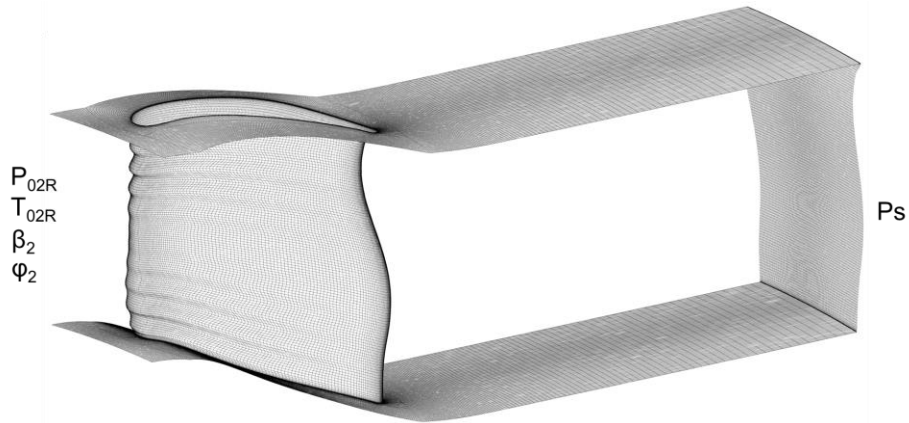


Figure 32. Wavy computational domain

Four different meshes were compared to select the optimal number of cells for the optimization. The meshes were evaluated at $+15$ degrees incidence which represents the worst pressure loss case. Table 9 shows the number of cells used to define each of the meshes. Figure 33 compares the pressure loss, as a function of mesh size. Figure 33-a investigates the effect of mesh size on total-total efficiency. Figure 33-b compares the mesh size to pressure loss. The fine mesh was able to predict the trend in pressure loss compared to the finest grid. The relative difference is less than 0.16% in pressure loss. The difference in pressure loss between cases that will be investigated later were larger than 1.3%.

Table 9. Mesh size and corresponding pressure loss

	Mesh Size	P_{loss}	ΔP_{0loss}	% Error
Coarser	2.6M	0.237	1.00E-3	0.46
Coarse	3.6M	0.238	1.98E-3	0.84
Fine	4.7M	0.235	-3.80E-4	0.16
Finest	6.7M	0.236	-	-

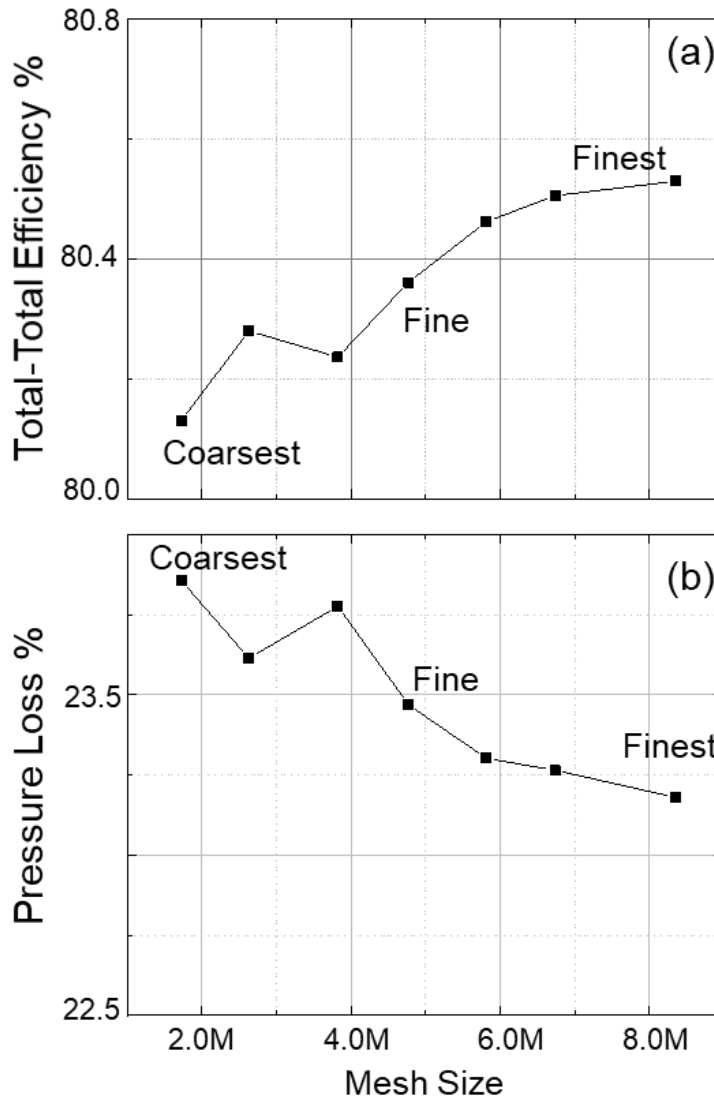


Figure 33. Mesh Sensitivity +20 deg incidence, a) Pressure loss b) Efficiency

4.4 Scaling Matrix Definition

The wavy blade was designed by scaling the leading and trailing edges and suction and pressure sides using 4 wave functions (Figure 34) scaling was performed for each profile and along the span. The wave can be any mathematical function that is defined from 0 to 1. The function was then interpolated on to the span-wise profiles.

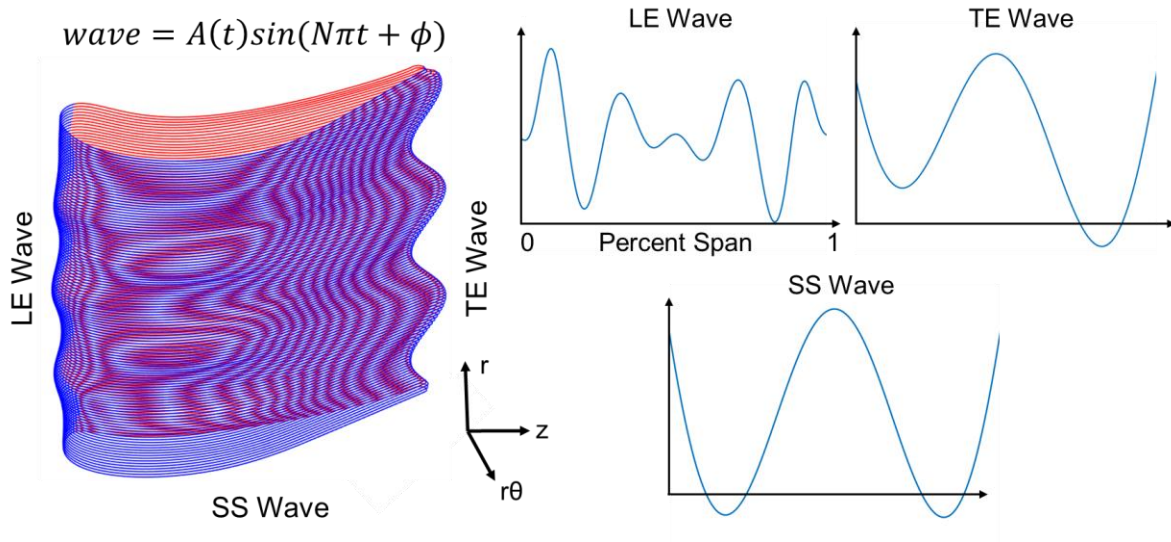


Figure 34. Left: Wave Rotation. Right: LE, TE, SS, Waves

The 3D blade's points were defined as 3 matrixes of z , $r\theta$, and r for both suction and pressure sides. 1D waves were then converted to a scaling matrix through an interpolation from leading edge to trailing edge for each profile. Figure 35 shows the wave amplitude on the suction side and pressure side. The amplitude was calculated by taking the magnitude of the stretching in z and $r\theta$ for each spanwise profile.

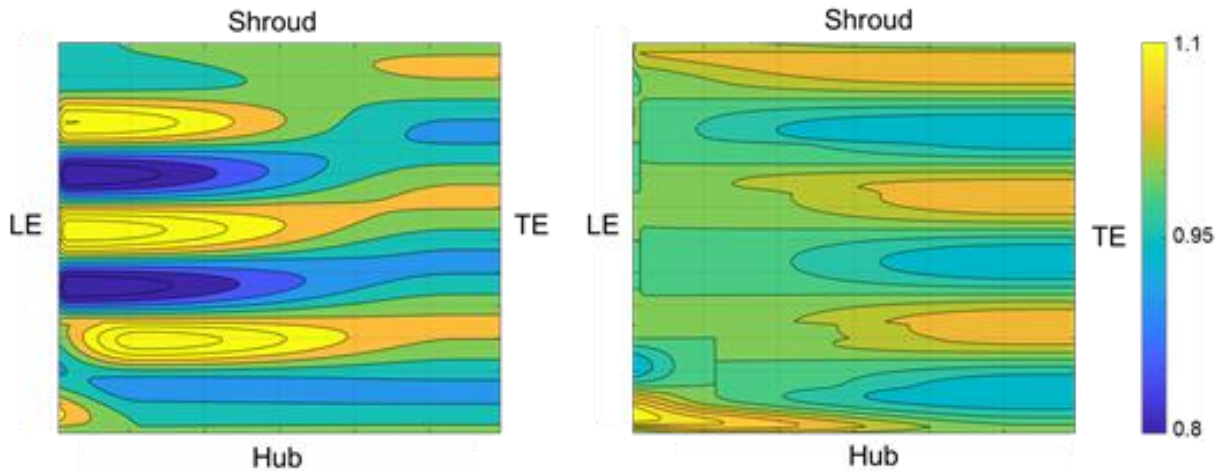


Figure 35. Wave amplitude along the blade surface Left: Suction side. Right: Pressure Side

Once the scaling matrix was defined, each profile can then be stretched and scaled by taking the difference between each point and the centroid (Figure 36-red square). The red square has to be located where $d(r\theta)/dz$ changes signs otherwise the waves would not follow the direction of the leading or trailing edge metal angles.

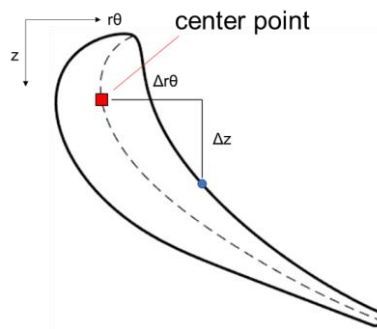


Figure 36. Location of the center point

4.5 Wavy parameterization

Each wave function was expressed as a sinusoid (Equation 22). The amplitude was defined as a Bezier curve of 3 points. Figure 37a shows a Bezier curve of the amplitude and the control points. The first and last point are free to move vertically increasing the amplitude at the hub and tip. The middle point has 2 degrees of freedom and was constrained between the two end points. This enables the amplitude to be adjusted at any percent span.

$$wave = A(t) * span * \sin(N\pi t + \phi) \quad (22)$$

Each wave was defined using 8 parameters. Four parameters are used to control the amplitude of the wave, two parameters are reserved for the frequency and phase. The last two parameters define when the waves start and end. The pressure side wave was automatically defined by the leading and trailing edge waves and blended with baseline from 10% to 90% chord (Figure 37-b). A total of 24 parameters was used to define the 3D wavy blade.

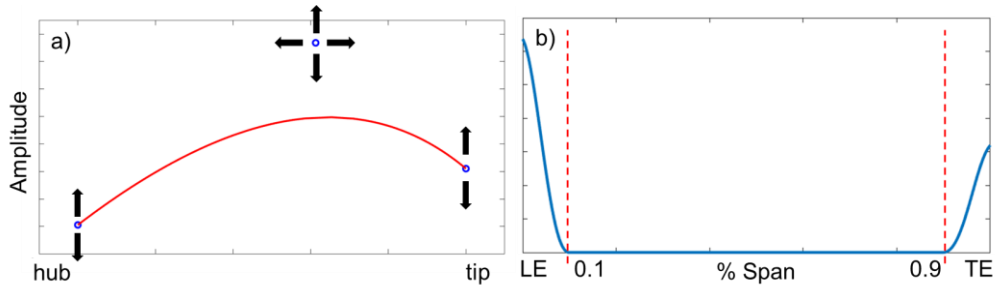


Figure 37. Wave amplitude definition. Amplitude as a function of % span.

4.6 Optimization Setup

The optimization tool used for this study is CADO [60]. CADO was configured use single-objective differential evolution [88]. The following was constrained in the optimization: the inlet flow angle and outlet flow angle to be within ± 0.2 degrees from the baseline geometry. The stage loading was constrained to be within ± 0.01 . The trailing edge radius was maintained throughout the optimization to neglect the loss improvements by stretching the trailing edge of the baseline rotor.

The optimization was initiated with a seed population of 128 individuals generated using fractional factorial approach were used to define the initial population. Crossover and mutation were applied to generate the successive populations until an optimal was reached. Each population contained 50 individuals. The differential evolution parameters are shown in Table 1.

4.7 Results

4.7.1 Optimization Results

The optimization yielded 235 individuals. The following design (Figure 38) was selected as the optimum. It matches the massflow, stage loading, and exit flow angle within 0.5 degrees of the baseline geometry at design and off-design conditions. Due to the addition of the waves, pressure loss is reduced at off-design conditions by 1.4%, the total-total efficiency increased by 0.7%.

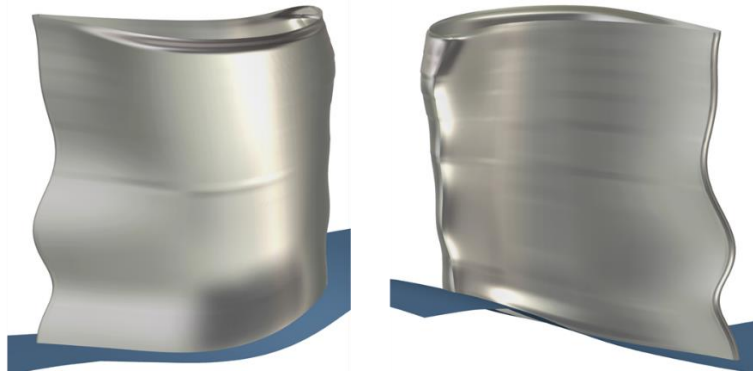


Figure 38. Optimized wavy design

Figure 39 shows the individual waves that were applied to the leading edge, suction side, pressure side, and trailing edge as a percent of the span. The trailing edge was scaled in a way that did not change the trailing edge diameter. The bottom right of Figure 39 displays 3 cut planes near the leading edge at 70%, 80%, and 90% span corresponding to the valley, hill, and valley.

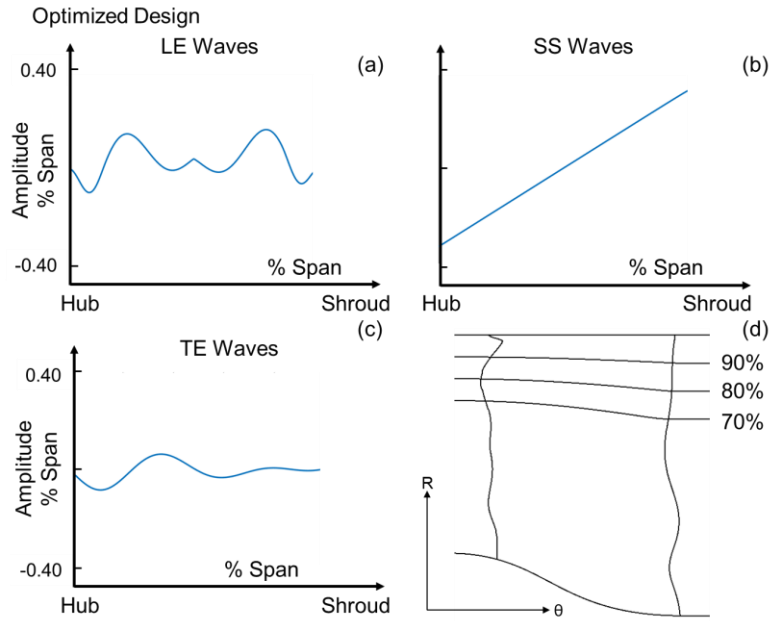


Figure 39. Optimized design wave definition as a function of span. a) Leading edge wave. b) Suction side wave. c) Trailing edge wave. d) Location of cut planes near the tip

4.7.2 Pressure loss and separation bubble

Figure 40 compares the ratio of total pressure at the exit to the total pressure at the inlet at off-design conditions. The optimized design experiences less total pressure loss near the tip and mid span, however the waves at the leading edge create more losses near the hub.

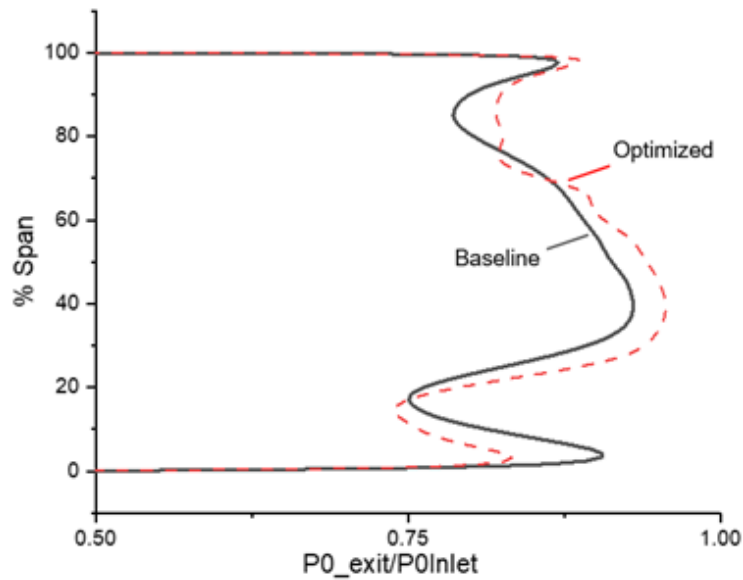


Figure 40. Ratio of total pressure at exit to inlet

At positive incidences, flow impinges on the pressure side of the blade, this causes a large separation bubble to occur on the suction side shown in Figure 41. The top plot shows the baseline blade and the separation that occurs on the pressure side. The bottom of the figure is the wavy design. Waves on the leading edge can help reduce the loss by dividing the streamlines which accelerate the flow around the wave which increases the mixing in the recirculation region (Figure 42). Low momentum flow is mixed with the main flow as it leaves the blade resulting in more uniform total pressure variation at the exit.

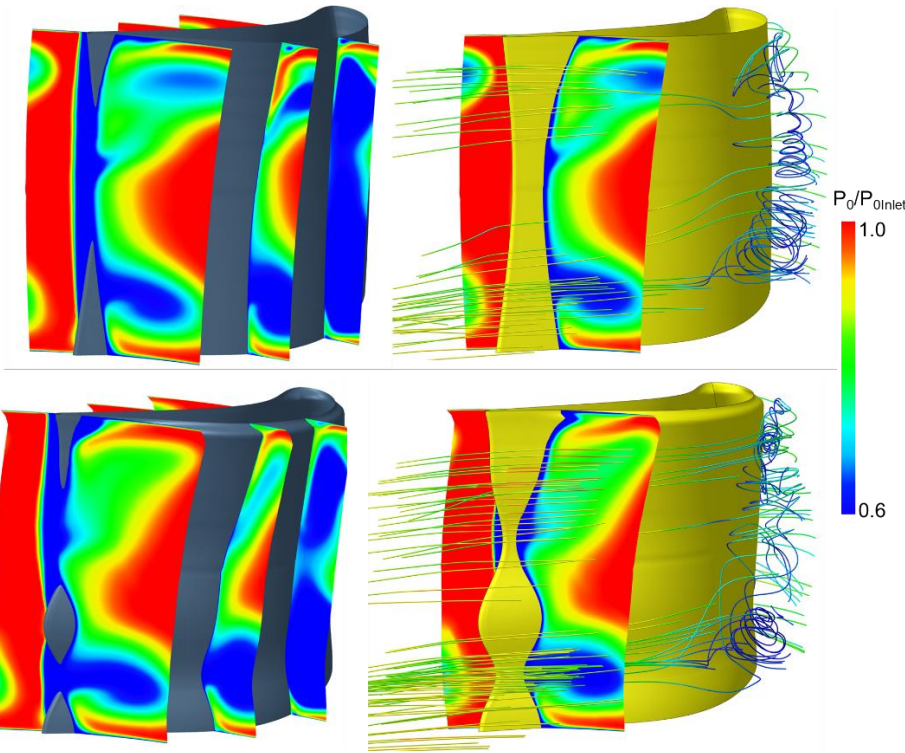


Figure 41. Large recirculation region around the suction side. Top: baseline blade: Bottom: Optimized Wavy design

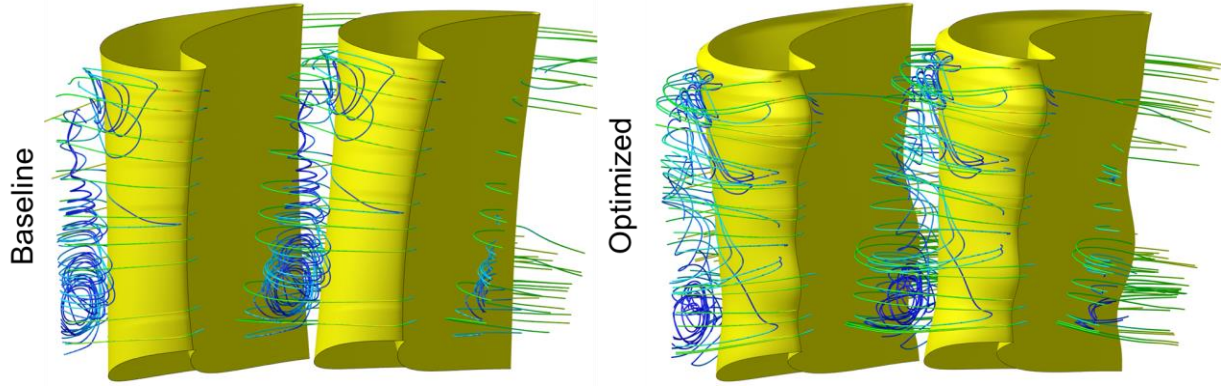


Figure 42. Streamlines comparison. Top: baseline. Bottom: Optimized

Q-criterion is used to identify vortices when $Q > 0$. Q is the summation of the strain rate tensor “ S ” with the rotation rate tensor “ Ω ”. When the rotation rate tensor exceeds the strain rate, it indicates the presence of a vortex [89,90].

$$S = \frac{1}{2} \left(\frac{\partial u_i}{\partial x_j} + \frac{\partial u_j}{\partial x_i} \right) \quad (23)$$

$$\Omega = \frac{1}{2} \left(\frac{\partial u_i}{\partial x_j} - \frac{\partial u_j}{\partial x_i} \right) \quad (24)$$

$$Q = \frac{1}{2} (|\bar{\Omega}|^2 - |\bar{S}|^2) \quad (25)$$

Figure 43 compares the Q-criterion for 3 different z planes on the suction side. The separation bubble can be clearly seen for both blades near the leading edge. As the cut planes move closer to the trailing edge, the separation bubble splits into two vortices for the baseline design near the shroud; on the other hand, the optimized geometry was able to minimize the vortex size near the tip; however, near the hub, the optimized design has a larger horseshoe vortex than the baseline.

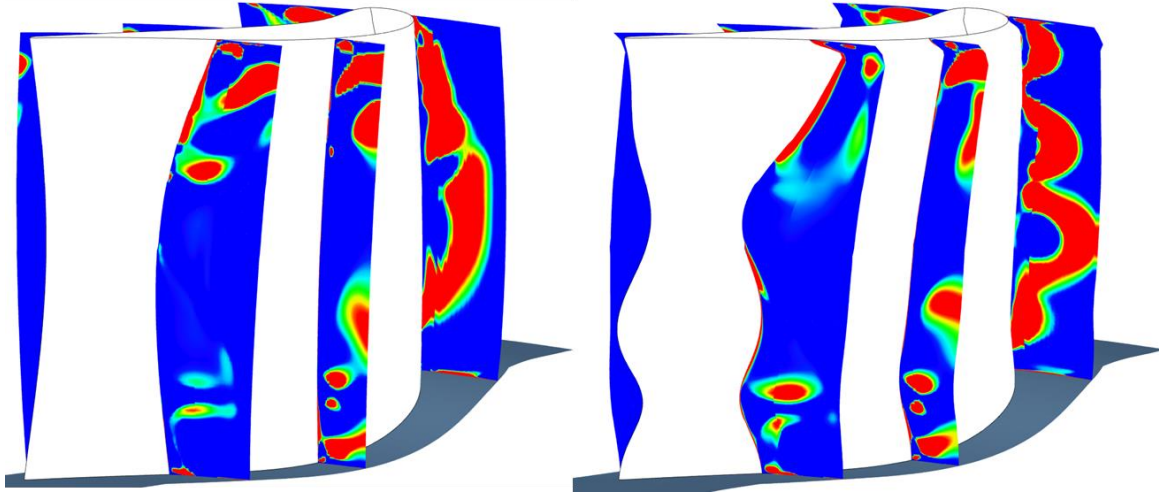


Figure 43. Q-criterion. Left: Baseline blade. Right: Wavy Blade

4.7.3 Impact on Mach Number

The peak of the wave near the tip splits the flow into the troughs as the flow moves around the suction side. This has a significant impact on the Mach number. The left column in Figure 44 shows the baseline blade at 70%, 80%, and 90% span. The optimized design shows a size reduction in the recirculation region at 70% and 90% spans which results in higher exit Mach numbers.

High Mach numbers can also be seen in Figure 45. Iso-surfaces of Mach 1.4 and 1.35 are highlighted using green and teal. The optimized design features higher exit Mach numbers at the midspan and near the tip. The baseline only has high exit mach numbers near the midspan.

Figure 46 plots the density gradient for both the blades at the same 70, 80, and 90% spans. Higher Mach numbers result in oblique shocks on the suction side. The baseline does not have a shock forming at 70-90% spans. Instead the flow that moves around the recirculation bubble interacts more with the trailing edge shock (Figure 18: 80 and 90% spans) compared to the optimized design where flow is more attached to the suction side.

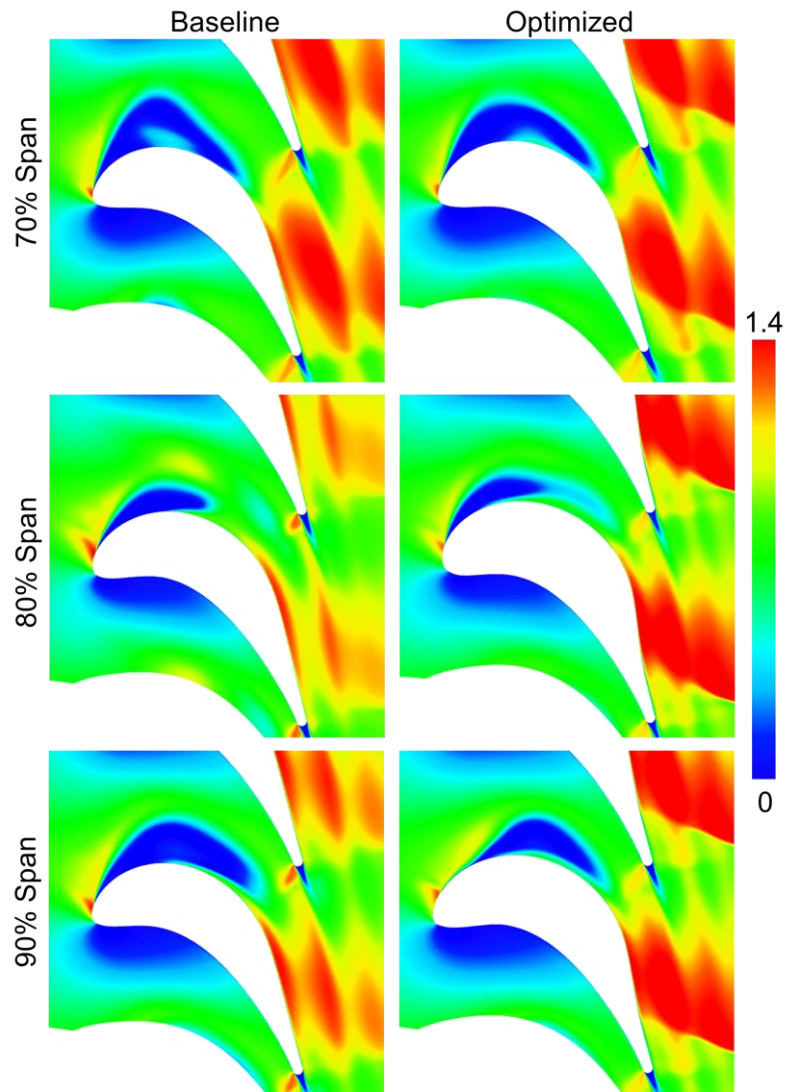


Figure 44. Mach Number contours near the shroud

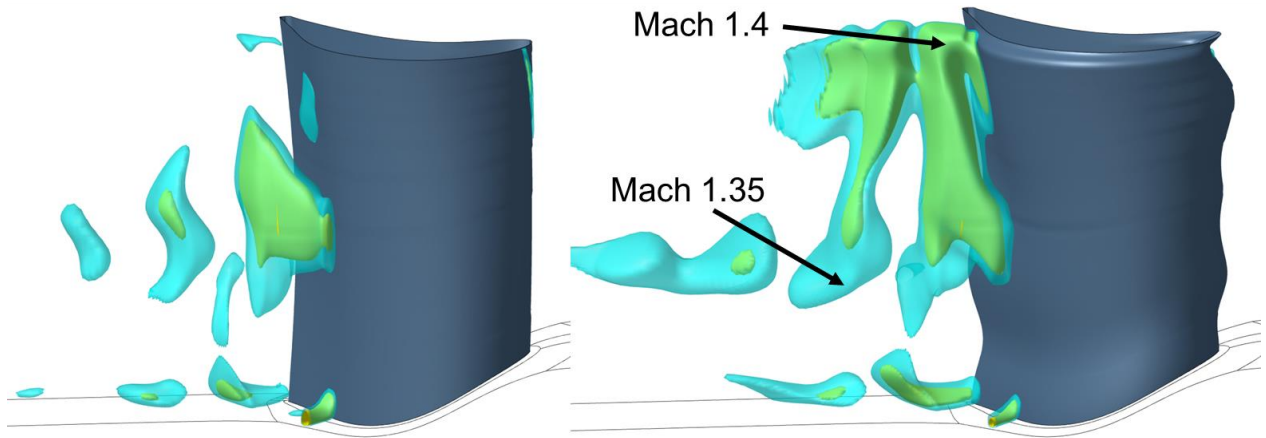


Figure 45. Iso-surface of constant Mach number. Left: Baseline. Right: Optimized.

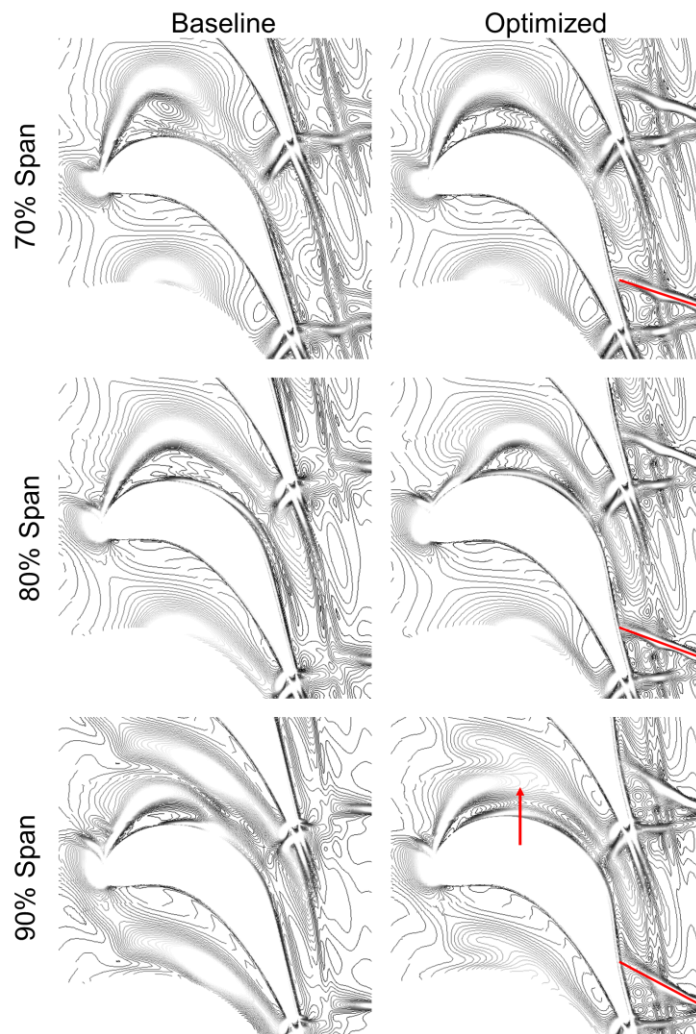


Figure 46. Density Gradient. Top: 70% span. Mid: 80% span, Bottom: 90% span.

Figure 47 compares the mach number contours with the density gradient at the leading edge. The leading edge wave amplitude at 50% span is at a smaller wave amplitude than at the near shroud (Figure 39a). This wave splits the recirculation region into 2 zones (Figure 47- Bottom right) which were identified using the vorticity. Figure 48 relates the x and y vorticities for the baseline and optimized. The lines represent constant density gradients. The optimized geometry (Figure 20) shows x and y vortices of opposite signs (Figure 48-Top right, Bottom right) which could be a result of slice through a 3D flow feature.

Figure 49 is the 3D plot of iso-surfaces of vorticity. The top two figures represent x-vorticity and the bottom two represent y-vorticity. The leading edge waves generate vortex structures in the in the x direction of opposite signs. The two vortices that the slice in Figure 47 passes through are identified as “A” and “B” in Figure 49-Top right.

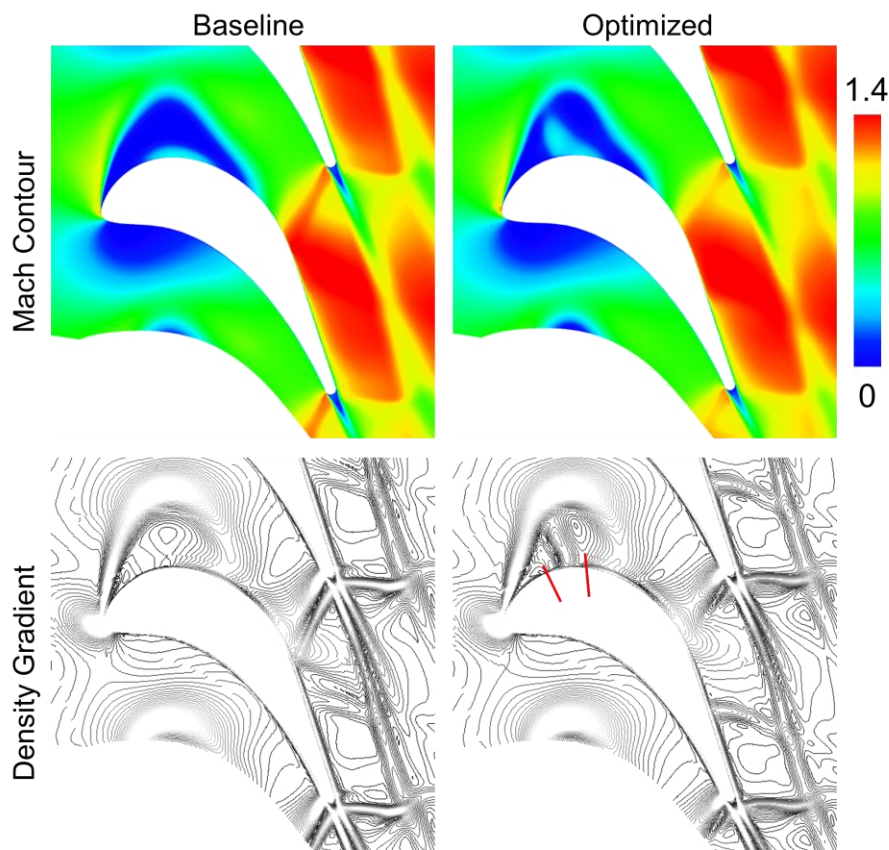


Figure 47. Mach contour and density gradients at 50%. Left column: Baseline. Right column: Optimized. Top row: Mach contours. Bottom Row: Density gradients magnitude.

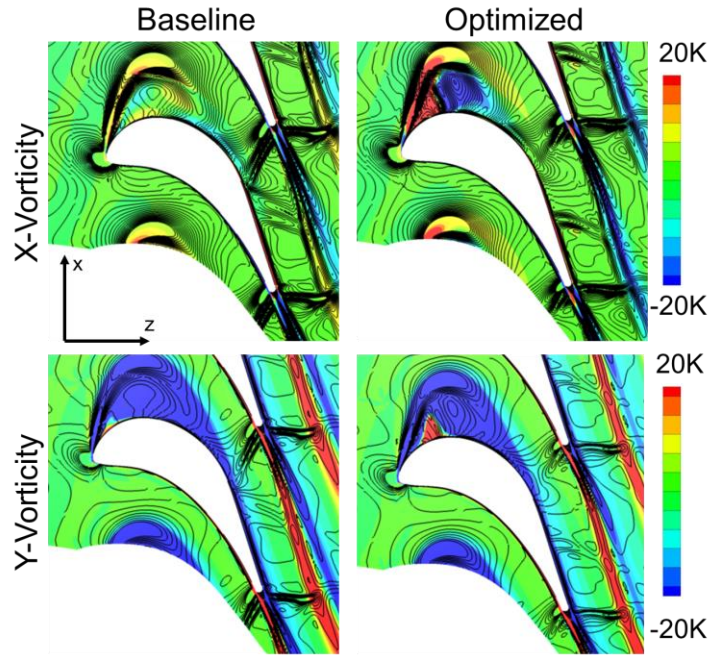


Figure 48. Vorticity at 50% span. Top Row: X-Vorticity. Bottom Row: Y Vorticity. Left Column: Baseline. Right Column: Optimized.

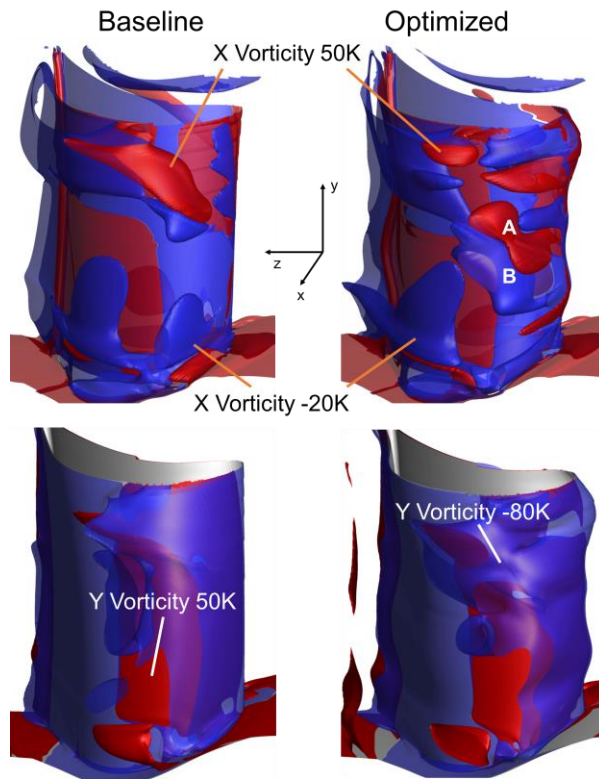


Figure 49. Vortex Structures. Left column: Baseline. Right column: Optimized.

The trailing edge wake at 3 different cut planes, 40%, 50%, and 60% are shown in Figure 50. At 60% span, the optimized geometry does not show separation while in the baseline there is separation occurring near the trailing edge. Additionally, at 40 and 50% spans the optimized geometry has a smaller wake profile than the baseline.

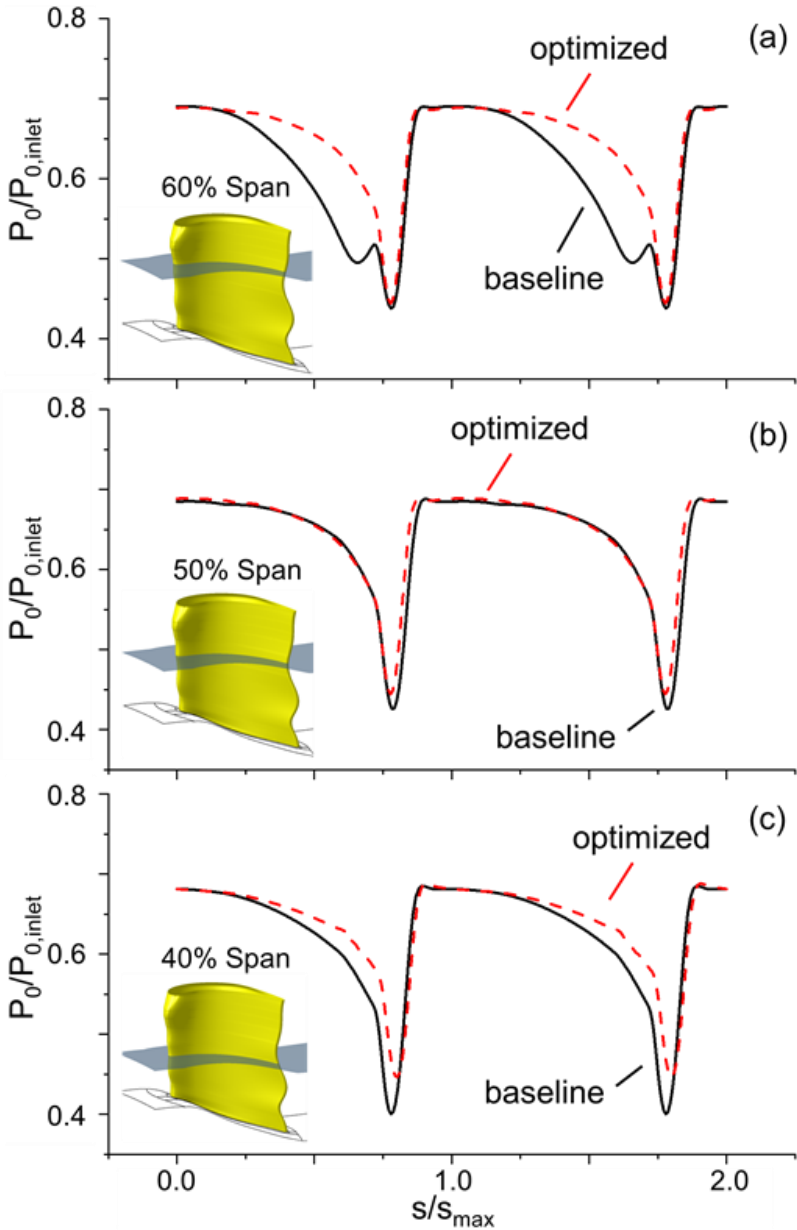


Figure 50. Trailing edge wake profile

4.7.4 Secondary Flow

Iso-surfaces of Total relative temperature (T_{OR}) is used to identify the secondary flow shown in Figure 51. On suction side, the passage vortex is greatly reduced at midspan and near the hub and above the midspan.

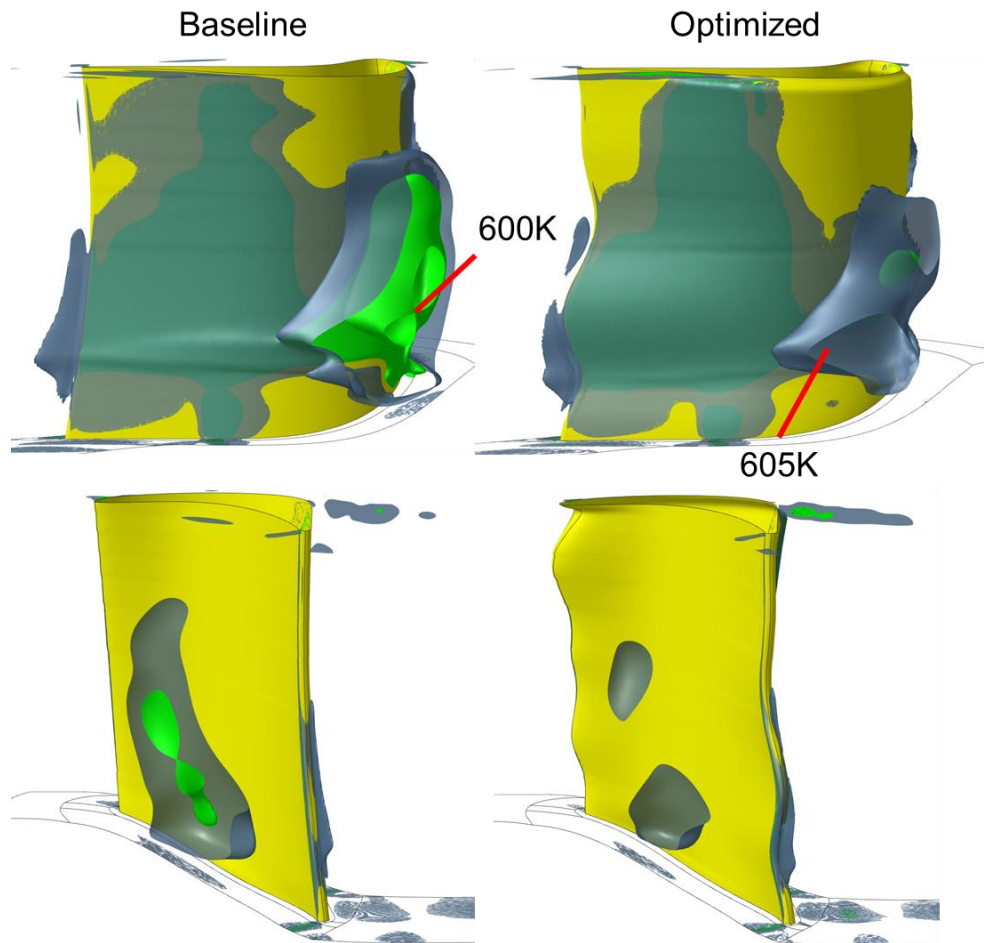


Figure 51. Secondary Flow. Left: Baseline blade. Right: Optimized.

The effect on the optimized blade on horseshoe vortex was approximated by changing the hub and shroud to be Euler walls. The percentage reduction in losses is summarized in Table 10. The wavy design is able to reduce secondary flow losses; however, the contribution of the horseshoe is small compared to the overall loss of the blade.

Table 10. Endwall secondary flow loss contribution

	Horseshoe vortex contribution	Secondary flow loss reduction	Reduction in profile and mixing loss
Baseline	14.8 %	-	-
Optimized	12.9 %	-20%	-7.4%

4.7.5 Blade Loading

Figure 52 compares the blade loading and C_p distribution at 3 different spanwise locations. The top row shows the isentropic mach number for the 3 different spans: 40% span which is below the hill at the leading edge, 50% at the peak of the hill, and 60% at the valley above the hill. The bottom row compares the pressure coefficient for the different spans. Areas where C_p (Equation 26) has a positive slope indicates regions of separation.

$$C_p = \frac{P_{local} - P_3}{P_{02R} - P_3} \quad (26)$$

Both blades experience high mach numbers along the suction side followed by separation. At 40% span, the optimized design was able to reattach the flow earlier than the baseline geometry. The opposite happens at 50% and 60% span; the flow attaches later, but there is less diffusion from 40-60% of axial chord. And in all cases, the blade is more loaded at the trailing edge. Positive incidence increases the front loading of the airfoil; the waves shift the loading to the trailing edge.

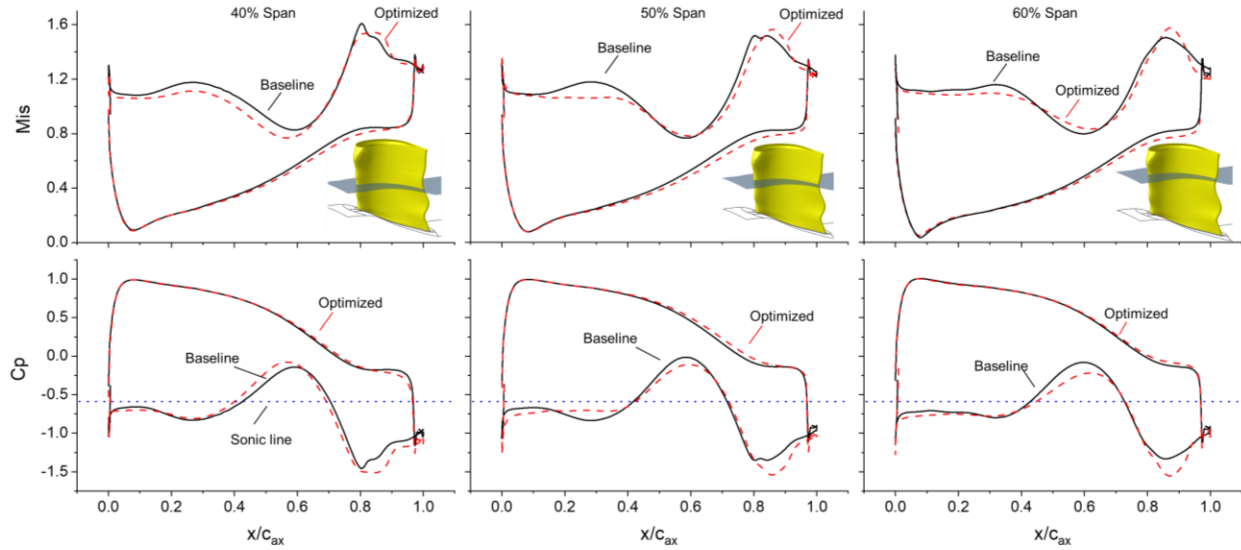


Figure 52. Top row: isentropic mach number for 3 different spanwise locations. Bottom row: Cp distribution for 3 different spanwise locations. Dotted blue line indicates the sonic line

4.7.6 Stage Performance

Both the optimized and baseline rotors were simulated using the computational domain (Figure 55) over a range of incidence angles by changing the RPM. Figure 53 compares the pressure loss and total-total efficiency with incidence and RPM. The optimized design is able improve the efficiency by 0.7% and the pressure loss is reduced by 1.4% at 15 degrees positive incidence. As the RPM increases, the benefit of the wavy design is smaller. Both blades perform similarly at design conditions, the baseline is better by 0.2% in total-total efficiency, 0.6% in pressure loss. At negative incidence the optimized performs worse than the baseline by 0.2% in efficiency. The stage loading is the same for both blades, 5.92 at +15 positive incidence and 1.34 at -31 incidence.

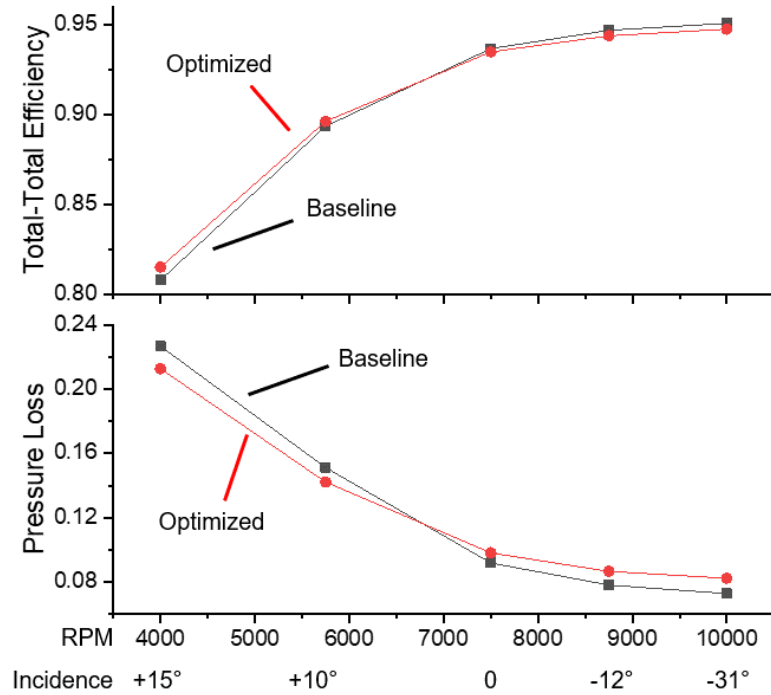


Figure 53. Top: Total-Total efficiency. Bottom: Pressure loss

In addition to the rotor only simulations, the optimized rotor and the baseline were both simulated with a stator in front. The computational domain used is shown in Figure 54. The stator is located 1 axial chord upstream of the mixing plane. The rotor is positioned $\frac{1}{2}$ rotor axial chord downstream. The rotor mesh remained the same, the stator mesh comes from [91]. The simulation was run at two different incidence angles 0 and +15. The absolute Mach number exiting the stator is around 1.02.

A comparison of the boundary conditions at the rotor inlet is show in Figure 55. The solid lines represent the rotor-only boundary conditions, the dashed lines are from the stage after the mixing plane. The comparison fits well at the midspan. The main differences occur near the endwalls; this is due to a thicker boundary layer forming at the stator exit.

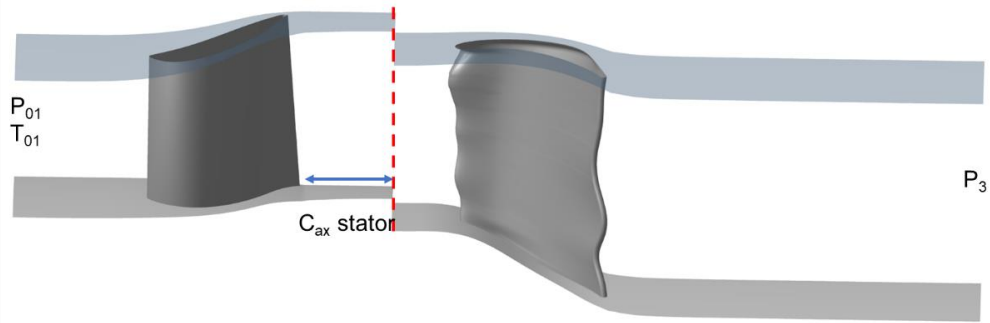


Figure 54 Stage computational domain

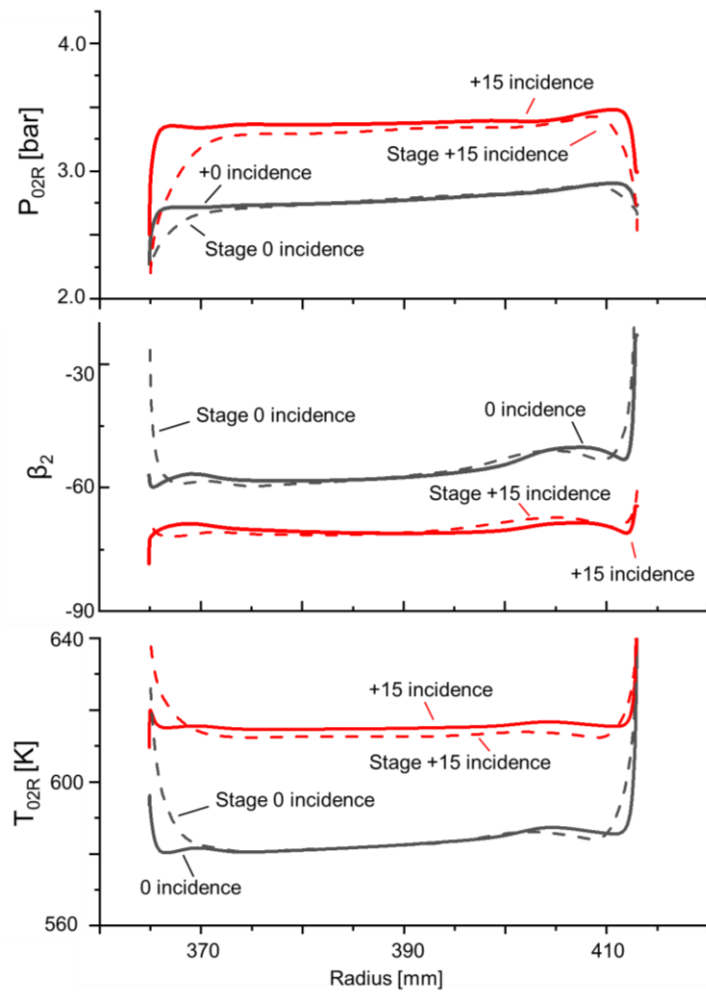


Figure 55. Boundary conditions of stage and rotor only simulations

At design conditions (Table 11) the optimized design has lower efficiency than the baseline. However, at off-design conditions the optimized design performs more 1.2% efficiency points better than the baseline.

Table 11. Stage baseline and wavy simulations at design conditions

	η_{TT}	P_{loss}	β_2	β_3
Baseline	91.3%	14.2%	-55.4	69.2
Optimized	90.8%	16.0%	-54.5	69.2

Table 12. Stage baseline and wavy simulations at +15 incidence

	η_{TT}	P_{loss}	β_2	β_3
Baseline	77.2%	11.1%	-69.9	68.0
Optimized	78.6%	10.6%	-69.9	67.4

5. OPTIMIZATION OF THE CAVITY

5.1 Design Optimization Approach

The design of the cavity is simplified into a 2D axi-symmetric simulation of the cavity without the stator or rotor. There is a pitchwise static pressure variation from the upstream vane that is neglected. The variation in static pressure causes ingestion and ejection zones along the rim seal [27]. By not including the pitchwise variation, this analysis focuses on the impact of the cavity for a given inlet swirl. Other authors [92–97] have also chosen similar approaches in order to delineate the physics of the cavity. The turbine platform geometry used for the optimization is the highest efficiency design, obtained with an in-house turbine design toolbox [91] at engine scaled conditions. Table 13 highlights the boundary conditions of the 2D cavity. This simplified analysis does not include stator or rotor geometries. The rotor platform is considered in the relative frame of reference and no rotation is applied to the stator platform. The baseline purge geometry is the double-overlap seal and the static pressure at the outlet was selected to match the relative mach number (M_{2r}) at the exit of the stator before the purge. The total pressure in cavity was chosen to give cavity to mainstream massflow ratio of 1.4%.

Table 13. Boundary Conditions

T_{02R} [K]	P_{02R} [bar]	T_{02R}/T_{0C}	T_{02R}/T_{wall}	P_{02R}/P_{s3}	RPM
1700	30	2	1.5	1.04	-

5.1.1 Optimization Strategy

The design methodology (Figure 56-Bottom) uses a differential evolution multi-objective optimizer, CADO [60], to execute an evaluation routine that uses MATLAB to generate the cavity geometry which is parameterized using a meander line and two sets of thickness distribution. The routine exports the geometry to an unstructured mesher, HEXPRESS. The mesh is solved in FLUENT using unsteady Reynolds averaged Navier Stokes (URANS). The URANS result files was exported for the last 1000 timesteps, corresponding to 6 to 7 periods of data. For each timestep, inlet massflow, outlet massflow, cavity massflow, massflow weighted averaged fluid temperature above the platform, flow velocities and density at exit of the purge are extracted and averaged. Fluid temperature above the platform and the cavity massflow were

passed into the optimizer as objectives to be minimized. A population size of 30 individuals was chosen with 60 individuals in the restart file. Each “individual” comprises of a vector of parameters used to define a purge design. Individuals are paired using crossover and mutation to generate the new population of designs. The Design of Experiments (DOE) had a population of 128 individuals which is within the range of 5 to 10 times the number of parameters [98]. The population size was chosen as a balance between speed, evaluation time, and geometric variability.

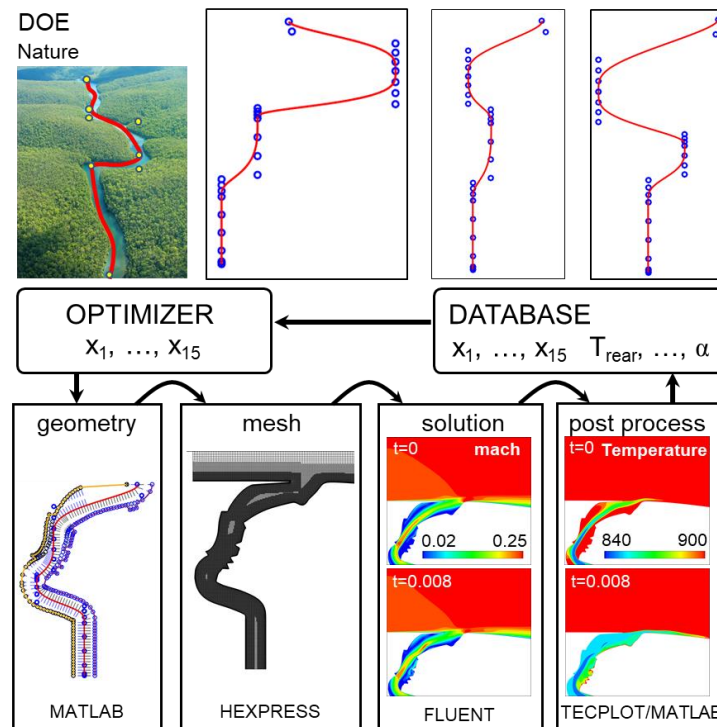


Figure 56. Hub disk design overall strategy

5.1.2 Meander-line parameterization

The purge geometry was constructed using 3 components: the meander line, the stator rim, and the rotor rim (Figure 57: Left). The meander line was assembled by joining 4 Bezier curves. In total 7 parameters were used to create 4 Bezier curves that define the meander line. Four parameters were used to construct the first Bezier curve starting at point 1 and ending at point 4. One parameter determined the exit slope of the meander, the next 2 parameters controlled the horizontal and vertical location of point 4. The last parameter was used to control the thickness “A” between points 3 and 5. The second Bezier (points 7 to 9) was parameterized the same way.

The last Bezier is from point 9 to 10. The points without fill in Figure 57-left represent intermediate points that are spaced equally between filled control points.

5.1.3 Creation of the stator and rotor rim cavity shape

Both the stator and the rotor rims were defined using splines that control the thickness perpendicular from the meander line. The thickness of each rim was assigned using 4 parameters each, represented by the first 4 points from left to right in Figure 57-mid. The first 4 points were allowed to move vertically, the last point was fixed at 1 mm. The location of the first point represents the thickness of the rim at the exit into the channel while the last point is the thickness at the cavity inlet. The applied stator and rotor rim thicknesses are shown in Figure 57-right. A filtering algorithm was used to space out points that are less than the minimum allowed spacing of 2mm [27,99] and also remove points that result in the intersection of curves. In total 15 parameters were used to define the entire cavity.

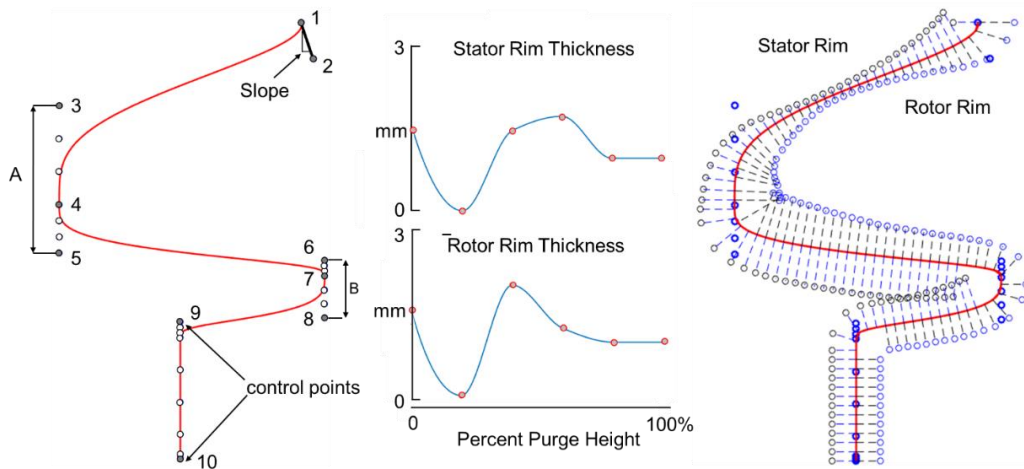


Figure 57. Left: Meander line. Middle: Stator and rotor rim thicknesses. Right: Stator rim and rotor rim shape.

An alternative strategy is to use a Bezier curve to fit the points as shown in Figure 58-a. This produces designs without the possibility of jagged edges. Both parameterization strategies were compared. To smooth the interface between the channel and the purge, a Bezier curve is used to remove sharp corners. The curve is fitted to the points of the channel and the purge (Figure 58-b).

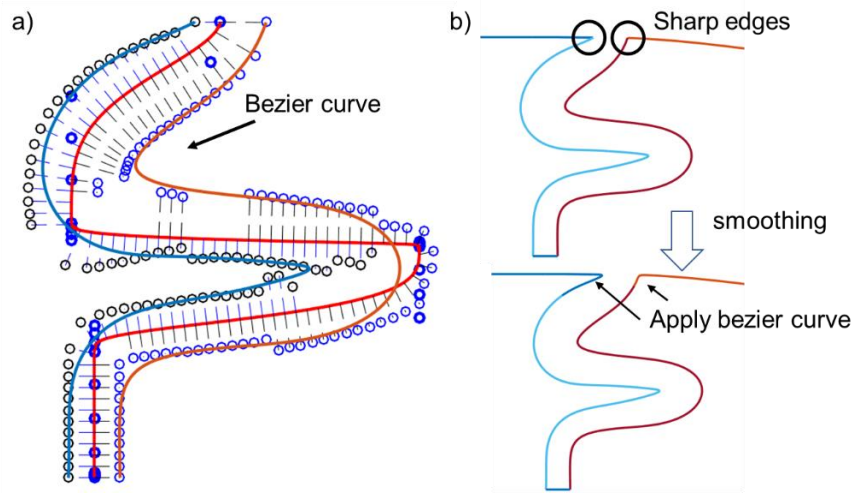


Figure 58. a) Purge smoothing using Bezier curves. b) Removal of sharp corners.

5.1.4 Computational domain

The computational domain (Figure 59) is an unstructured 3D hexahedral mesh – created in HEXPRESS – contains 2-kplanes with symmetry boundary conditions on the side walls. A y^+ of less than 0.3 was achieved by using a wall spacing of $0.1\mu\text{m}$. The mesh was exported to Fluent where it is solved in steady state (RANS) for 8000 iterations before moving to an unsteady simulation (URANS) for 7200 timesteps with $2\mu\text{s}$ per timestep. An unsteady simulation was required to resolve the vortex shedding. Time averaged quantities was obtained using TECPLOT and passed back to the optimizer.

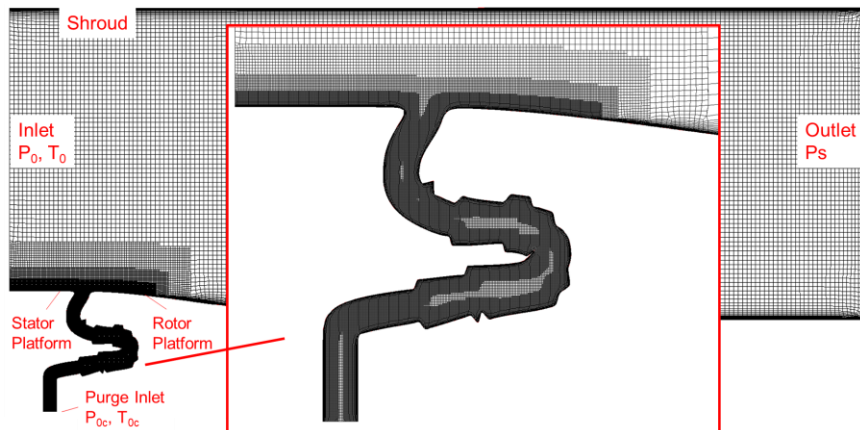


Figure 59. Computational domain mesh generated using HEXPRESS

5.1.4 Grid sensitivity and convergence analysis

A test geometry was simulated in URANS using 4 different grid levels. The massflow weighted average fluid temperature (Equations 27 and 28) above the rear platform was compared against the number of nodes used to define each grid. The locations above the platform are shown in the rectangles (Figure 60-left). The difference between the fine and finer meshes was 0.8K. The finer mesh was selected for the optimization, factoring computational resources available and evaluation time. Figure 60-right compares the fluctuation of massflow averaged rear platform temperature with the timestep. Convergence for an unsteady simulation was evaluated using the technique of Clark and Grover [100]. In this method the phase, amplitude, mean value, and the cross correlation for each cycle are cross correlated. The unsteady simulation is considered periodic when the cross-correlation coefficient is 0.96 or above. In the optimization, the minimum coefficient was 0.9561.

$$T_{rear}(t) = \frac{\sum_{i=1}^{N_{cells}} (A_{cell} \rho V_{ax} T)_i}{\sum_{i=1}^{N_{cells}} (A_{cell} \rho V_{ax})_i} \quad (27)$$

$$T_{rear} = \frac{1}{100} \sum_{t=(T_{end}-100)}^{T_{end}} T_{rear}(t) \quad (28)$$

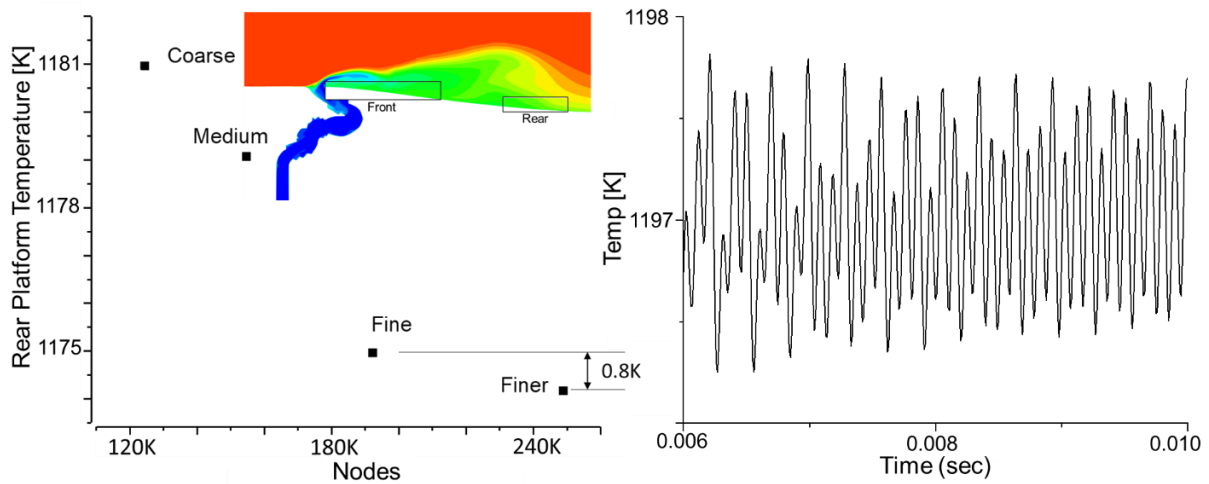


Figure 60. Cavity Mesh Sensitivity

5.2 Results of 2D Optimization

5.2.1 Geometries that reduce rear platform temperature

The results of the optimization are shown in Figure 61. The optimizer iterated through 10 populations with 30 individuals per population. Each symbol in Figure 61. represents a unique design. The vertical axis shows the rear platform temperature and the massflow ratio (Equation 29) in abscissa.

$$\text{Massflow Ratio [\%]} = 100 * \frac{\dot{m}_{\text{Purge Inlet}}}{\dot{m}_{\text{Inlet}}} \quad (29)$$

The red line represents the pareto front – an optimal trade-off between cooling of the rear platform and massflow required. The double overlap seal baseline is indicated with a diamond near the top of the graph. The straight/radial cavity is represented by a diamond near the bottom. Circular symbols are designs that have jagged geometries including A-D. Square symbols are designs that have Bezier fitted geometries including “X” and “Y”. Each symbol is labeled with a color corresponding to the level of blowing ratio (Equation 30).

$$\text{BlowingRatio} = \frac{\rho_{\text{coolant}} V_{\text{coolant}}}{\rho_{\infty} V_{\infty}} \quad (30)$$

Blowing ratio relates the momentum of the flow exiting the cavity to the main flow. Designs with higher blowing ratio are those that have high discharge coefficients. Blowing ratio ranges from 1.1 to 0.6 along the pareto front. Purge designs featuring low massflow ratios contain two overlaps regions. At the top of the pareto front, design “A” ejects flow against the mainstream, offering better cooling than the baseline double overlap seal. Moving down the pareto front, design “B” delivers a 150K difference over the baseline for a 0.5% increase in massflow. In this design, cavity flow is purged along the platform in the direction of the mainstream flow which reduces mixing with the mainflow and provides better cooling to the platform. Designs “X” and “Y” which were designed using the Bezier smoothing strategy. They allow more cooling and perform similarly to “B” and “C”. Designs that provide the best cooling to the rear are also the best at cooling the front. **The parameterization strategy can lead to designs with pointy cavity exits that are not feasible manufacturing perspective and from a stress point of view, however we want to explore the potential of these unconventional geometries to quantify aero-thermal benefits.**

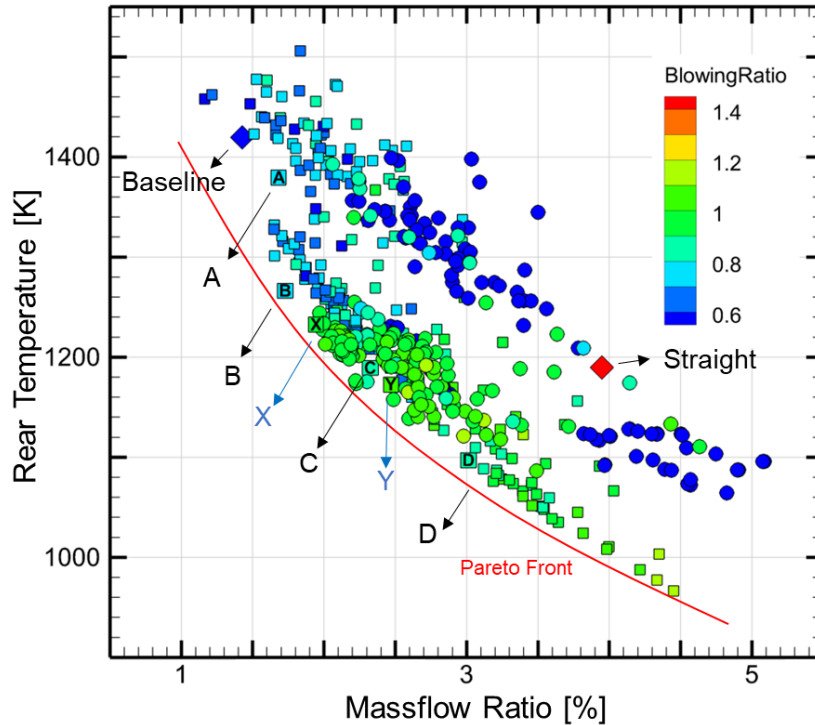


Figure 61. Rear Temperature plotted against massflow ratio

Figure 62 shows iso-TKE (turbulence kinetic energy) plotted with iso-contours of constant Q Criterion for designs “A” and “D” at two time instances. Vortices were identified using the Q criterion [89,90]. Regions of high TKE designate strong mixing between main flow and purge flow. For example, design “A” which ejects purge flow against the main flow, in so doing creates a large vortex that detaches as it travels downstream. This also generates a large fluctuation in rear platform temperature. The average cooling of “A” is better than the baseline, however it does not reduce the rear temperature as much as design “B” which has a similar massflow ratio. Geometries that eject in the direction of the channel such as “B” and “D” produces are small recirculation bubble that sheds from the inlet (Figure 62). Additionally, designs have less overlap allow more massflow, this can reduce fluctuations in rear platform temperatures.

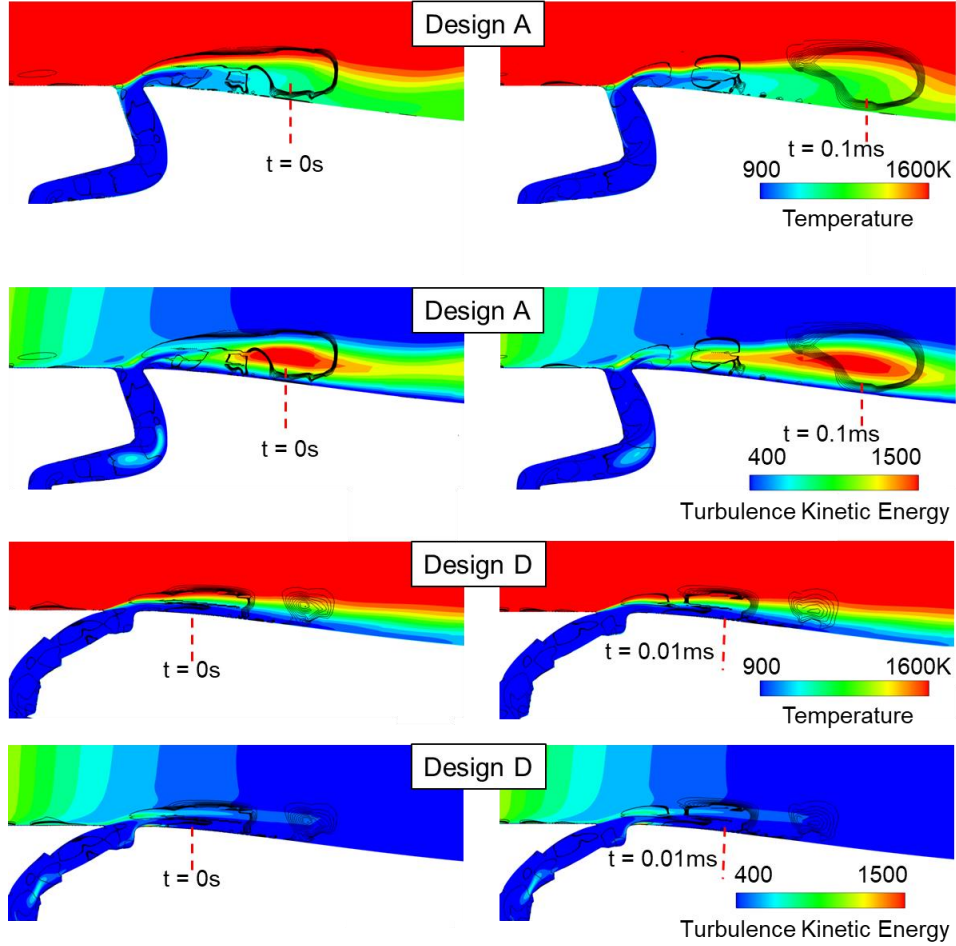


Figure 62. Top: Contours of temperature and lines of constant Q Criterion. Bottom: Contours turbulence kinetic energy with lines of constant Q Criterion

5.2.2 Blockage and Exit Flow Angle

Blockage is defined as the effect of the cavity on the stator outlet flowfield (\dot{m}_{inlet}) by comparing the current inlet massflow to the massflow without purge.

$$Blockage [\%] = 100 * \left(1 - \frac{\dot{m}_{inlet}}{\dot{m}_{inlet \text{ no purge}}} \right) \quad (31)$$

The pitch angle alpha was determined at purge exit.

$$\alpha = \tan^{-1} \frac{V_y}{V_x} \quad (32)$$

Figure 63 compares the effect of blockage and the massflow rate through the cavity. The symbols are colored corresponding to the pitch angle. Designs that have exit angles of 20-30

degrees have less blockage of the main flow; on the contrary, as purge massflow rises to 4-5%, the blockage of the mainflow increases and the purge exit flow angle increases to about 30 degrees.

The standard deviation of the purge exit angle was investigated, designs that discharge cavity flow at shallow angles of 20-30 degrees experience less fluctuation in flow angle and rear platform temperature. These types of designs also provide the best cooling of the rear platform with temperatures 1150-1350K. Rear platform temperature was further reduced at purge massflow ratios greater than 3.5% at the expensive of increasing blockage above 3%. Designs that eject cavity flow at higher angles cause higher fluctuations in temperature and blockage of the main flow.

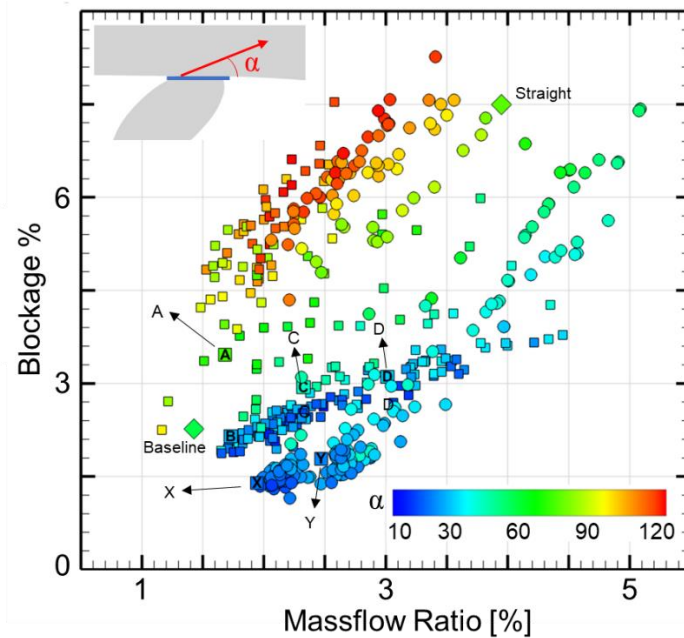


Figure 63. Blockage vs. Massflow contoured with purge exit flow angle

5.2.3 Smoothness comparison

The parameterization produced designs that are jagged which is not practical from a manufacturing perspective. To analyze the effects of jagged vs. smooth. A jagged design, B, was smoothed using running averages. In the investigated cases (Figure 64), the smoothed geometry resulted in a higher outlet velocity, and therefore higher Reynolds numbers. Thus, smoothness increases the heat transfer between cool purge flow and the hot walls within the cavity. The effect becomes more pronounced towards exit. This impacts the cooling of the platform.

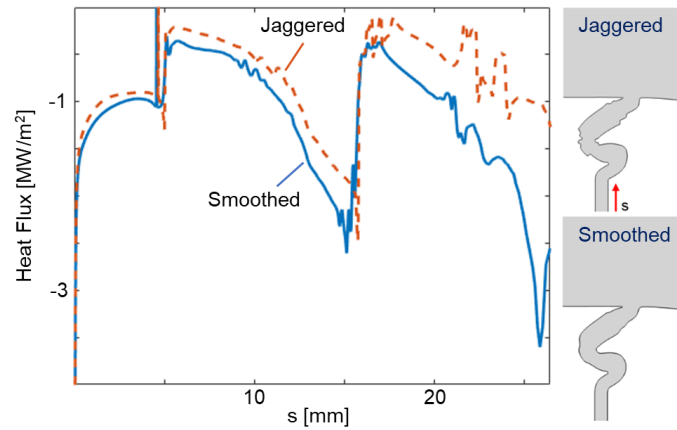


Figure 64. Left: Heat flux within the cavity comparison with smooth geometry. Right Top: Design B jagged. Right Bottom: Design B Smooth

5.2.4 2D/3D Stationary and Rotation comparison

The hypothesis that the cavity can be designed using a 2D axi-symmetric approach was tested against 3D in stationary and rotation. The 3D computational domain was created using Autodesk Inventor by taking design “B” and rotating it 6 degrees about the axial direction shown in Figure 65. The mesh contains 9M tetrahedron cells and maintains the same level of Y^+ as the 2D mesh. A periodic boundary condition was applied to the side walls to take into account tangential flows. The mesh was solved in Fluent using Reynolds Averaged Navier Stokes using the same boundary conditions as the 2D simulations. To simulate rotation, a rotational speed of 7500 RPM was employed on the stator side platform.

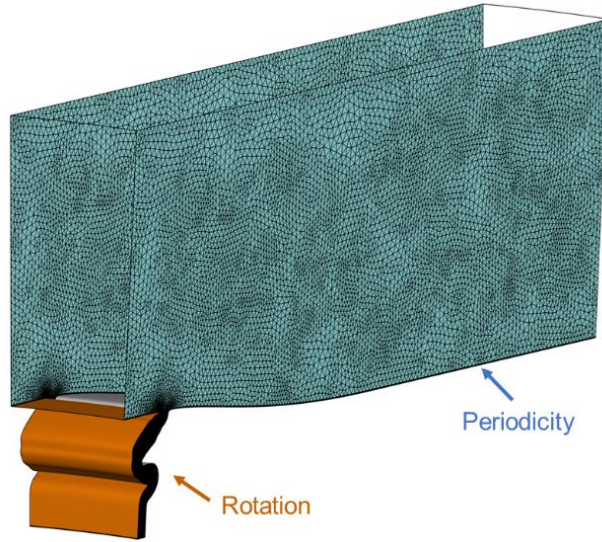


Figure 65. Computational Domain

Table 14. 2D/3D cavity simulation boundary conditions

	P_{01} [bar]	T_{01} [K]	Re_u	RPM	P_{s3} [bar]	T_{wall1} [K]	T_{wall2} [K]
2D/3D Stationary	30	1700		-	28.9	1133	1300
3D Rotation	30	1700	2.9E7	7000	28.9	1133	1300

Table 15. 2D/3D cavity inlet total conditions

	P_{0c} [bar]	T_{0c} [K]
2D/3D/Rotation	29.9	850

Figure 66 compares the heat flux inside the purge (Top) and on the bottom, the distribution of heat flux across the platform for the 2D, 3D rotation (orange circles), and 3D stationary (red triangles). The data was sampled by performing radial pitchwise averages. Inside the cavity the trend is similar for all 3 cases. However, there are slight deviations from where the flow is forced to turn; the mean level of deviation from 2D with 3D rotation is 16%. Figure 66-bottom compares the heat flux at different axial locations across the rotor platform. The trend in heat flux in the 2D simulation inside the cavity and on the platform corroborate the 3D results. Rotation has less of an impact on the heat flux within the cavity than the massflow.

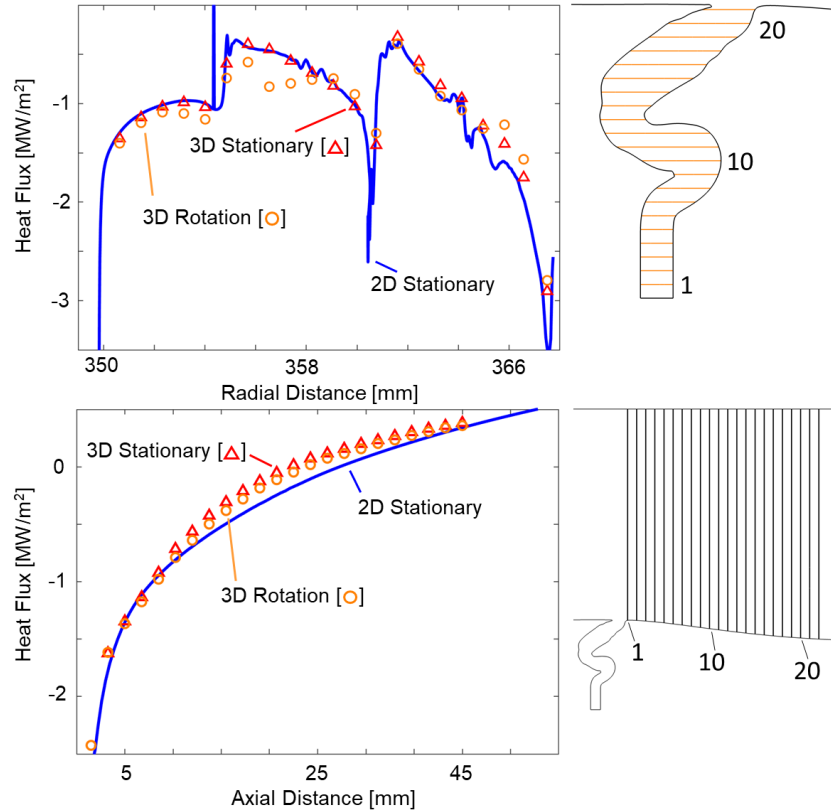


Figure 66. Top: Heat Flux [W/m^2] inside the cavity. Bottom: Heat flux along the rotor platform vs axial direction

5.2.5 Gap Sensitivity

In spite of potential benefits of jagged designs, smoother Bezier curve fitted designs are more feasible to implement. Hence, a robustness analysis was performed on the sensitivity of three different Bezier smoothed designs, X and Y, these designs are compared with the straight cavity with variations in gap sizes. Figure 67 compares the heat flux with the massflow ratio for the 3 designs and 3 gap sizes, -10%, 0%, and +10%. Time-averaged heat flux averaged within a 2cm region downstream of the rotor purge shown in the rectangle was used as a comparison benchmark.

An increase in heat flux can be seen for design “Y” and straight purge when gap is increased. Design “X” with its larger meander, is more resilient to changes in gap. Increasing the gap by 10% results in a 1% change in massflow rate. The heat flux remains constant from nominal to 10% gap. The straight purge is more sensitive in terms of massflow. When gap size increased by

10%, the massflow increased by 9% providing an improvement of 6% in cooling the rear platform.

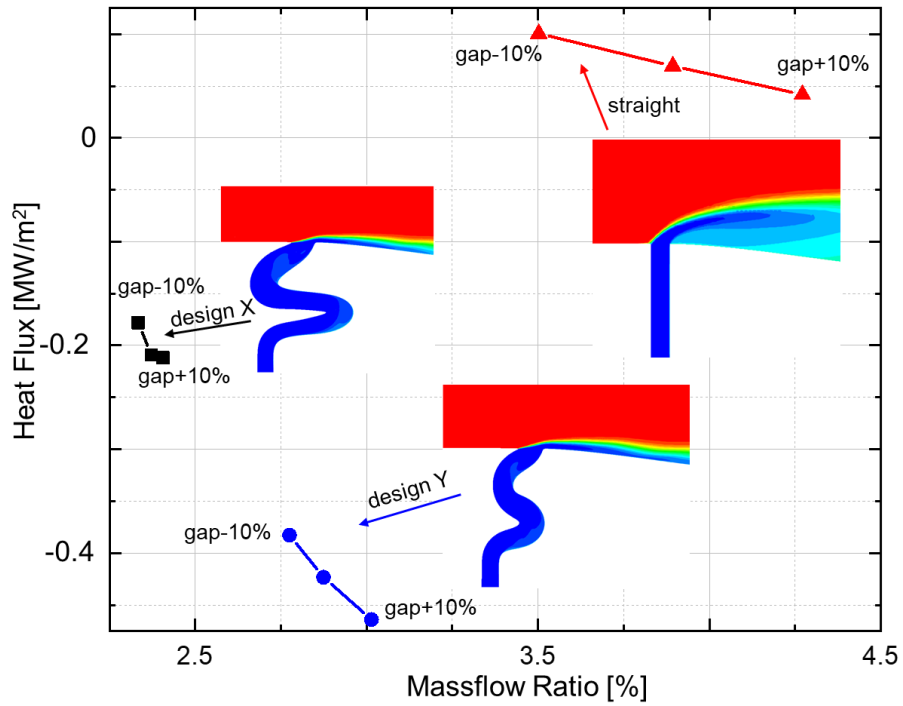


Figure 67. Heat flux vs. massflow by changing gap size

Figure 68 shows the time-averaged heat flux plotted along the platform measured from where the purge discharges into the channel. The straight design provides coolant further along the platform better as the gap increases. Design “X” shows very little variation as gap changes.

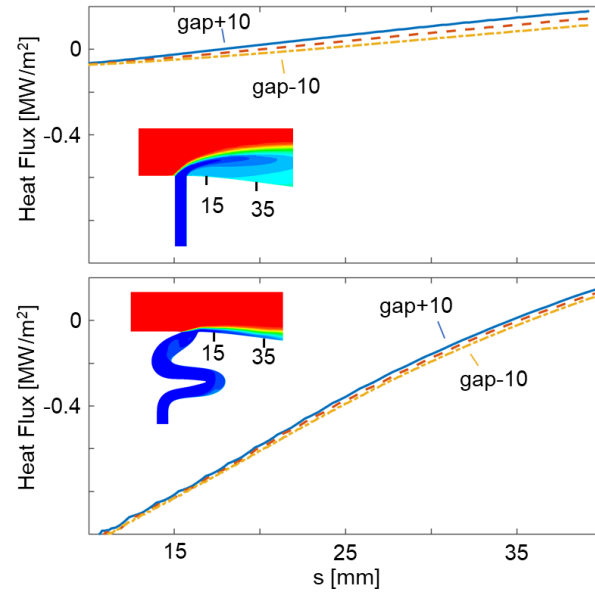


Figure 68. Heat flux along the platform for different gap sizes

5.2.6 Pressure Sensitivity

In a gas turbine engine, the cavity pressure changes during operation, Figure 69 shows the effects of changing the cavity pressure gap under constant gap. For the meander like designs (X,Y) increasing the pressure, reduces the heat flux in the rear platform. The straight design also reduces the heat flux however it is less effective at higher pressures.

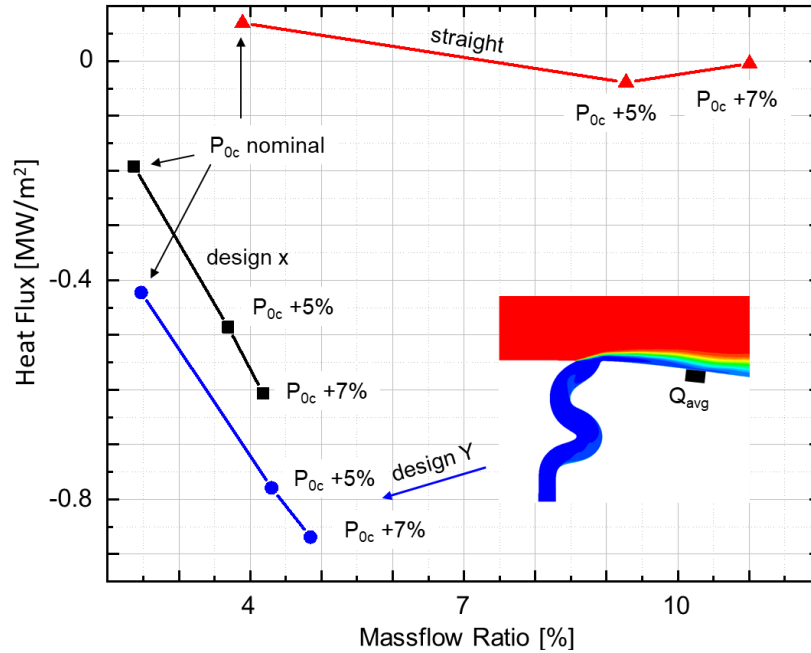


Figure 69. Heat flux along platform vs. massflow by changing pressure

5.3 Assessment in a Turbine Stage

5.3.1 Computational Domain

In 2D, design “X” was least sensitive towards gap and pressure changes, so it was compared with the straight purge in a 3D highly loaded turbine stage [101]. The computational domain consists of a stator-rotor cavity attached to the turbine inlet. To simplify the computation, the stator was not included. Figure 70 shows the computational domain created in SOLIDWORKS.

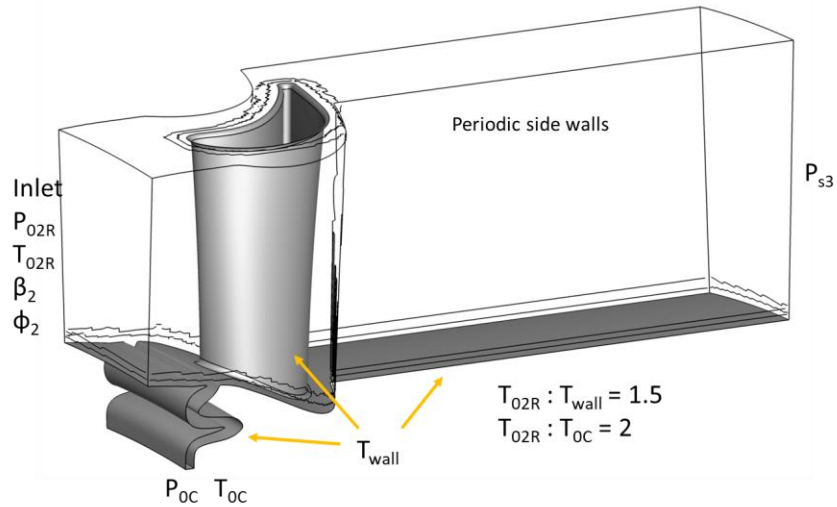


Figure 70. Optimized Geometry “B.” Rotation was applied to the stator walls

Table 16. Highly Loaded Turbine without Purge

Blades	r_{mean} [mm]	P_0/P_{s3}	RPM	r_p	ϕ	ψ	s/c
61	358	2.24	7500	0.32	0.49	2.3	0.72

5.3.2 Boundary Conditions and solver setup

The 3D mesh of the turbine and cavity was created using HEXPRESS with a size of around 9.7M cells. The inflation layer first cell height was 5E-7 m and contained a total of 40 layers. Y^+ was below 1. Periodicity was applied to the side walls. The mesh was solved using a Reynolds Averaged Navier Stokes solver, FINEOPEN.

Inlet rotor relative boundary conditions consist of pitchwise averaged P_{0r} , T_{0r} , pitch, and yaw flow angles from the stator. An outlet static pressure of 1.25 bar was imposed and an RPM of 7500 was applied to the stator platform. A wall temperature of 395K was applied to the turbine and platform. Purge total temperature was set to 293K. A hot gas to wall temperature ratio of 1.5 and hot gas to cool gas ratio of 2 was respected. Purge total pressure and gap was varied quantify the effects of the different designs on the turbine.

Table 17. Inlet and outlet boundary conditions for simulations with turbine

	P_{O2} [bar]	T_{O2} [K]	Re_u	RPM	P_{s3} [bar]	T_{wall1} [K]	T_{wall2} [K]
2D/3D Stationary	2.8	584	-	-	1.25	395	420
3D Rotation	2.8	584	1.48E7	7500	1.25	395	420

Table 18. Cavity boundary conditions when simulating with turbine

	P_{Oc} [bar]	T_{Oc} [bar]
2D/3D/Rotation	2.8	293

5.3.3 Comparison between 2D and 3D Stationary and Rotation

Figure 71 shows the pitchwise averaged Nusselt number inside the cavity. The 2D results are benchmarked against 3D stationary, and rotation, with and without the rotor. The simulations were compared to each other at a massflow ratio of 10% and an inlet mach number of 0.42. Total pressure within the cavity was set to 3.8 bars in the simulations without the turbine compared with 3.75 bar with turbine; this was done to match the massflow ratios. The blade does not have a large effect on the heat flux within the cavity. A 3D stationary design is able to capture the trend in heat flux. Liao et al. [102] reached similar conclusions from their experiments and numerical simulations of the cavity. They found that the heat transfer coefficient inside the cavity had little dependence on rotational Reynolds number.

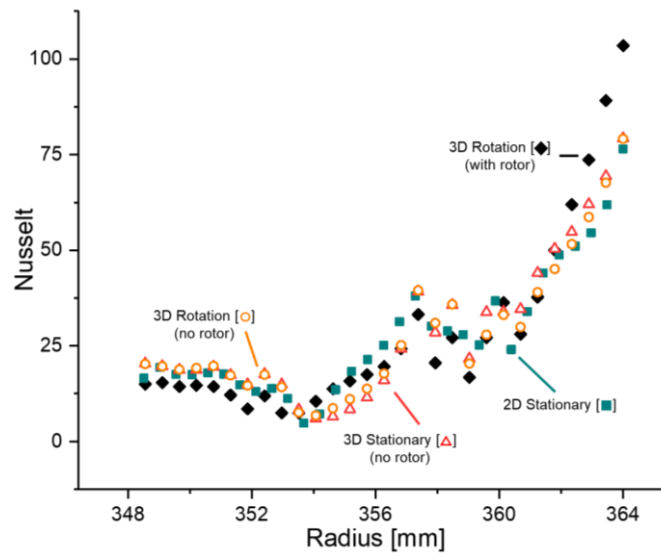


Figure 71. Nusselt number within cavity X

Figure 72 (a and b) shows iso-surface of constant rothalpy ($Cp[T_{0R}-U^2/(2Cp)]$) for the straight and design “X”. The cavity flow enhances the horseshoe vortex. In the straight purge, the horseshoe vortex has a wider spread; however, when the flow is ejected tangentially the horseshoe vortex becomes narrower. The platform heat flux is compared in Figure 72 (c and d). Design “X” provides a 150kW reduction in platform heat flux over the straight ejection; improving the cooling to the rotor platform was one of the goals of the optimization.

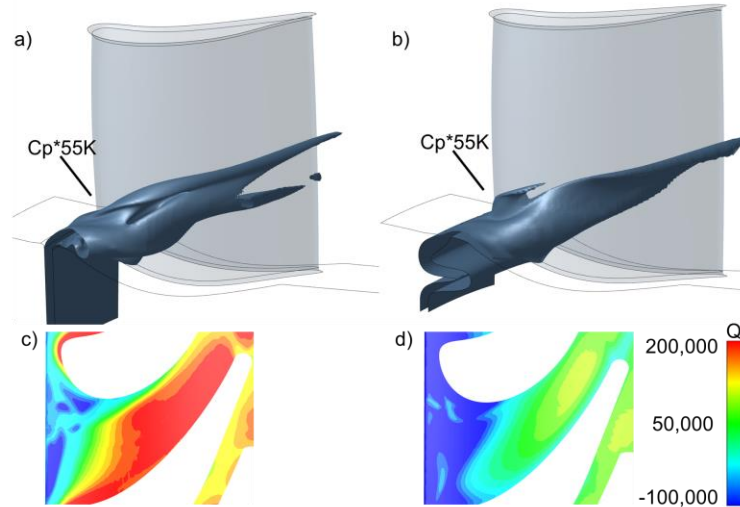


Figure 72. a,b) Secondary flows plotted with iso surface of rothalpy, massflow ratio 10% both cases. c,d) Platform heat flux.

5.3.4 Cavity impact on rotor performance

The Figure 73 shows the impact of changing the massflow ratio between the cavity and inlet on various turbine performance metrics. The massflow ratio was adjusted by changing the total pressure P_{0c} at the cavity inlet, this is similar to modeling the effect of losses upstream of the cavity. The three points in each plot in Figure 73 for both straight and design X represents cavity total pressures less than or equal to the inlet total pressure of the computational domain (Figure 73b). The stage efficiency shown in Figure 73a decays linearly as purge massflow increases. The decay rate of design X is higher, but the efficiency is limited to 91.8% because design X with its meander is less sensitive towards changes in total pressure than a straight ejection. For every 0.1 bar change in cavity pressure, the massflow ratio will decrease by 0.72% compared to the straight ejection where 1 bar change results in 2.53% increase in massflow ratio. All simulations were performed at iso-thermal conditions, therefore the heat dissipated and absorbed was

accounted for using the Atkins and Ainsworth [103] estimation of adiabatic efficiency (Equation 33). The heat transfer corrected value of efficiency is less than 0.3% from the adiabatic definition.

$$\eta_{stage,corr} = \frac{P_{mech} + Q_{rotor} + Q_{cav} + Q_{platform}}{\Delta H_{0,is} - \frac{T_{03}}{\Delta H_{0,is}} \left[\frac{Q_{rotor}}{0.5(T_{02} + T_{03})} + \frac{Q_{cav} + Q_{platform}}{0.5(T_{0c} + T_{03})} \right]} \quad (33)$$

$$\Delta H_{0,is} = mCp_w T_{01} \left(1 - \left(\frac{P_{03}}{P_{01}} \right)^{\frac{\gamma_w - 1}{\gamma_w}} \right) + mCp_w T_{0c} \left(1 - \left(\frac{P_{03}}{P_{0c}} \right)^{\frac{\gamma_w - 1}{\gamma_w}} \right) \quad (34)$$

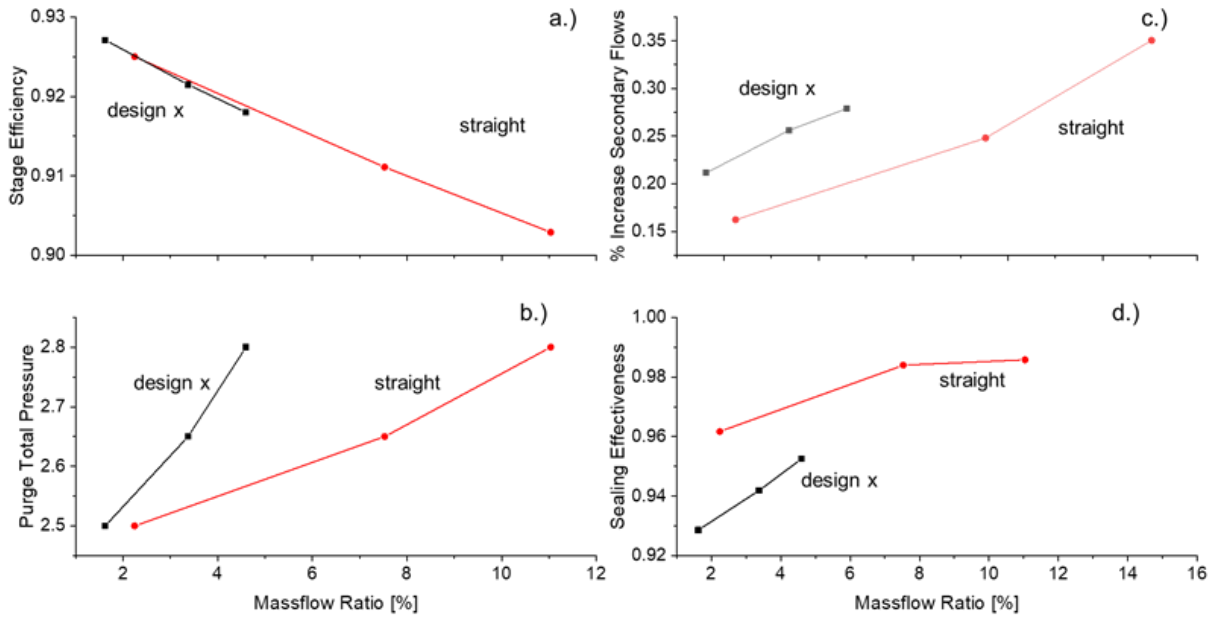


Figure 73. a) Stage Efficiency. b) Massflow Ratio. c) Increase in secondary flow. d) Sealing Effectiveness

Sealing effectiveness measures how well the seal is able to prevent ingestion of hot gases (Equation 35). Figure 73d shows that designs that ejecting radially provides the best seal, but as pressures approach the inlet pressure, secondary flow loss is higher than design “X”.

$$\eta_{seal} = \frac{T_{\infty} - T_{cav\ exit}}{T_{\infty} - T_{cav\ inlet}} \quad (35)$$

5.3.5 Effect of the gap spacing and leakage inlet pressure

Over the course of a turbine operation the cavity gap size changes and so does the pressure. Figure 74-Top, compares the corrected efficiency of the 2 cavity designs at 2 different cavity pressures and in 3 gap sizes. The solid line is design “X” and the dash line is the radial ejection. With design “X”, increasing the gap decreases the efficiency by 1%, but as gap increases to 20% there is no effect on the efficiency. Increasing P_{0c} decreases the efficiency by 0.5%. The straight purge shows less of a drop in efficiency around 0.5% gap increases but as pressure increases the efficiency drops by 1%.

Figure 74-Bottom compares the discharge coefficient of the two different designs. The discharge coefficient relates the purge massflow to the theoretical massflow you can achieve given the total conditions upstream and the static pressure downstream. Design “X” with its meandering geometry has a lower discharge coefficient making it more resilient towards changes in gap and pressure than the straight design. This also means that at the same P_{0c} conditions the meander-like design will enable the turbine to operate at a higher efficiency with lower massflow ratios.

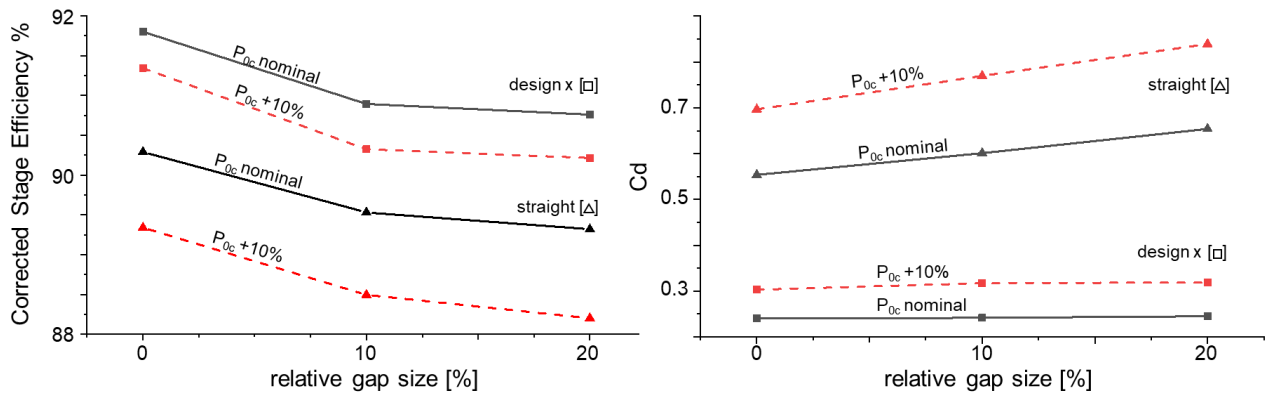


Figure 74. Top: Corrected efficiency vs. gap and pressure. Bottom: Discharge coefficient vs. gap

5.4. Development of an Experimental Methodology

Unsteady Reynolds Average Navier-stokes simulations can predict regions of separation however they have difficulty in predicting reattachment point [58]. Additionally, heat flux is difficult to predict using Reynolds Averaged Navier Stokes simulations (RANS). RANS often overpredicts the heat flux [104–107]. An experiment performed at engine level mach numbers is needed to verify the design of the cavity. Optical measurement techniques such as PIV can also be used to visualize the flow structure and can be used for CFD validation. To accomplish this, the engine scale design should be scaled up by 10x or 5x depending on how much visual access is needed into the cavity width (20mm or 10mm).

The Linear Experimental Apparatus for novel Testing (LEAF) [108]. LEAF is modular linear test section, it has a dimension of 230 mm wide by 170mm in height and a length of 543 mm with full optical access; it is the ideal candidate to test new cavity designs at low TRL. The results of the cavity optimization has demonstrated that in the rotational frame of reference, a 2D cavity design can predict the heat flux trend of the 3D stationary and rotation [109]. To test the cavity in the linear test section, a separate air supply must be routed underneath the linear test section. Additionally, the bottom plate of the linear test section must be redesigned to allow the installation of different cavity geometries. There is 37 inches (940 mm) of available space below the linear test section to fit a settling chamber and a contraction that will route the flow to the test section.

5.5 Experimental Design of the Test Article Methodology

The design of the test article was completed using two steps. The first step considers the aerodynamic conditions within the linear test section and compares it to the engine channel design minus the turbine and the stator. The objective of this first step is to match isentropic mach number along the surface of the linear test section (Figure 76) with the engine geometry (Figure 75) but at scaled conditions. The second step considers the channel with a cavity and matches the isentropic mach number along the wall of the cavity by changing the total pressure at the cavity inlet.



Figure 75. Channel geometry without stator, rotor, or purge



Figure 76. Test Article 5x scaled

Scaling of 5x was chosen because it was large enough to measure inside the cavity while also small enough that the top wall of the linear test section does not interfere with the flow physics of the cavity. The scaled geometry (Figure 76) extends further than the 544mm length constraint of the linear test section; this is not an issue, because the objective is to make sure the cavity is visible from the windows of the linear test section and match the mach number just before the cavity.

5.5.1 Boundary Conditions

The boundary conditions of the computational domain (Figure 75 and Figure 76) include total pressure and temperature at the inlet (P_{02} and T_{02}) and static pressure at the outlet (P_{s3}). The ratio of total pressure at the inlet to the static pressure at the outlet was selected to match a mach number of 0.3 through the domain. The boundary conditions listed in Table 19 matches the mach number inside the channel with the mach number linear test section within 0.02, see Figure 77. Figure 78 shows the Mach number in the channel for both the linear test section and in the engine. The dotted line indicates where the massflow weighted mach number was matched between the two simulations.

Table 19. Scaled Boundary Conditions

Channel		
P_{02}	bar	30
T_{02}	K	1700
P_{s3}	bar	28.9
Linear Test Section		
P_{02}	bar	3
T_{02}	K	450
P_{s3}	bar	2.92

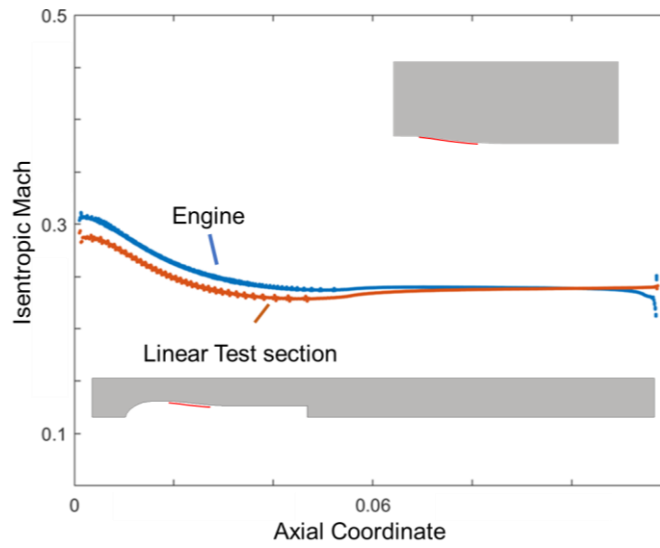


Figure 77. Isentropic mach number along the channel and linear test section test article

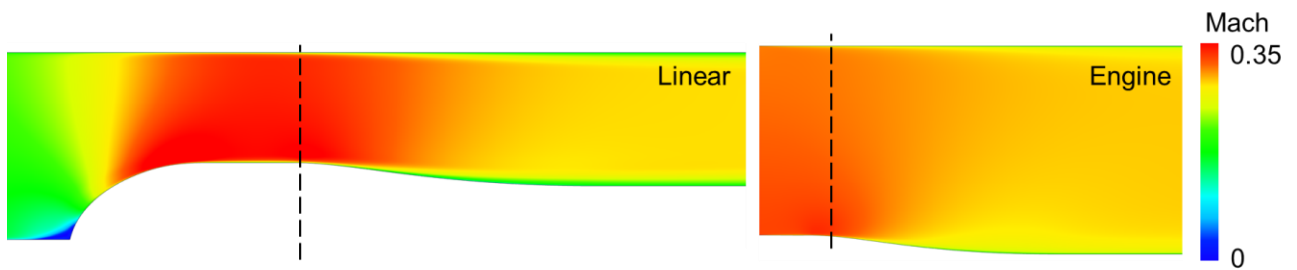


Figure 78. Mach number contour. Left: Linear. Right: Engine boundary conditions and geometry. Dotted line: start of the cavity

5.5.2 Matching Cavity Isentropic Mach and Nusselt

The strategy, described in Figure 79, for matching the mach number within the cavity begins with a guess total pressure for the cavity inlet. The mach number along the inside of the cavity was then plotted with the purge design from Chapter 2. Isentropic relation for total-to-static pressure and mach number is used to find the static pressure at a reference point. This static pressure is then used to calculate the new total pressure in the cavity of the linear test section in order to match the mach number in the purge design of the engine.

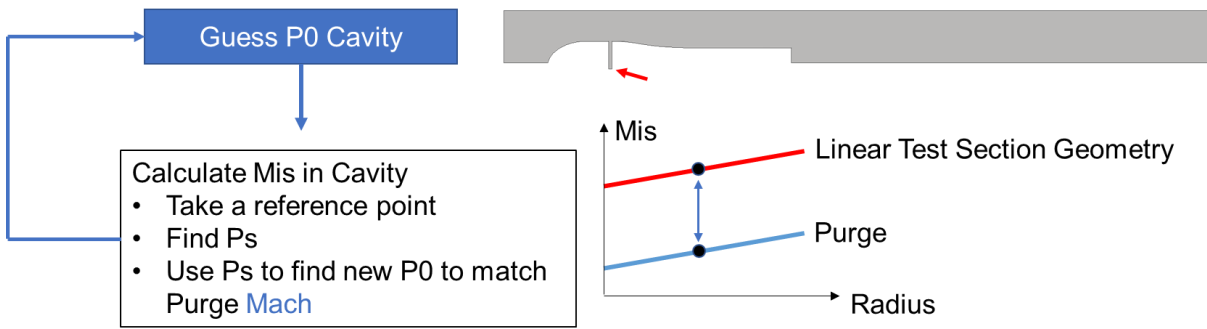


Figure 79. Cavity Total Pressure selection strategy

The radial ejection cavity design was scaled by 5x and simulated inside the linear test section. Table 20 contains the boundary condition of the cavity used to match the engine simulations. Boundary conditions at the inlet and outlet match Table 19. The rotor wall was simulated with the same coolant-to wall ratio 2:1, and hot flow to wall temperature ratio, 1.5, as in the engine simulation. The total pressure at the inlet of the cavity (P_{0c}) was iterated to match the isentropic mach number along the walls.

Table 20. Cavity Inlet Boundary Conditions

Cavity Inlet		
P_{0c}	Bar	2.97
T_{0c}	K	225

Figure 80 compares the isentropic mach number along the wall inside the linear test article with the cavity under engine level conditions for two different geometries, radial ejection (Left) and the meander geometry (Right). The isentropic mach number inside the cavity was

reproduced with an accuracy less than 0.02 mach for both designs. The same turbulence intensity from the engine was imposed on the cavity inlet when performing the simulations.

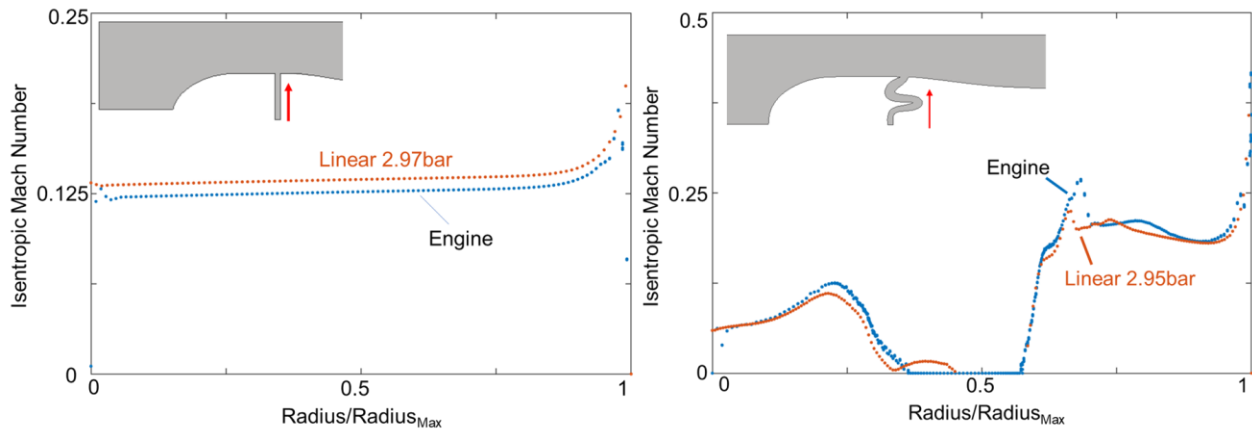


Figure 80. Straight Purge Isentropic mach number, purge comparison with linear

Comparing the flowfield of the linear test section with the engine conditions reveals slight differences in the mach number near the purge exit (Figure 81). This is due to the design of the initial ramp at the inlet of the linear test section. The ramp was slightly modified for the meandering geometry (design X) shown in Figure 82. This produced more blockage by 4%. Despite the differences in the inlet flowfield, the mach number along the walls of the cavity can be accurately replicated by both cavity designs.

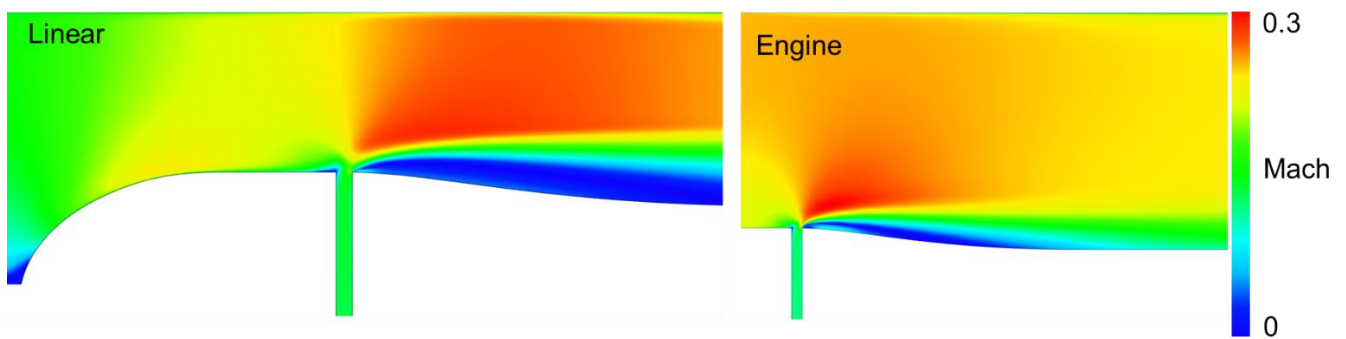


Figure 81. Straight purge Mach Number. Left: Linear test section. Right: Engine

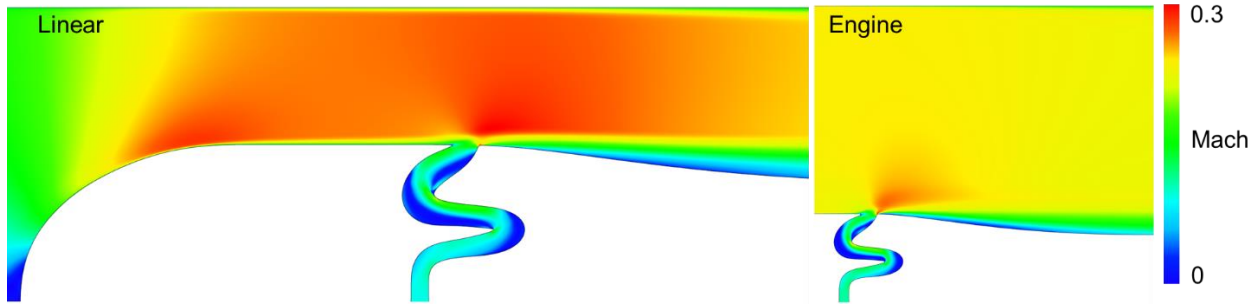


Figure 82. Design X Mach Number. Left: Linear test section. Right: Engine

5.6 Experimental Requirements

The experimental hardware needed to test cavity geometries should be capable of testing massflow ratios up to 12% of the mainflow, this is required sensitivity studies. Blowing ratios are a function of the geometric design, a radial ejection will have a higher blowing ratio than a meander-like design. Table 21 shows the desired experimental conditions for cavity flow simulations. The desired scaling factor for the cavity width is 5x, any number higher results in the top window interfering with the cavity flow.

Table 21. Experimental Requirements

Geometry Requirements		Test Conditions	
Linear Test Section		Cavity Massflow	0-1.5 kg/s
- Height	170mm	Freestream Mach	0.3-0.45
- Width	230mm	Settling chamber exit mach	0-0.8
Engine Scale Cavity			
- Height	50mm		
- Min Width	2 mm		
Scale CFD to Experiment	5x		
Cavity Test Article			
- Height to top window	100mm		
- Cavity Width	10mm		

5.7 Design of the Settling Chamber

The objective of the settling chamber is to deliver uniform flow into the test article. Two sets of parameters are essential towards providing uniform flow entering the test section: the inlet area to contraction area ratio (Equation 36) and the contraction length. Ideally, it is desired to have a large area ratio and a long contraction length. Bell and Mehta [111] recommended contraction ratios around 6 to 10 for their low speed tunnel ($U < 40$ m/s). They used a length to inlet height ratio of 1 to 1.8. Morel [112] discovered that the length to diameter ratio decreases with increasing contraction ratio. Figure 83 shows two designs that were used to launch the design of the settling chamber.

$$\text{Contraction Ratio} = \frac{\text{Inlet Area}}{\text{Outlet Area}} \quad (36)$$

5.7.1 1 to 2 Inlets with inner casing

The single inlet type of design was inspired by settling chambers used in the VKI for probe calibration. With a single inlet design, you can have a small inlet area and a large outlet area, but this also means that the flow will have to be injected through one side and diffuse around the settling chamber walls then finally pass through the contraction and leave through the top. This is the simplest design from a manufacturing point of view. Screens are typically installed inside the settling chamber, however for this design exploration, screens will not be considered, because they are too complicated and time consuming to model. The objective will be to minimize the pitch and yaw variations at the exit of the settling chamber.

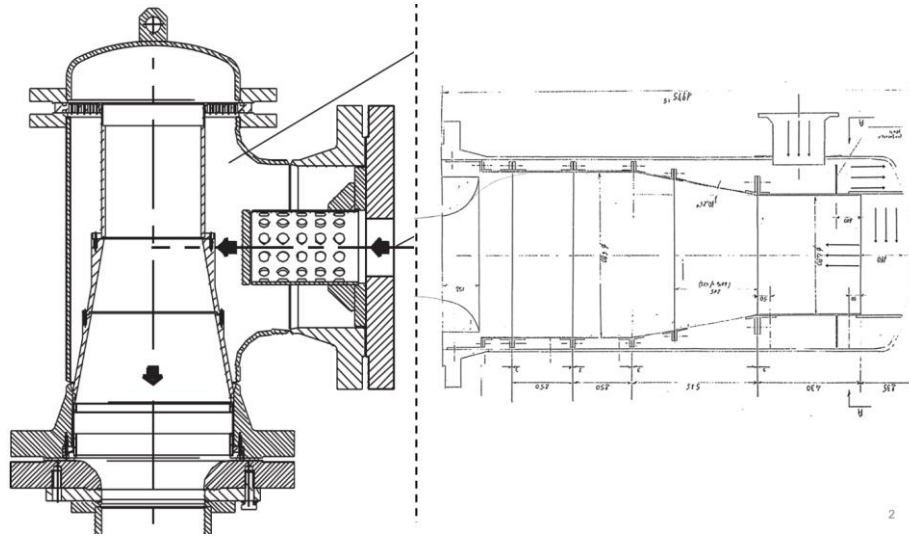


Figure 83. Left: Settling chamber used in the VKI C4 tunnel. Right: Settling chamber used in the VKI C3 tunnel.

A single inlet design was simulated in steady state using Reynolds Averaged Navier Stokes without the contraction that leads into the linear test section. What happens with this type of design is that the air impinges on the inner wall and wraps around the inner walls of the settling chamber at high mach numbers, this creates swirl and a large recirculation bubble of different sizes in the nozzle part of the settling chamber.

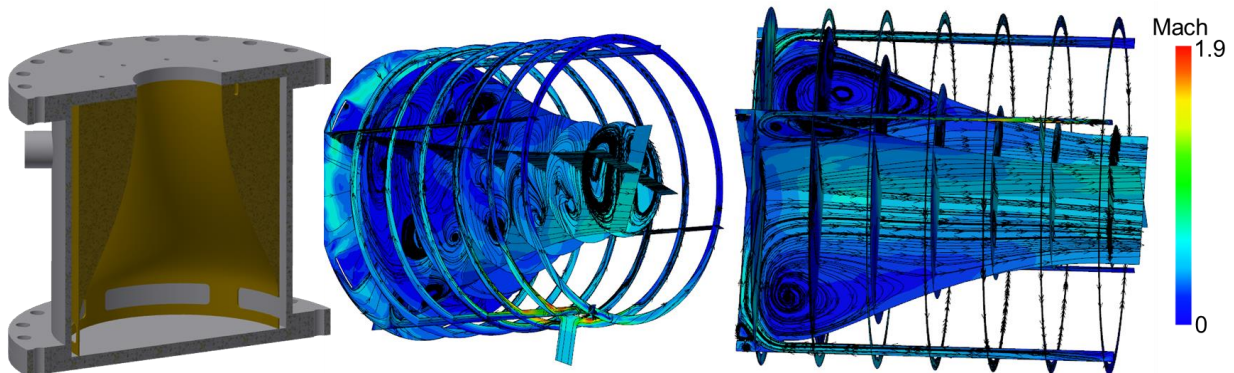


Figure 84. Settling chamber with single inlet

Table 22. Boundary conditions for single inlet design without contraction

	Single Inlet	Double Inlet
Inlet P_0 [bar]	3	1.5
Outlet P_s [bar]	1	1
Massflow [kg/s]	4.32	4.32

Increasing the number of inlets could reduce the swirl, a double inlet design was simulated. Having two inlets also produced a lot of swirl and large recirculation bubbles within the settling chamber. Injecting flow at the sides into the wall is not good practice. The next section explores injecting the flow at the base and compares the exit pitch and yaw angles with a contraction mounted.

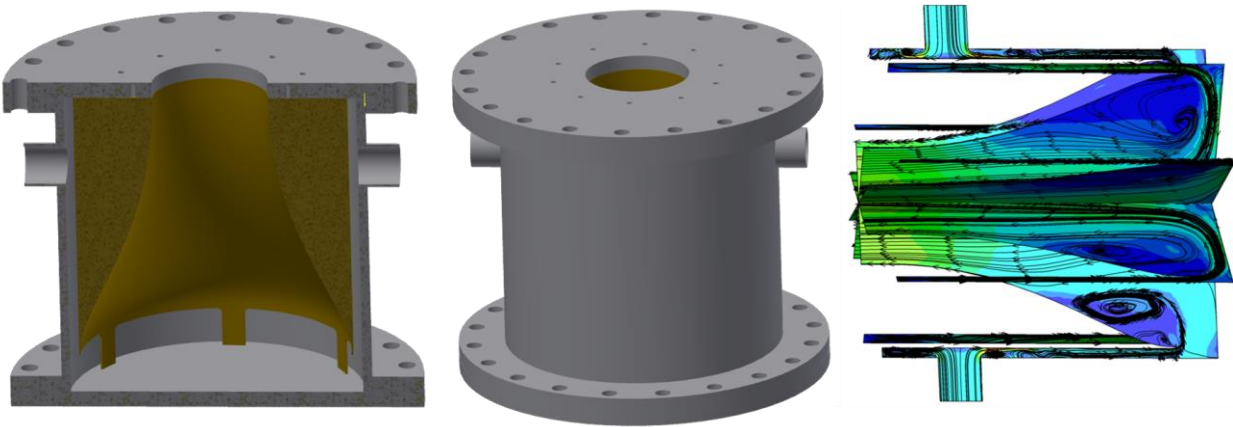


Figure 85. Double inlet settling chamber

5.7.2 1, 2, 4, and 8 Inlets without inner casing

A single and double radial inflow inlet design with an inner casing resulted in large swirl. Increasing the number of inlets and reducing the total pressure could help reduce the swirl. In this section a 1, 2, 4, and 8 inlet designs were tested, the inlet was moved to the base and a contraction was added at the exit. Figure 86 compares the 4 different settling chamber inlet designs. Having a single inlet creates large variations in pitch and yaw; increasing the inlets results in more uniform exit flow.

Table 23. Settling chamber boundary conditions with 20 mm contraction

	1 Inlet	2 Inlets	4 Inlets	8 Inlets
Inlet P_0 [bar]	1.77	1.55	1.38	1.35
Inlet T_0 [K]	300	300	300	300
Outlet P_s [bar]	1	1	1.01	1
Massflow [kg/s]	1.257	1.29	1.26	1.25

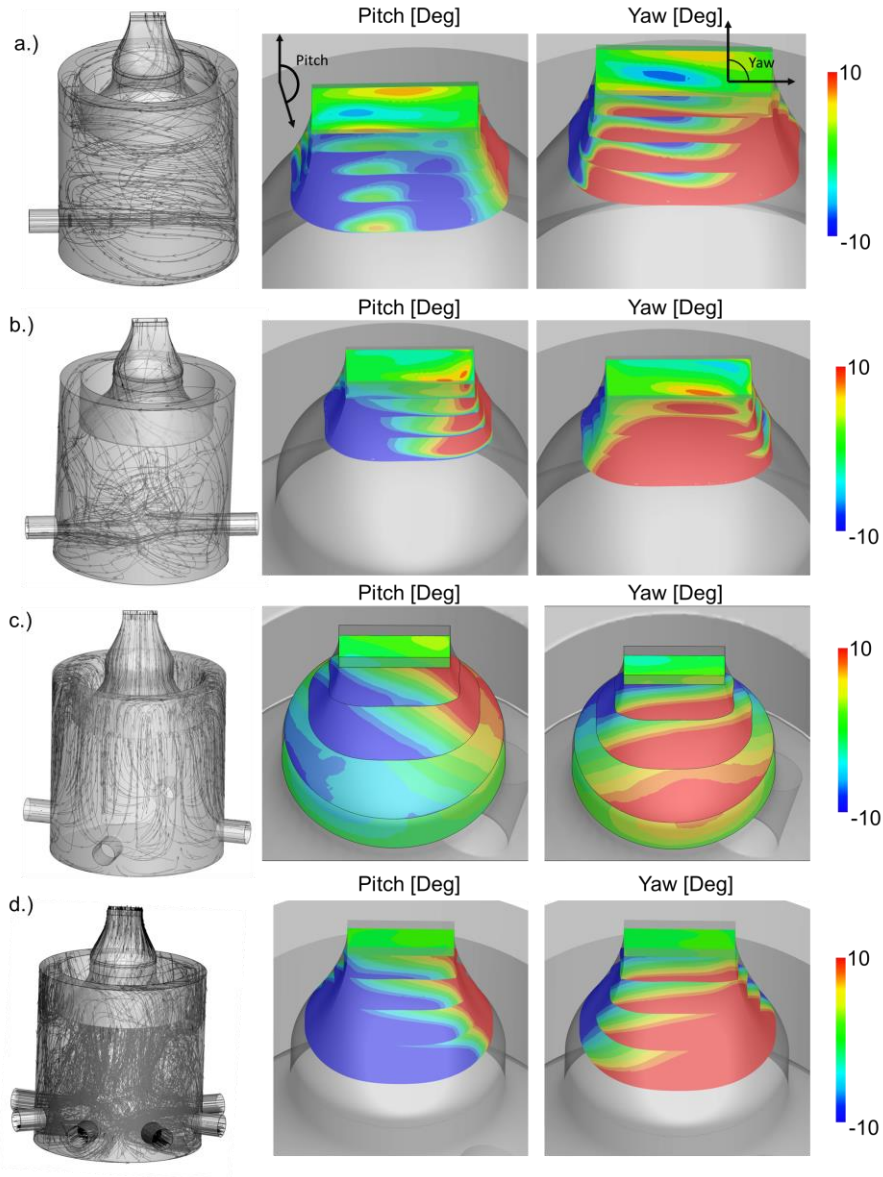


Figure 86. Settling chambers with contraction. a.) single inlet b.) double inlet c.) 4 inlets d.) 8 inlets

Out of all the options explored, the best option was to inject the flow using 8 inlets to reduce the max pitch and yaw angle variations to less than 2 degrees. Simulations were performed with a contraction exit width of 20mm. 20mm is the ideal cavity gap in the linear test section but having such a gap would compromise visual access. To gain full visual access a smaller contraction width of 10mm is needed. With a 10mm width the variations in pitch and yaw angles was found to be less than 0.1 degrees. The length of the settling chamber and contraction geometry were designed to fit in the space under the linear test section. The final height of the settling chamber and contraction geometry is 33.5". The contraction has an inlet to exit area ratio of 17.9 assuming 10mm width. The relationship between the inlet total pressure in the settling chamber to the contraction exit mach number (black squares) and massflow (red circles) is shown in Figure 88.

Table 24. Settling chamber flow exit properties 20mm contraction

	1 Inlet	2 Inlets	3 Inlets	4 Inlets
Massflow Avg Pitch [Deg]	0.27	-0.04	0.02	0.15
Massflow Avg Yaw [Deg]	0.33	-0.07	-0.05	0.17
Max Pitch [Deg]	8	8	3	1.8
Max Yaw [Deg]	6	7	4	1.5

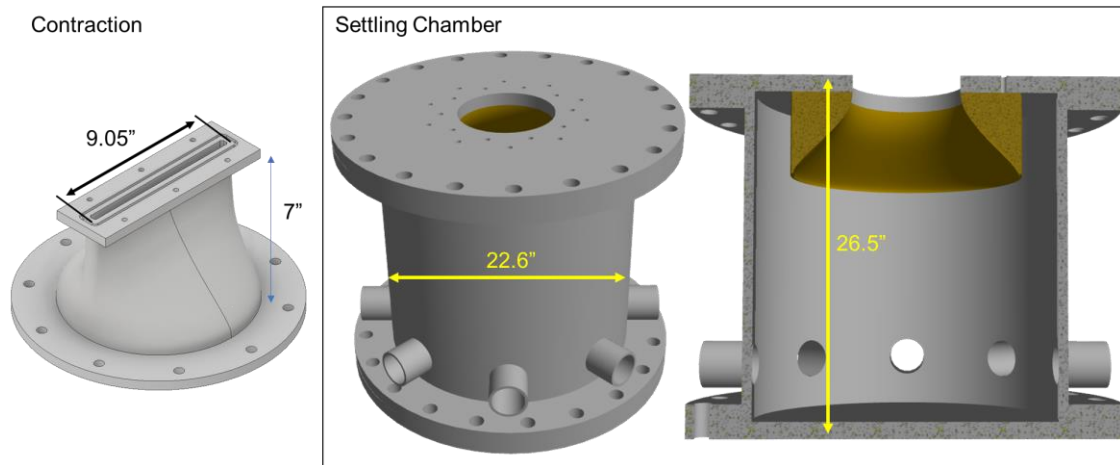


Figure 87. Left: Contraction Geometry and dimensions. Middle: Settling chamber and dimensions. Right: Settling chamber cross section

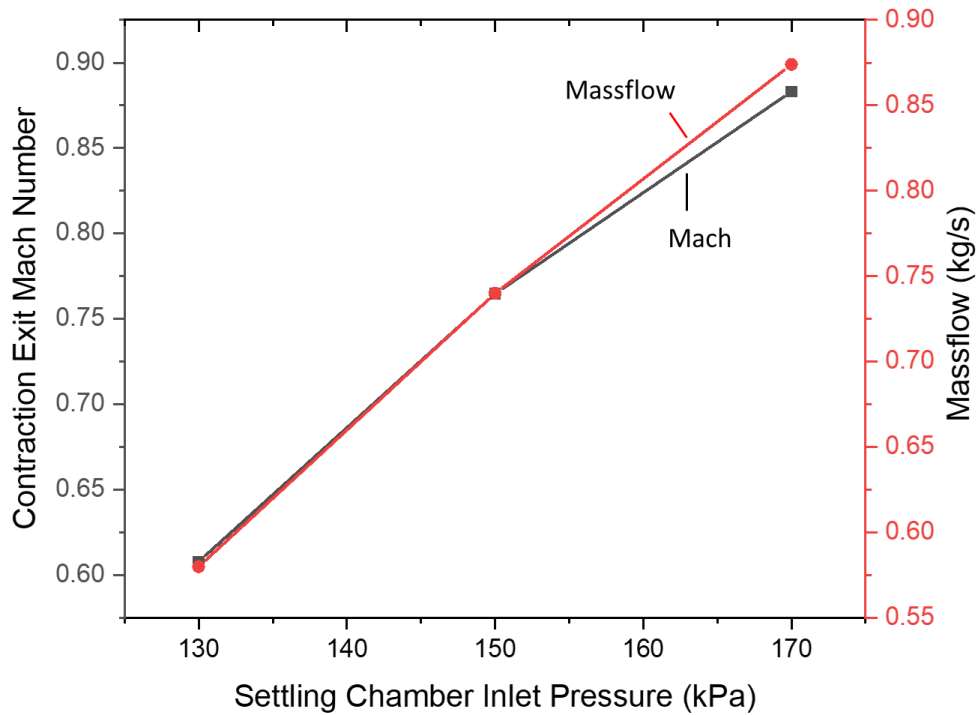


Figure 88. Settling Chamber contraction exit mach number and massflow vs. inlet total pressure simulated with 10mm contraction width

5.7.3 Linear Test Section Hardware

The bottom window of the settling chamber was replaced with a mounting plate. The plate was designed to eject flow at the widest possible width into the linear test section. An adapter was made to connect to the contraction (Figure 89) and screwed on to the plate. The test article screws directly onto the mounting plate. The assembly is shown in Figure 90.

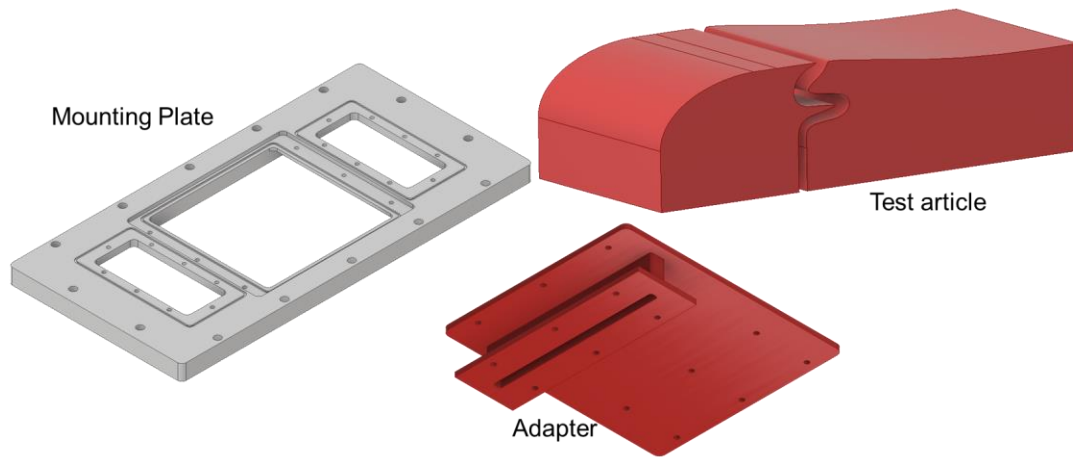


Figure 89. Mounting Hardware Linear Test Section

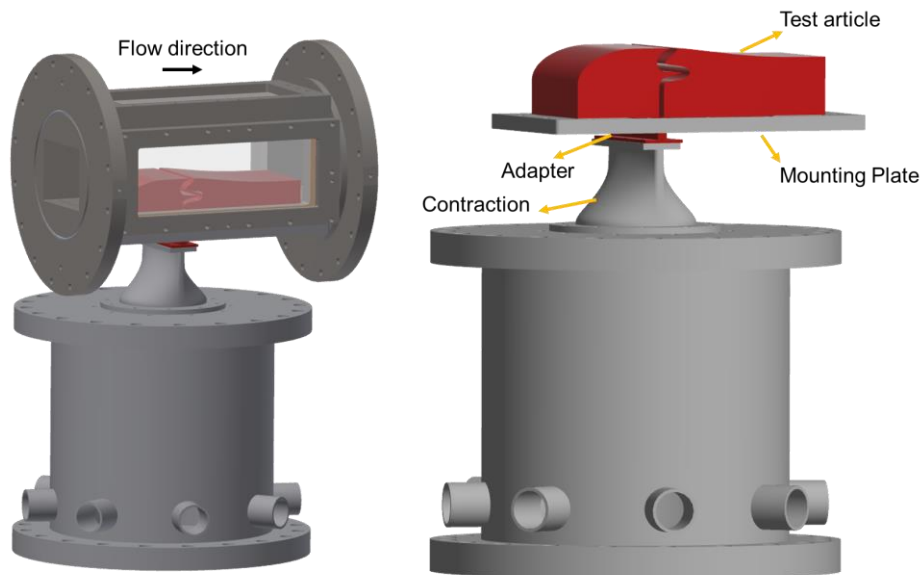


Figure 90. Left: Linear test section with purge hardware. Right: Settling chamber with the purge hardware

CONCLUSION

Weight reduction and environmental concerns drive the need for efficient turbines that are highly loaded. A full stage multi-objective optimization is needed to study the full design space so that a compromise between efficiency and loading can be realized. New propulsion architectures can cause the turbine to operate at highly loaded off-design conditions. The exploration of bio and nature-inspired design strategies can lead to blade designs that are more incident tolerant and resilient to changes in gap and pressure.

A Full 3D optimization of a turbine stage was performed with a newly developed design tool. A fast 1D mean-line optimization to identify an ideal lab environment to safely test an efficient highly loaded turbine stage and the target stage flow angles. This procedure was followed by a full 3D parameterization using an in-house code. The code was paired with an optimizer to perform a combined optimization of the stator, rotor, and channel geometry using a total of 75 design parameters. The aerodynamic efficiency of the turbine was simultaneously maximized with the stage loading, generating a Pareto front of prime turbine designs. The optimization yielded a wide variety of possible designs, allowing the investigation of loss-generation in both the stator and rotor. The stator losses reached values up to 12% for turning higher than 76 degrees, however, they can be kept as low as 6-7% if one limits the turning and degree of reaction. Additionally, the lowest losses were observed for the geometries combining the minimum constrained stagger angle of 55 deg. with high pitch-to-chord ratios (up to 0.9) in a regime of low turning. A proper optimization of the rotor blade design can limit the loss generation to 10% for turning angles up to 110 degrees. From this point on, the losses increase significantly up to 15% for a turning angle of 125 deg. Furthermore, most of the rotor blade profiles along the Pareto front adopt a pitch-to-chord ratio of 0.7 to 0.75, stagger angles between 40 and 45 degrees, and feature a lean of the tip section towards the direction of rotation. Highly loaded designs that have the best efficiency have less stagger at the hub and tip. Furthermore, they experience high loading near the leading edge followed by diffusion and loading increases in the aft portion of the blade.

Using the database of possible designs, the mechanical efficiency was compared with the Horlock efficiency, computed using kinetic losses from stator and rotor. The comparison

revealed a mismatch in the trend due to the rotor exit Mach numbers. A correction to the Horlock equation was proposed using the trends of stator and rotor exit Mach number improved the accuracy for the turbine performance estimation from aerothermal measurement data to $\pm 0.01\%$.

Newly optimized Bio-inspired designs have been identified with an in-house wavy design tool. The design tools created for optimizing turbine shapes were modified to include the parameterization of wavy shapes on the blade surface. An optimization campaign was pursued on an existing optimal geometry design to improve its performance at positive 15 degrees incidence. The optimized wavy blade was able to marginally improve the efficiency in the rotor-only simulations while maintaining the same amount of massflow, turning, and work output. The stage simulations show a higher improvement in stage efficiency of 1.2%. Improvements at off-design resulted in a decrease in efficiency and higher losses at design point. Not all waviness in nature are equal. The same is true for applying the waves on a turbine. The optimization revealed 286 different designs. At the leading edge it was advantageous to have 3 waves and no waves on the suction side and 2 waves on the trailing edge. Designs that have higher pressure loss are those that have wave frequencies higher than 3 in either leading edge, suction side, or trailing edge. The leading edge impacts the separation on the suction side. A large wave acts as an obstacle slowing down the flow as it moves from pressure side to suction side. The waves cause vortices to form in the translational direction. The vortices rotate in opposite directions as the flow moves past the leading edge.

Investigating the static pressure, the waves at the leading edge help reduce the size of the recirculation bubble by accelerating the flow over the leading through the valleys. At the hills, the flow is decelerated. This is as direct impact on the secondary flows and the shock structure. The optimized wavy blade has a high exit Mach number than the baseline. There is also less secondary flow loss. Positive incidence makes the blade more front loaded which increases the profile and secondary flow losses. The optimized design's wavy shape makes the blade more aft loaded. A cut plane at the hills and valleys shows reduced front loading. Additionally, the loading near the trailing edge is increased by the higher exit mach number.

Overall wavy designs can help reduce loss at incidence for highly loaded geometries, but losses can be improved further by revisiting the velocity triangles and designing a blade that is incident tolerant without the use of waves that is a compromise between two design points.

However, if waves are going to be implemented, an optimization can reveal designs that reduce loss while also keeping the massflow, turning, and loading the same.

The design of the stator-rotor rim seal was optimized to protect the rotor platform. 2D simplification of the stator-rotor rim seal allowed for an optimization which revealed cavity design trends that showed a trade-off between the massflow and temperature of the fluid above the rear platform. The optimization required URANS to model the unsteady rolling of vortices past the meanderings. Cavity designs that eject coolant at angles of 20 to 30 degrees proved to be the best at cooling the rear and front of the rotor platform. Designs that allow higher massflow have less temperature fluctuations in the rear platform. High purge flow rates result in higher blockage which decrease the turbine efficiency; but blockage can be reduced by allowing purge flow to exit at low flow angles and by increasing the cavity overlap. The meander-like cavity design with the most overlap proved to be least sensitive to variations in gap and purge total pressure.

The optimized design was compared against a radial ejection geometry in a 3D computational domain which included the rotor with pitchwise averaged boundary conditions from the stator imposed at the inlet. The optimized design was finally assessed in a turbine stage demonstrating a significant amelioration to protect the rear platform and was more resilient towards changes in gap and purge total pressure. The present thesis should help designers understand the effects of simplifying the cavity physics. The simplification can reduce the time to develop more efficient stator-rotor cavities and lead to assessments in a linear wind tunnel where cavity designs can be 3D printed and evaluated quickly.

FUTURE WORK

Turbine Design

Use of dataset in cloud computing

Design and optimization have been around for years, it has been a vital tool in designing airfoils. But what happens after the optimization campaign has finished? Often the results of these campaigns are archived. Instead what should be done, now with cloud computing and the availability of NoSQL databases, it is possible to store the results of large datasets to the cloud. Once the data is in the cloud machine learning models can be developed to improve correlations and update existing design tools. This by itself is a momentous task and will require numerous optimization campaigns, normalization, and programming skill.

Nature Inspired Airfoil

Methodology Future Changes

One of the greatest challenges in designing the wavy blade is the mesh. Depending on the number of waves, the frequency, phase, and amplitude, the mesh can fail. Also, the skewness of the cells affects the convergence. Unconventional designs should be evaluated using an unstructured mesh.

In this optimization, I kept the massflow constant at off-design conditions to maintain similarity with the baseline; however instead of keeping the massflow constant at off-design, efforts should be made to keep it constant at on-design. If the waves reduce the recirculation bubble, this should allow more massflow through the passage.

Structural considerations

Wavy designs need to be evaluated for flutter and force response and compared with the baseline geometry. Unsteady simulations with the stator should also be evaluated in the future. It would be interesting to find out what happens when a wavy leading edge is exposed to the wakes and

shocks coming from the stator. Additionally, it would be beneficial to create a database of designs and harmonic frequencies.

Cavity Design

Ingestion Free Design

In this thesis, the cavity was optimized in 2D in the rotor relative frame in order to protect the rotor platform. However, there is still a problem of ingestion. I suggest that future studies look at optimizing the stator-platform above the cavity in the absolute frame. The optimization objective should be a uniform pressure distribution just before the cavity exit into the main flow path. This new strategy can be evaluated in 3D by taking the computational domain of the stator and unwrapping it into a rectangle or R- θ -Z coordinate system. A surface of the static pressure vs θ and R can be imposed as the boundary condition into a rectangular domain. Additionally, by viewing the design in R- θ -Z coordinate system, this enables low TRL testing in a linear wind tunnel. This new methodology may help prevent ingestion of hot gases. Combining this new strategy with the one outlined in this thesis is a future step to prolonging the life of the turbine disk and blades.

REFERENCES

- [1] Hawthorne, W. R., 1955, “Rotational Flow Through Cascades Part I. The Components of Vorticity,” *The Quarterly Journal of Mechanics and Applied Mathematics*, **8**(3), pp. 266–279.
- [2] Hawthorne, W. R., and Armstrong, W. D., 1955, “Rotational Flow Through Cascades Part II. The Circulation about the Cascade,” *The Quarterly Journal of Mechanics and Applied Mathematics*, **8**(3), pp. 280–292.
- [3] Langston, L. S., 1980, “Crossflows in a Turbine Cascade Passage,” *Journal of Engineering for Gas Turbines and Power*, **102**(4), pp. 866–874.
- [4] Sieverding, C. H., 1985, “Recent Progress in the Understanding of Basic Aspects of Secondary Flows in Turbine Blade Passages,” *Journal of Engineering for Gas Turbines and Power*, **107**(2), p. 248.
- [5] Sharma, O. P., and Butler, T. L., 1987, “Predictions of Endwall Losses and Secondary Flows in Axial Flow Turbine Cascades,” *Journal of Turbomachinery*, **109**(2), pp. 229–236.
- [6] Goldstein, R. J., and Spores, R. A., 1988, “Turbulent Transport on the Endwall in the Region Between Adjacent Turbine Blades,” *Journal of Heat Transfer*, **110**(4a), p. 862.
- [7] Sieverding, C. H., and Van den Bosche, P., 1983, “The Use of Coloured Smoke to Visualize Secondary Flows in a Turbine-Blade Cascade,” *Journal of Fluid Mechanics*, **134**(1), p. 85.
- [8] Denton, J. D., 1993, “Loss Mechanisms in Turbomachines,” *Journal of Turbomachinery*, **115**(4), p. 621.
- [9] Zoric, T., Popovic, I., Sjolander, S. A., Praisner, T., and Grover, E., 2007, “Comparative Investigation of Three Highly Loaded LP Turbine Airfoils: Part I — Measured Profile and Secondary Losses at Design Incidence,” *Volume 6: Turbo Expo 2007, Parts A and B*, ASME, pp. 621–630.
- [10] Weiss, A. P., and Fottner, L., 1995, “The Influence of Load Distribution on Secondary Flow in Straight Turbine Cascades,” *Journal of Turbomachinery*, **117**(1), p. 133.
- [11] Dossena, V., D’Ippolito, G., and Pesatori, E., 2004, “Stagger Angle and Pitch-Chord Ratio Effects on Secondary Flows Downstream of a Turbine Cascade at Several Off-Design Conditions,” *Volume 5: Turbo Expo 2004, Parts A and B*, ASME, pp. 1429–1437.
- [12] Hodson, H. P., and Dominy, R. G., 1986, “The Off-Design Performance of a Low Pressure Turbine Cascade,” *Volume 1: Turbomachinery*, ASME, p. V001T01A077.

- [13] Corriveau, D., and Sjolander, S. A., 2004, “Influence of Loading Distribution on the Performance of Transonic High Pressure Turbine Blades,” *Journal of Turbomachinery*, **126**(2), p. 288.
- [14] Perdichizzi, A., and Dossena, V., 1993, “Incidence Angle and Pitch-Chord Effects on Secondary Flows Downstream of a Turbine Cascade,” *Journal of Turbomachinery*, **115**(3), pp. 383–391.
- [15] Benner, M. W., Sjolander, S. A., and Moustapha, S. H., 2004, “The Influence of Leading-Edge Geometry on Secondary Losses in a Turbine Cascade at the Design Incidence,” *Journal of Turbomachinery*, **126**(2), pp. 277–287.
- [16] Sieverding, C. H., “Advanced Course on Turbines.”
- [17] Corriveau, D., and Sjolander, S. A., 2007, “Influence of Loading Distribution on the Off-Design Performance of High-Pressure Turbine Blades,” *Journal of Turbomachinery*, **129**(3), p. 563.
- [18] Eric Lyall, M., King, P. I., Clark, J. P., and Sondergaard, R., 2014, “Endwall Loss Reduction of High Lift Low Pressure Turbine Airfoils Using Profile Contouring—Part I: Airfoil Design,” *Journal of Turbomachinery*, **136**(8), p. 081005.
- [19] Praisner, T. J., Grover, E. A., Knezevici, D. C., Popovic, I., Sjolander, S. A., Clark, J. P., and Sondergaard, R., 2013, “Toward the Expansion of Low-Pressure-Turbine Airfoil Design Space,” *Journal of Turbomachinery*, **135**(6), p. 061007.
- [20] McQuilling, M. W., “Design and Validation of a High-Lift Low-Pressure Turbine Blade,” p. 143.
- [21] Denton, John, 2018, “The Evolution of Turbomachinery Design Methods.”
- [22] Shelton, M. L., Gregory, B. A., Lamson, S. H., Moses, H. L., Doughty, R. L., and Kiss, T., 1993, “Optimization of a Transonic Turbine Airfoil Using Artificial Intelligence, CFD and Cascade Testing,” *Volume 3A: General*, ASME, p. V03AT15A012.
- [23] Sousa, J., and Paniagua, G., 2015, “Entropy Minimization Design Approach of Supersonic Internal Passages,” *Entropy*, **17**(8), pp. 5593–5610.
- [24] Joly, M. M., Verstraete, T., and Paniagua, G., 2014, “Integrated Multifidelity, Multidisciplinary Evolutionary Design Optimization of Counterrotating Compressors,” *Integrated Computer-Aided Engineering*, **21**(3), pp. 249–261.
- [25] Joly, M. M., Verstraete, T., and Paniagua, G., 2013, “Differential Evolution Based Soft Optimization to Attenuate Vane-Rotor Shock Interaction in High-Pressure Turbines,” *Applied Soft Computing Journal*, **13**(4), pp. 1882–1891.

- [26] Thorn, C. R., and Hartfield, R. J., 2016, “Three Dimensional Turbine Blade Optimization Using Evolutionary Algorithm with Viscous Flow Analysis,” AIAA SciTech Forum, pp. 1–20.
- [27] Pau, M., Paniagua, G., Delhayé, D., de la Loma, a., and Ginibre, P., 2010, “Aerothermal Impact of Stator-Rim Purge Flow and Rotor-Platform Film Cooling on a Transonic Turbine Stage,” *Journal of Turbomachinery*, **132**(2), p. 021006.
- [28] Owen, J. M., 2011, “Prediction of Ingestion through Turbine Rim Seals-Part II: Externally Induced and Combined Ingress,” *Journal of Turbomachinery*, **133**(3), pp. 31006–1–31006–9.
- [29] Johnson, B. V., Mack, G. J., Paolillo, R. E., Daniels, W. A., Johnson, B., Beach, W. P., and Daniels, W., 1994, “Turbine Rim Seal Gas Path Flow Ingestion Mechanisms,” *30th Joint Propulsion Conference and Exhibit*, American Institute of Aeronautics and Astronautics, Reston, Virginia.
- [30] Owen, J. M., 2009, “Prediction of Ingestion through Turbine Rim Seals Part 1: Rotationally-Induced Ingress,” *Proceedings of the ASME Turbo Expo*, **3**(PART B), pp. 1071–1082.
- [31] Michael Owen, J., 2012, “Theoretical Modelling of Hot Gas Ingestion through Turbine Rim Seals,” *Propulsion and Power Research*, **1**(1), pp. 1–11.
- [32] Chilla, M., Hodson, H. P., Pullan, G., and Newman, D., 2016, “High-Pressure Turbine Rim Seal Design for Increased Efficiency,” *Volume 2B: Turbomachinery*, ASME, p. V02BT38A046.
- [33] Paniagua, G., Dénos, R., and Almeida, S., 2004, “Effect of the Hub Endwall Cavity Flow on the Flow-Field of a Transonic High-Pressure Turbine,” *Journal of Turbomachinery*, **126**(4), p. 578.
- [34] Rosic, B., Denton, J. D., Curtis, E. M., and Peterson, A. T., 2007, “The Influence of Shroud and Cavity Geometry on Turbine Performance — An Experimental and Computational Study: Part II — Exit Cavity Geometry,” *Volume 6: Turbo Expo 2007, Parts A and B*, ASME, pp. 761–771.
- [35] Miller, R. A., and Lowell, C. E., 1982, “Metallurgical and Protective Coatings 265 Failure Mechanisms of Thermal Barrier Coatings Exposed To Elevated Temperatures*,” pp. 265–273.
- [36] Sheffler, K. D., and Gupta, D. K., 1988, “Current Status and Future Trends in Turbine Application of Thermal Barrier Coatings,” *Journal of Engineering for Gas Turbines and Power*, **110**(4), pp. 605–609.
- [37] Zhou, D. W., Roy, R. P., Wang, C.-Z., and Glahn, J. a., 2011, “Main Gas Ingestion in a Turbine Stage for Three Rim Cavity Configurations,” *Journal of Turbomachinery*, **133**(3), p. 031023.

- [38] Moon, M., Lee, C., Kim, K.-Y., and Kim, J., 2014, “Effects of Geometry on Sealing Effectiveness of a Rim Seal,” *Volume 5C: Heat Transfer*, ASME, p. V05CT16A007.
- [39] Popović, I., and Hodson, H. P., 2013, “Improving Turbine Stage Efficiency and Sealing Effectiveness Through Modifications of the Rim Seal Geometry,” *Journal of Turbomachinery*, **135**(6), p. 061016.
- [40] Popović, I., and Hodson, H. P., 2012, “The Effects of a Parametric Variation of the Rim Seal Geometry on the Interaction Between Hub Leakage and Mainstream Flows in HP Turbines,” *Volume 4: Heat Transfer, Parts A and B*, ASME, p. 1823.
- [41] McLean, C., Camci, C., and Glezer, B., 2001, “Mainstream Aerodynamic Effects Due to Wheel-space Coolant Injection in a High-Pressure Turbine Stage: Part I—Aerodynamic Measurements in the Stationary Frame,” *Journal of Turbomachinery*, **123**(4), p. 687.
- [42] Barigozzi, G., Fontaneto, F., Franchini, G., Perdichizzi, A., Maritano, M., and Abram, R., 2012, “Influence of Coolant Flow Rate on Aero-Thermal Performance of a Rotor Blade Cascade With Endwall Film Cooling,” *Journal of Turbomachinery*, **134**(5), p. 051038.
- [43] Suryanarayanan, A., Mhetras, S. P., Schobeiri, M. T., and Han, J. C., 2009, “Film-Cooling Effectiveness on a Rotating Blade Platform,” *Journal of Turbomachinery*, **131**(1), p. 011014.
- [44] Suryanarayanan, A., Ozturk, B., Schobeiri, M. T., and Han, J. C., 2010, “Film-Cooling Effectiveness on a Rotating Turbine Platform Using Pressure Sensitive Paint Technique,” *Journal of Turbomachinery*, **132**(4), p. 041001.
- [45] McVetta, A., Giel, P., and Welch, G., 2012, “Aerodynamic Investigation of Incidence Angle Effects in a Large Scale Transonic Turbine Cascade,” 48th AIAA/ASME/SAE/ASEE Joint Propulsion Conference & Exhibit, (August), pp. 1–15.
- [46] Nakaya, K., 1995, “Hydrodynamic Function of the Head in the Hammerhead Sharks (Elasmobranchii: Sphyrnidae),” *Copeia*, **1995**(2), p. 330.
- [47] Fish, F. E., and Battle, J. M., 1995, “Hydrodynamic Design of the Humpback Whale Flipper,” *Journal of Morphology*, **225**(1), pp. 51–60.
- [48] Fish, F. E., Weber, P. W., Murray, M. M., and Howle, L. E., 2011, “The Tubercles on Humpback Whales’ Flippers: Application of Bio-Inspired Technology,” *Integrative and Comparative Biology*, **51**(1), pp. 203–213.
- [49] Miklosovic, D. S., Murray, M. M., Howle, L. E., and Fish, F. E., 2004, “Leading-Edge Tubercles Delay Stall on Humpback Whale (Megaptera Novaeangliae) Flippers,” *Physics of Fluids*, **16**(5).
- [50] Hanke, W., Witte, M., Miersch, L., Brede, M., Oeffner, J., Michael, M., Hanke, F., Leder, A., and Dehnhardt, G., 2010, “Harbor Seal Vibrissa Morphology Suppresses Vortex-Induced Vibrations,” *Journal of Experimental Biology*, **213**(15), pp. 2665–2672.

- [51] Shyam, V., Ameri, A., Poinsette, P., Thurman, D., Wroblewski, A., and Snyder, C., 2015, “Application of Pinniped Vibrissae to Aeropropulsion,” *Volume 2A: Turbomachinery*, ASME, p. V02AT38A023.
- [52] Luo, Y., Wen, F., Wang, S., Zhang, S., Wang, S., and Wang, Z., 2019, “Numerical Investigation on the Biomimetic Trailing Edge of a High-Subsonic Turbine Blade,” *Aerospace Science and Technology*, **89**, pp. 230–241.
- [53] Pym, S. A., Asghar, A., Allan, W. D. E., and Clark, J. P., 2019, “A Low Reynolds Number Experimental Evaluation of Tubercles on a Low-Pressure Turbine Cascade,” p. 12.
- [54] Miklosovic, D. S., Murray, M. M., and Howle, L. E., 2007, “Experimental Evaluation of Sinusoidal Leading Edges,” *Journal of Aircraft*, **44**(4), pp. 1404–1408.
- [55] Hansen, K. L., Kelso, R. M., and Dally, B. B., 2012, “Performance Variations of Leading-Edge Tubercles for Distinct Airfoil Profiles,” *AIAA Journal*, **49**(1), pp. 185–194.
- [56] Shyam, V., Poinsette, P., Thurman, D., Dearmon, E., Stone, M., and Rogenski, E., 2018, “Characterization and Analysis of Phoca Vitulina, Zalophus Californianus and Mirounga Angustirostris Vibrissae,” NASA Technical Report, (July 2018), pp. 1–80.
- [57] Paniagua, G., Yasa, T., La Loma, A. D., Castillon, L., and Coton, T., 2008, “Unsteady Strong Shock Interactions in a Transonic Turbine: Experimental and Numerical Analysis,” *Journal of Propulsion and Power*, **24**(4), pp. 722–731.
- [58] Vogel, J. C., and Eaton, J. K., 1985, “Combined Heat Transfer and Fluid Dynamic Measurements Downstream of a Backward-Facing Step,” *Journal of Heat Transfer*, **107**(4), p. 922.
- [59] Menter, F. R., 1993, “Zonal Two Equation K-w, Turbulence Models for Aerodynamic Flows,” AIAA paper, p. 2906.
- [60] Verstraete, T., 2010, “CADO: A Computer Aided Design and Optimization Tool for Turbomachinery Applications,” *International Conference on Engineering Optimization*, Lisbon 2010, pp. 1–10.
- [61] Verstraete, T., Alsalihi, Z., and Van den Braembussche, R. a., 2010, “Multidisciplinary Optimization of a Radial Compressor for Microgas Turbine Applications,” *Journal of Turbomachinery*, **132**(3), p. 031004.
- [62] Mueller, L., Verstraete, T., and Arts, T., 2013, “Design of the Primary Liquid-Metal Pump of the Myrrha Research Reactor,” *Proceedings of 10th European Conference on Turbomachinery Fluid dynamics & Thermodynamics*, pp. 1–13.
- [63] Storn, R., and Price, K., 1997, “Differential Evolution – A Simple and Efficient Heuristic for Global Optimization over Continuous Spaces,” *Journal of Global Optimization*, **11**(4), pp. 341–359.

- [64] Deb, K., Pratap, A., Agarwal, S., and Meyarivan, T., 2002, “A Fast and Elitist Multiobjective Genetic Algorithm: NSGA-II,” *IEEE Transactions on Evolutionary Computation*, **6**(2), pp. 182–197.
- [65] Lampinen, J., and Zelinka, I., 2000, “On the Stagnation of the Differential Evolution Algorithm,” *On Stagnation of the Differential Evolution Algorithm*, Brno, Czech Republic, pp. 76–83.
- [66] Price, K. V., Storn, J. A., and Zebinsky, Z. B., 2005, “The Role of Cr in Optimization,” *A Practical Approach to Global Optimization*, Springer, pp. 97–104.
- [67] Gamperle, R., Muller, S. D., and Koumoutsakos, P., “A Parameter Study for Differential Evolution,” p. 6.
- [68] Rosenbrock, H. H., 1960, “An Automatic Method for Finding the Greatest or Least Value of a Function,” *The Computer Journal*, **3**(3), pp. 175–184.
- [69] Yi, M., Xiaodong, L., Xin, Y., and Omidvar, M. N., 2016, “A Competitive Divide-and-Conquer Algorithm for Unconstrained Large-Scale Black-Box Optimization,” *ACM Transactions on Mathematical Software*, **42**(2).
- [70] Queipo, N. V., and Nava, E., 2019, “A Gradient Boosting Approach with Diversity Promoting Measures for the Ensemble of Surrogates in Engineering,” *Structural and Multidisciplinary Optimization*, (Tenne 2013).
- [71] Raquel, C. R., and Naval, P. C., 2005, “An Effective Use of Crowding Distance in Multiobjective Particle Swarm Optimization,” *GECCO 2005 - Genetic and Evolutionary Computation Conference*, pp. 257–264.
- [72] Li, X., Tang, K., Omidvar, M., Yang, Z., Qin, K., and China, H., 2013, “Benchmark Functions for the CEC’2013 Special Session and Competition on Large-Scale Global Optimization,” *Gene*, **7**(33), p. 8.
- [73] Omidvar, M. N., Yang, M., Mei, Y., Li, X., and Yao, X., 2017, “DG2: A Faster and More Accurate Differential Grouping for Large-Scale Black-Box Optimization,” *IEEE Transactions on Evolutionary Computation*, **21**(6), pp. 929–942.
- [74] Bartz-Beielstein, T., Limbourg, P., Mehnen, J., Schmitt, K., Parsopoulos, K. E., and Vrahatis, M. N., 2003, “Particle Swarm Optimizers for Pareto Optimization with Enhanced Archiving Techniques,” *2003 Congress on Evolutionary Computation, CEC 2003 - Proceedings*, **3**, pp. 1780–1787.
- [75] Kramer, O., 2017, *Studies in Computational Intelligence 679 Genetic Algorithm Essentials*.
- [76] Kursawe, F., 1991, “A Variant of Evolution Strategies for Vector Optimization,” *Lecture Notes in Computer Science (including subseries Lecture Notes in Artificial Intelligence and Lecture Notes in Bioinformatics)*, **496 LNCS**, pp. 193–197.

- [77] Leung, M. F., Ng, S. C., Cheung, C. C., and Lui, A. K., 2014, “A New Strategy for Finding Good Local Guides in MOPSO,” *Proceedings of the 2014 IEEE Congress on Evolutionary Computation, CEC 2014*, pp. 1990–1997.
- [78] Lim, W. J., Jambek, A. B., and Neoh, S. C., 2015, “Kursawe and ZDT Functions Optimization Using Hybrid Micro Genetic Algorithm (HMGA),” *Soft Computing*, **19**(12), pp. 3571–3580.
- [79] Hou, Z., 2012, *Lecture Notes in Electrical Engineering*.
- [80] De Maesschalck, C., Lavagnoli, S., Paniagua, G., and Vinha, N., 2014, “Aerothermodynamics of Tight Rotor Tip Clearance Flows in High-Speed Unshrouded Turbines,” *Applied Thermal Engineering*, **65**(1–2), pp. 343–351.
- [81] Yasa, T., Paniagua, G., and Bussolin, A., 2007, “Performance Analysis of a Transonic High-Pressure Turbine,” *Proceedings of the Institution of Mechanical Engineers, Part A: Journal of Power and Energy*, **221**(6), pp. 769–778.
- [82] Atkins, N. R., and Ainsworth, R. W., 2012, “Turbine Aerodynamic Performance Measurement Under Nonadiabatic Conditions,” *Journal of Turbomachinery*, **134**(6), p. 061001.
- [83] Sieverding, C. H., Stanislas, M., and Snoeck, J., 1980, “The Base Pressure Problem in Transonic Turbine Cascades,” *Journal of Engineering for Power*, **102**(3), p. 711.
- [84] Joly, M. M., Verstraete, T., and Paniagua, G., 2013, “Differential Evolution Based Soft Optimization to Attenuate Vane-Rotor Shock Interaction in High-Pressure Turbines,” *Applied Soft Computing Journal*, **13**(4), pp. 1882–1891.
- [85] Denton, J., and Pullan, G., 2012, “A Numerical Investigation Into the Sources of Endwall Loss in Axial Flow Turbines,” *Volume 8: Turbomachinery, Parts A, B, and C*, ASME, Copenhagen, Denmark, p. 1417.
- [86] Ronkkonen, J., Kukkonen, S., and Price, K. V., 2005, “Real-Parameter Optimization with Differential Evolution,” *2005 IEEE Congress on Evolutionary Computation*, IEEE, Edinburgh, Scotland, UK, pp. 506–513.
- [87] Montgomery, D., *Design and Analysis of Experiments*, Wiley.
- [88] Storn, R., and Price, K., 1997, “Differential Evolution – A Simple and Efficient Heuristic for Global Optimization over Continuous Spaces,” *Journal of Global Optimization*, **11**(4), pp. 341–359.
- [89] Kolář, V., 2007, “Vortex Identification: New Requirements and Limitations,” *International Journal of Heat and Fluid Flow*, **28**(4), pp. 638–652.
- [90] HALLER, G., 2005, “An Objective Definition of a Vortex,” *Journal of Fluid Mechanics*, **525**, pp. 1–26.

- [91] Juangphanich, P., De Maesschalck, C., and Paniagua, G., 2019, “Turbine Passage Design Methodology to Minimize Entropy Production—A Two-Step Optimization Strategy,” *Entropy*, **21**(6), p. 604.
- [92] Phadke, U. P., and Owen, J. M., 1983, “An Investigation of Ingress for an ‘Air-Cooled’ Shrouded Rotating Disk System With Radial-Clearance Seals,” *Journal of Engineering for Power*, **105**(1), p. 178.
- [93] Chew, J. W., 1991, “A Theoretical Study of Ingress for Shrouded Rotating Disk Systems with Radial Outflow,” *Journal of Turbomachinery*, **113**(1), pp. 91–97.
- [94] Phadke, U. P., and Owen, J. M., 1988, “Aerodynamic Aspects of the Sealing of Gas-Turbine Rotor-Stator Systems,” *International Journal of Heat and Fluid Flow*, **9**(2), pp. 98–105.
- [95] Phadke, U. P., and Owen, J. M., 1988, “Aerodynamic Aspects of the Sealing of Gas-Turbine Rotor-Stator Systems. Part 2: The Performance of Simple Seals in Quasi-axisymmetric External Flow,” *International Journal of Heat and Fluid Flow*, **9**(2), pp. 98–105.
- [96] Phadke, U. P., and Owen, J. M., 1988, “Aerodynamic Aspects of the Sealing of Gas-Turbine Rotor-Stator Systems. Part 3: The Effect of Nonaxisymmetric External Flow on Seal Performance,” *International Journal of Heat and Fluid Flow*, **9**(2), pp. 113–117.
- [97] Bayley, F. J., and Owen, J. M., 1970, “The Fluid Dynamics of a Shrouded Disk System with a Radial Outflow of Coolant,” *Journal of Engineering for Gas Turbines and Power*, **92**(3), pp. 335–341.
- [98] Piotrowski, A. P., 2017, “Review of Differential Evolution Population Size,” *Swarm and Evolutionary Computation*, **32**, pp. 1–24.
- [99] Roy, R. P., Feng, J., Narzary, D., and Paolillo, R. E., 2005, “Experiment on Gas Ingestion Through Axial-Flow Turbine Rim Seals,” *Journal of Engineering for Gas Turbines and Power*, **127**(3), p. 573.
- [100] Clark, J. P., and Grover, E. a., 2007, “Assessing Convergence in Predictions of Periodic-Unsteady Flowfields,” *Journal of Turbomachinery*, **129**(4), p. 740.
- [101] Juangphanich, P., De Maesschalck, C. G., and Paniagua, G., 2017, “From Conceptual 1D Design Towards Full 3D Optimization of a Highly Loaded Turbine Stage,” 55th AIAA Aerospace Sciences Meeting, (January), pp. 1–14.
- [102] Liao, G., Wang, X., Li, J., and Zhou, J., 2015, “Numerical Investigation on the Flow and Heat Transfer in a Rotor-Stator Disc Cavity,” *Applied Thermal Engineering*, **87**, pp. 10–23.
- [103] Atkins, N. R., and Ainsworth, R. W., 2012, “Turbine Aerodynamic Performance Measurement Under Nonadiabatic Conditions,” *Journal of Turbomachinery*, **134**(6), p. 061001.

- [104] Ameri, A. A., and Steinthorsson, E., 1995, “Prediction of Unshrouded Rotor Blade Tip Heat Transfer,” p. V004T09A037.
- [105] Giel, P. W., Boyle, R. J., and Bunker, R. S., 2004, “Measurements and Predictions of Heat Transfer on Rotor Blades in a Transonic Turbine Cascade,” *Journal of Turbomachinery*, **126**(1), p. 110.
- [106] Guenette, G. R., Epstein, A. H., Giles, M. B., Haines, R., and Norton, R. J. G., 2009, “Fully Scaled Transonic Turbine Rotor Heat Transfer Measurements,” *Journal of Turbomachinery*, **111**(1), p. 1.
- [107] Ooi, A., Iaccarino, G., Durbin, P. A., and Behnia, M., 2002, “Reynolds Averaged Simulation of Flow and Heat Transfer in Ribbed Ducts,” *International Journal of Heat and Fluid Flow*, **23**(6), pp. 750–757.
- [108] Paniagua, G., Cuadrado, D., Saavedra, J., Andreoli, V., Meyer, T., Solano, J. P., Herrero, R., Meyer, S., and Lawrence, D., 2018, “Design of the Purdue Experimental Turbine Aerothermal Laboratory for Optical and Surface Aerothermal Measurements,” *Journal of Engineering for Gas Turbines and Power*, **141**(1), p. 012601.
- [109] Juangphanich, P., and Paniagua, G., 2018, “Meander-Like Shape Optimization of the Stator-Rotor Platform Cavity,” Oslo, Norway.
- [110] Pinilla, V., Solano, J. P., Paniagua, G., and Anthony, R. J., 2012, “Adiabatic Wall Temperature Evaluation in a High Speed Turbine,” *Journal of Heat Transfer*, **134**(9), p. 091601.
- [111] Bell, J. H., and Mehta, R. D., 1988, *Contraction Design for Small Low-Speed Wind Tunnels*, NASA.
- [112] Morel, T., 1975, “Comprehensive Design of Axisymmetric Wind Tunnel Contractions,” *Journal of Fluids Engineering*, **97**(2), pp. 225–233.

LETTERS

Dear Mr. Juangphanich,

It is our pleasure to grant you permission to use the following ASME Figures ONLY:

- Figures 1, 4 from Sieverding, C. H. (1985). Recent Progress in the Understanding of Basic Aspects of Secondary Flows in Turbine Blade Passages. *Journal of Engineering for Gas Turbines and Power*, 107(2)
- Figure 2 from Sharma, O. P., & Butler, T. L. (1987). Predictions of endwall losses and secondary flows in axial flow turbine cascades. *Journal of Turbomachinery*, 109(2)
- Figure 1 from Pralsner, T. J., Allen-Bradley, E., Grover, E. A., Knezevici, D. C., & Sjolander, S. A. (2007). Application of non-axisymmetric endwall contouring to conventional and high-lift turbine airfoils. *Proceedings of the ASME Turbo Expo*, 6 PART A(November)

cited in your letter for inclusion in thesis to be published by Purdue University.

Permission is granted for the specific use as stated herein and does not permit further use of the materials without proper authorization. As is customary, we request that you ensure proper acknowledgment of the exact sources of this material, the authors, and ASME as original publisher.

Many thanks for your interest in ASME publications.

Sincerely,

Beth Darchi
Publishing Administrator
ASME
2 Park Avenue
New York, NY 10016-5990
darchib@asme.org

Dear Mr. Juangphanich,

It is our pleasure to grant you permission to use all or any part of the ASME paper “Meander-Like Shape Optimization of the Stator-Rotor Platform Cavity,” by Paht Juangphanich, Guillermo Paniagua, Paper No: GT2018-77167, cited in your letter for inclusion in a dissertation entitled Bio-inspired optimization of a turbine stage.

Permission is granted for the specific use as stated herein and does not permit further use of the materials without proper authorization. Proper attribution must be made to the author(s) of the materials. Please note: if any or all of the figures and/or Tables are of another source, permission should be granted from that outside source or include the reference of the original source. ASME does not grant permission for outside source material that may be referenced in the ASME works.

As is customary, we request that you ensure full acknowledgment of this material, the author(s), source and ASME as original publisher. Acknowledgment must be retained on all pages where figure is printed and distributed.

Many thanks for your interest in ASME publications.

Sincerely,

Beth Darchi
Publishing Administrator
ASME
2 Park Avenue
New York, NY 10016-5990
Tel 1.212.591.7700
darchib@asme.org

PUBLICATIONS

- Abdou, E., Carvalhar, A. P., Harry, J., Juangphanich, P., Klein, M., De Maesschalck, C., ... Pourpoint, T. (2017). Turbopump design, build, and testing at Purdue University. *AIAA SciTech Forum - 55th AIAA Aerospace Sciences Meeting*, (January), 1–22. <https://doi.org/10.2514/6.2017-0300>
- Juangphanich, P., De Maesschalck, C., & Paniagua, G. (2019). Turbine passage design methodology to minimize entropy production-A two-step optimization strategy. *Entropy*, 21(6). <https://doi.org/10.3390/e21060604>
- Juangphanich, P., & Paniagua, G. (2018). Meander-like shape optimization of the stator-rotor platform cavity. *Proceedings of the ASME Turbo Expo, 5C-2018*, 1–12. <https://doi.org/10.1115/GT2018-77167>
- Juangphanich, P., De Maesschalck, C., & Paniagua, G. (2017). From conceptual 1D design to full 3D optimization of a highly loaded turbine stage. *AIAA SciTech Forum - 55th AIAA Aerospace Sciences Meeting*, (January), 1–14. <https://doi.org/10.2514/6.2017-0110>